Synthesis and characterization of cobalt nanocrystals

by

Dmitry P. Dinega

Diploma in Chemistry
Moscow State University, Moscow, 1993

Submitted to the Department of Chemistry
In partial fulfillment of the requirements for
the degree of

DOCTOR OF PHILOSOPHY

at the

MASSACHUSETTS INSTITUTE OF TECHNOLOGY

September 2001

Signature of Author _____
Department of Chemistry
August 24, 2001

Certified by _____
Moungi G. Bawendi
Professor of Chemistry
Thesis Supervisor

Accepted by _____
Robert W. Field
Chairman, Departmental Committee on Graduate Students

This doctoral thesis has been examined by a committee of the Department of Chemistry as follows:

Professor Robert Griffin ___ Chairman

Professor Moungi Bawendi _____ Thesis Supervisor

Professor Christopher Cummins

Professor Robert Cohen Department of Chemical Engineering

Synthesis and characterization of cobalt nanocrystals

by

Dmitry P. Dinega

Submitted to the Department of Chemistry on August 24, 2001 in partial fulfillment of the requirements for the degree of Doctor of Philosophy in Chemistry

ABSTRACT

Although several theoretical models for the behavior of magnetic crystals smaller than a single domain size were developed in the 1950's and 60's, they have hardly been verified experimentally because of the lack of appropriate material systems. This thesis is an attempt to develop such a system using metallic cobalt as a magnetic material and to verify its magnetic behavior in the context of a Stoner-Wohlfarth model of coherent rotation. The problem of preparing crystals of a desired shape and the effect of the crystal shape on its magnetic properties is also addressed.

Cobalt nanocrystals are prepared by thermal decomposition of dicobalt octacarbonyl in solution and in the presence of suitable surfactants and coordinating ligands, which influence the shape of the resulting crystals as well as their internal structure. The presence of trialkylphosphines in the growth solution leads to the formation of spherical nanocrystals with mixed fcc-hcp structure, where as trioctylphosphine oxide leads to a newly discovered structure of ε-cobalt. The final size of the crystals is controlled by the precursor-to-ligand ratio, and low polydispersity is achieved by the separation of nucleation and growth stages. Size-selective precipitation is used to further reduce the size variation of the samples. As a result, cobalt nanocrystals in the size range of 4-12 nm in diameter can be routinely produced with size distributions as small as 6%. The study of magnetic properties reveals the superparamagnetic nature of cobalt nanocrystals of this size range at room temperature. At low temperatures, a good qualitative agreement with the theoretical (Stoner-Wohlfarth) model is found, although quantitative results are strongly influenced by the presence of an oxide shell around each nanocrystal.

The presence of two surfactants (trialkylphosphines and sodium carboxylates) during the growth leads to the formation of a significant number of triangular and rod-shaped nanocrystals. Unlike disordered spherical particles, these nanocrystals have pure fcc structure without visible defects. The length of the rods is roughly controlled by the concentration of carboxylates in the growth solution and can be changed within a 40-400 nm range. Unlike spherical crystals of comparable volume, the rods are ferromagnetic even at room temperature due to an added effect of shape anisotropy. A growth mechanism for the formation of nanorods with cubic structure is also proposed.

Thesis supervisor: Moungi G. Bawendi, Ph.D.
Title: Professor of Chemistry and W. M. Keck Professor of Energy

Dedicated to my parents **Marianna** and **Petr** who were the first to introduce me to the magic of chemistry in my childhood

and

to my sons **Anton** and **Kirill** who were the continuous source of inspiration during most of the time this work has been conducted

Table of Contents

List of Figures

"…. в науке нет широкой столбовой дороги, и только тот достигнет её сияющих вершин, кто не страшась усталости и невзгод карабкается по её каменистым тропам."

Карл Маркс

Chapter 1
Introduction

1.1 Small size is special

When atoms or molecules assemble into a crystalline lattice, they interact in a very organized manner. These periodic collective interactions are responsible for the development of "energy bands", which define the physical properties of any solid material. These properties do not usually depend on size. However, if a material can be made such that its physical dimensions are smaller than the characteristic length of a given property or interaction, then that material will exhibit size dependent phenomena not seen in the bulk form. Many important physical properties of materials have their characteristic length scales between 1 and 100nm. In order to display size dependent properties, the physical dimensions of a material should fall somewhere in this range, depending on the property of interest. This is how the new field of "nanostructured materials" has emerged. Since the size of a single atom is on the order of 0.1nm, nanomaterials usually contain $10^2 - 10^7$ atoms. Interestingly, they represent a transitional state between single atoms or molecules on one side and the solid state on the other, and are often referred to as mesoscopic (or intermediate) materials. The novel phenomena resulting from an unusually small size of these materials can manifest themselves in a wide range of properties – electronic, optical, magnetic, etc.

The study of magnetic nanocrystals as described in this thesis was inspired and motivated in great deal by the advancement of knowledge generated during the pioneering work of other group members on semiconductor nanocrystals. Some basic properties of these nanocrystals are summarized, therefore, in the following section.

1.2 The case of semiconductor nanocrystals

In bulk semiconductors, the characteristic length of any material is given by the Bohr radius of the electron-hole pair (exciton) which is formed when a material absorbs a sufficient amount of energy. For the bulk cadmium selenide (a semiconductor most widely studied in a nanocrystalline form), for example, the Bohr exciton radius is only 56Å. When the crystals are 112Å (in diameter) or larger, the excitons inside feel quite "natural". In other words, they do not feel any confinement; as if the crystal were infinitely large. If the dimensions of a crystal are smaller than this characteristic length, the carriers inside the crystal will be confined to a smaller volume than they are used to, leading to a new set of size dependent properties. Depending on the geometry of the crystal, the carriers can be confined in one, two, or all three dimensions as in quantum wells, quantum wires, and quantum dots respectively.

Semiconductor quantum dots, in which excitons are confined in all three dimensions, represent the ultimate in quantum confined materials and have become the subject of numerous studies. Although they can be made by several different techniques, the

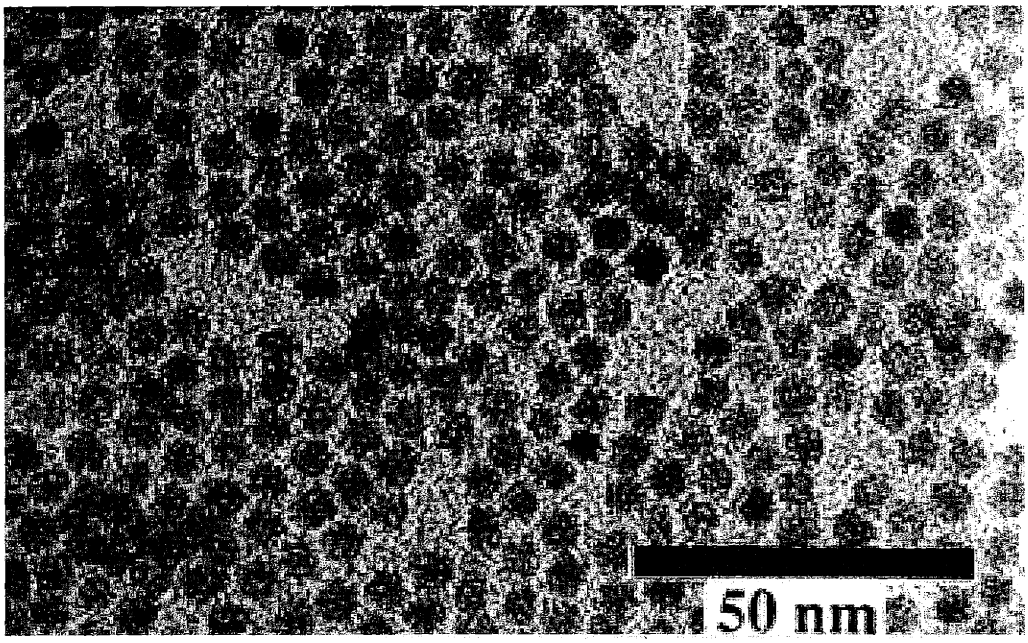

Figure 1.1 TEM image of chemically synthesized CdSe nanocrystals.
(the work of F. V. Mikulec and C. B. Murray)

growth of nanocrystals in solution (the so-called bottom-up approach) has become the most successful method. In 1993, Murray *et al.*[1] demonstrated that under appropriate conditions the chemical synthesis in solution can yield CdSe nanocrystals with nearly atomic roughness (Figure **1.1**). Moreover, this enabled them to characterize their size dependent properties with great accuracy. For example, the size dependence of the optical absorption spectra for CdSe nanocrystals is shown in Figure **1.2**. The systematic blue shift of the absorption peaks with decreasing crystalline size is a direct result of a quantum confinement and can be well understood in the context of a particle-in-the-box quantum mechanical model. As an exciton is confined to smaller and smaller volume, the HOMO-LUMO gap shifts to a higher energy and discrete electronic states emerge from the continuum of the bulk bands (Figure **1.3**).

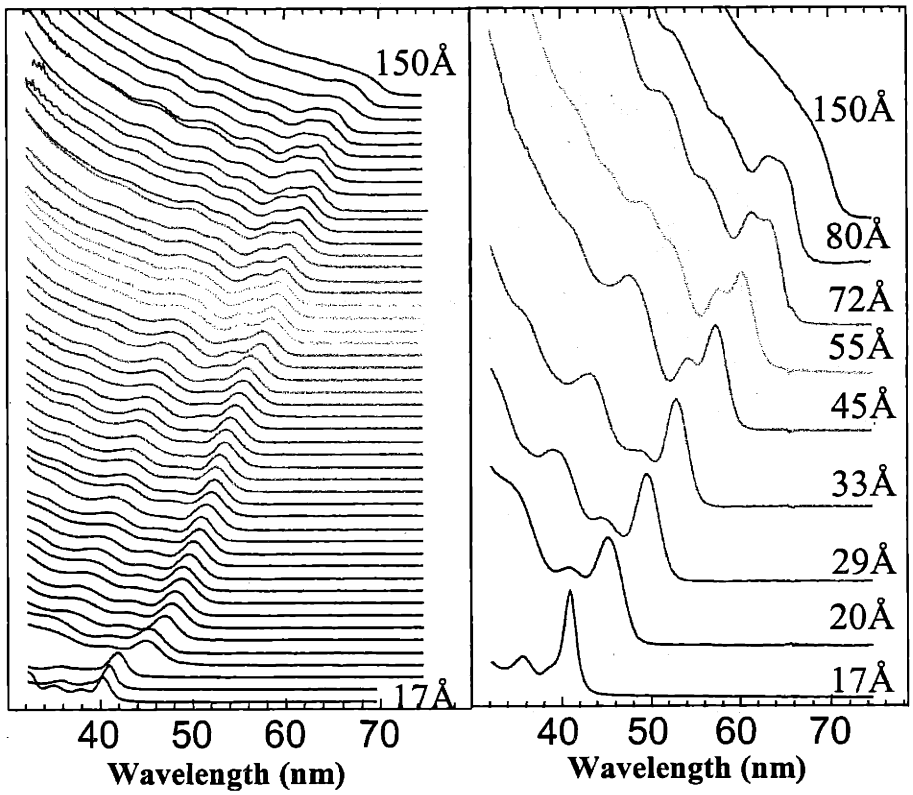

Figure 1.2 Absorption spectra of CdSe nanocrystals size series; a gradual shift of main absorption peak from red to blue is clearly observed.

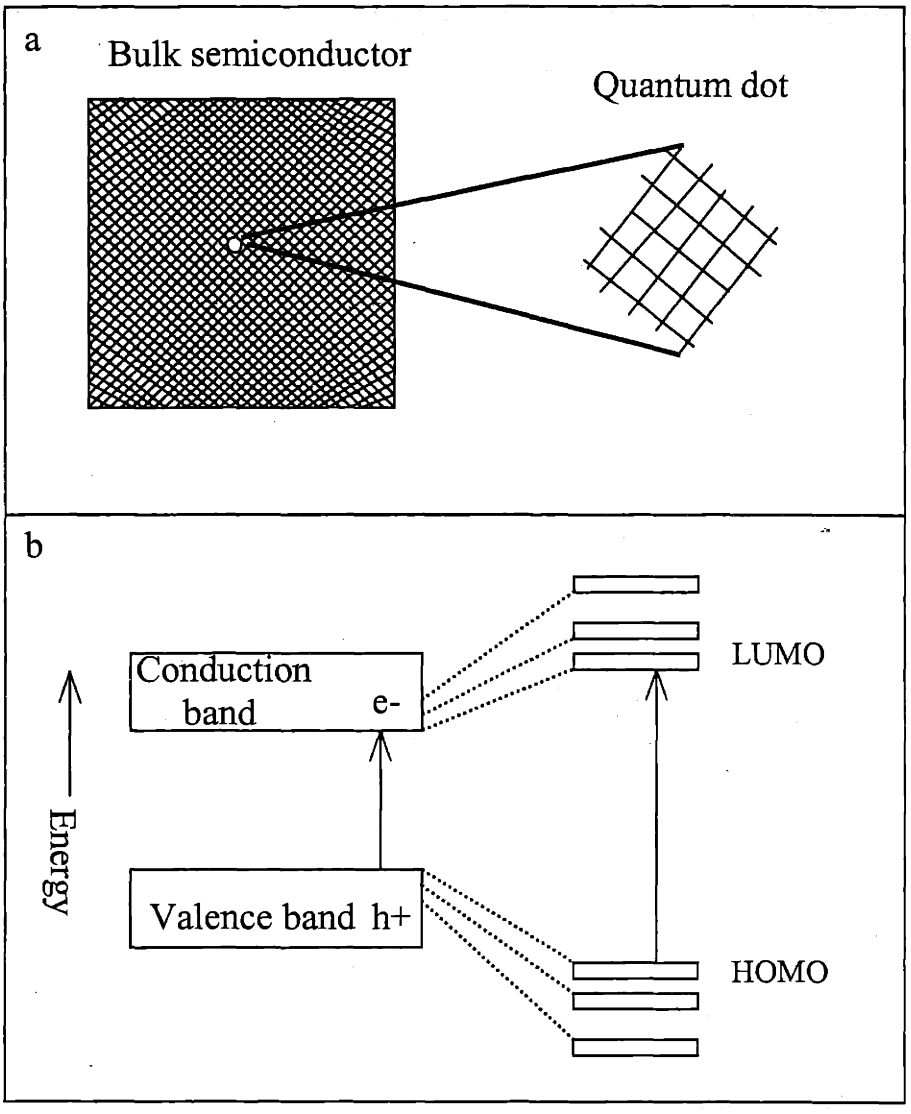

Figure 1.3 **a** - cartoon depicts a quantum dot as an excised fragment of the bulk lattice; **b**- energy diagram shows the effects of the special confinement of excitations in the quantum dot.

Although the most basic properties of semiconductor nanocrystals were understood in the context of existing theoretical models, detailed studies revealed the presence of more subtle features. For example, a fine structure of band edge electronic state observed in PLE experiments[2] and a size dependent Stokes shift found in fluorescence line narrowing[3] could not be understood and led to the development of new theoretical models.[4] The dark exciton model proposed by Efros et al. helped later not only to understand the existing data, but also predict some new properties which were later confirmed experimentally. Polarized emission from the dots is a good example.[5]

The above examples were intended to demonstrate how the development of a new material (namely semiconductor nanocrystals) led to a significant advancement of our knowledge with regard to these systems. But it was not the only consequence. Scientists provided with new materials and empowered by a new knowledge quickly moved to the development of new technological applications. Novel light emitting devices[6], optical molecular labels[7], switches[8], and lasers[9] have demonstrated as a result of these studies. All these examples clearly show the enormous potential presented in the future by conventional materials when their size can be made very small.

1.3 Magnetic nanocrystals

Just like semiconductors, magnetic materials have a characteristic length of their own below which their properties become size dependent. Moreover, they even have two such lengths. The structure of a conventional bulk magnet consist of tiny randomly oriented magnetic domains. When its size is gradually reduced, at some point the material contains only one domain. This transition to a single domain regime is the first characteristic length. When the size is reduced further, the direction of magnetization inside the crystal becomes unstable and can be changed by thermal fluctuations. This is the second characteristic length in magnetic materials – the transition from ferromagnetic to superparamagnetic behavior. When the dimensions of any magnetic material are reduced beyond either characteristic lengths, sharp changes in properties should occur and the size dependence of properties should appear.

Although by the time this work was conceived in early 1996 there had been significant progress made in preparing and understanding the physical properties of

semiconductor quantum dots, magnetic nanocrystals were barely studied at all. The main obstacle had long been the lack of reliable methods able to produce highly uniform crystals in a nanometer range. Common physical methods of preparation, such as sputtering, did not provide the desired level of uniformity. As an example, Figure **1.4** shows the TEM image of state-of-the-art magnetic storage media developed by IBM by 1990.[10] A significant variation of the particle size and shape is clearly observed. Advanced chemical methods of growth had not been developed at all. As a result, several theoretical models for the behavior of single domain particles developed earlier[11] remained largely untested.

Besides being of purely scientific interest, magnetic nanocrystals (just as semiconductor ones) can be utilized in a variety of technological applications. To this end, magnetic storage is one example. Others include ferrofluids, magnetic refrigeration,[12] and various devices based on GMR effect.[13]

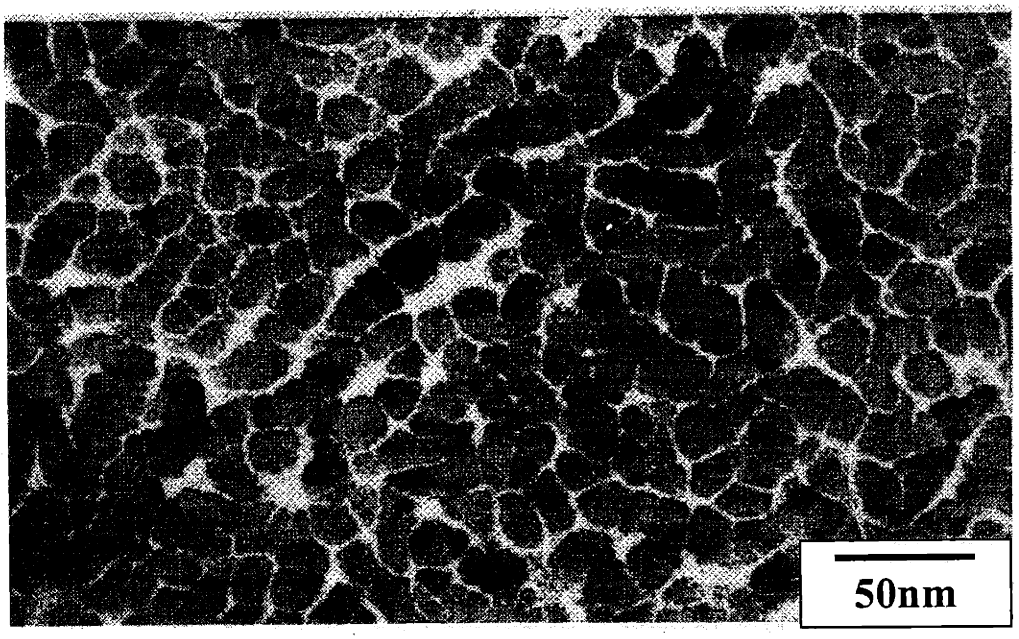

Figure 1.4 TEM image of 1Gb/in^2 magnetic storage medium developed by IBM (Co-Pt-Cr).[10]

We have chosen metallic cobalt nanocrystals as our model system for this study since metals exhibit much stronger magnetic properties than any other class of magnetic materials. Furthermore, cobalt has a variety of different crystal structures including highly symmetrical cubic as well as less symmetrical uniaxial hexagonal structure. Since the underlying structure has a strong influence on magnetic properties of the crystal, it makes our model system more general. Unlike cobalt, the other two common ferromagnetic metals (iron and nickel) are known to have only cubic lattices.

1.4 Thesis overview

This thesis is structured as follows. Chapter 2 describes the identification of a new crystal structure of elemental cobalt (ε-cobalt) discovered as a result of this study. This structure is quite common for chemically grown cobalt nanocrystals. A novel method for preparing nearly monodisperse spherical nanocrystals of variable size and a choice of two different crystal structures is proposed in Chapter 3. The assembly of these nanocrystals into amorphous and well-ordered two- and three-dimensional structures is also presented. Chapter 4 deals with structural characterization of newly prepared nanocrystals as well as their assemblies. A self-consistent structural model is developed as a result of elemental analysis, transmission electron microscopy and diffraction, and x-ray diffraction combined with structural simulations. In Chapter 5, size dependent magnetic properties are analyzed in the context of a coherent rotation model. Finally, a mechanism of shape control during preparation of cobalt nanocrystals and an effect of shape on the magnetic properties of nanocrystals is discussed in Chapter 6. Some important topics and equations used in Chapters 1 through 6 but not adequately addressed in the text are summarized in Appendices A through D.

1.5 References

1. Murray C. B., Norris D. J., Bawendi M. G. *J. Am. Chem. Soc.* **1993**, 115, 8706.
2. Norris D. J., Efros Al. L., Rosen M., Bawendi M. *Phys. Rev. B* **1996**, 53, 16347.
3. Efros Al. L., Rosen M., Kuno M., Nirmal M., Norris D. J., Bawendi M., *Phys. Rev B* **1996**, 54, 4843.

4. Efros Al. L., *Phys. Rev. B* **1992**, 46, 7448; Ekimov A. I., Hache F., Schanneklein M. C., Ricard D., Flytzanis C., Kudryavtsev I. A., Yazeva T. V., Rodina A. V., Efros Al. L. *J. Opt. Soc. Am. B*, **1993**, 10, 100; Efros Al. L., Rosen M. *Phys. Rev. B* **1998**, 58, 7120.
5. Empedocles S. A., Neuhauser R., Bawendi M. G. *Nature* **1999**, 399, 126.
6. Lee J., Sundar V. C., Heine J. R., Bawendi M. G., Jensen K. F. *Adv. Mater.* **2000**, 12, 1102.
7. Bruchez M., Moronne M., Gin P., Weiss S., Alivisatos A. P. *Science* **1998**, 281, 2013; Mattoussi H., Mauro J. M., Goldman E. R., Anderson G. P., Sundar V. C., Mikulec F. V., Bawendi M. G. *J. Amer. Chem. Soc.* **2000**, 122, 12142.
8. Woo W., *et al.* to be published.
9. Klimov V. I., Mikhailovsky A. A., Xu S., Malko A., Hollingsworth J. A., Leatherdale C. A., Eisler H. J., Bawendi M. G. *Science* **2000**, 290, 314.
10. Yogi T., Tsang C., Nguyen T., Ju K., Gorman G., Castillo G. *IEEE Trans. Mag.*, **1990**, 26, 2271.
11. Stoner E. C., Wohlfarth E. P. *Phil. Trans. Roy. Soc.* **1948**, A-240, 599; Jacobs I. S., Bean C. P. *Phys. Rev.*, **1955**, 100, 1060; Frei E. H., Shtrikman S., Treves D. *Phys. Rev.* **1957**, 106, 446.
12. Shull R. D., McMichael R. D., Ritter J. J., Bennett L. H. *Mat. Res. Soc. Symp. Proc.* **1993**, 286, 449.
13. Parkin S. S. P. *Annu. Rev. Mater. Sci.* **1995**, 25, 357; Barthelemy A., Cros V., Duvail J. L., Fert A., Morel R., Parent F., Petroff F., Steren L. B. *Nanostruc. Mater.* **1995**, 6, 217.

Chapter 2

New Crystal Structure of Elemental Cobalt

(Much of this chapter has appeared in print: Dmitry P. Dinega , M. G. Bawendi *Angew Chem. Int. Ed.* 1999, 38, 1788)

2.1 Introduction

As was emphasized in the previous chapter, the type of the lattice in which the atoms or molecules assemble to form a solid material plays a critical role in determining the physical properties of such a material. Not surprisingly, therefore, the very first characterization step for our newly grown cobalt nanocrystals was to look at their internal crystal structure. As it turned out, the structure of our cobalt was very different from anything observed in cobalt before. Unlike other chapters of the thesis, therefore, the content of this chapter describes the work that was not included in the original proposal. On the contrary, this realization came as a big surprise to us and was without any doubts worthwhile pursuing. As a result, a new crystal structure of elemental cobalt was fully identified.

2.2 Background

Cobalt has long been known to have two crystal structures - close-packed hexagonal (hcp) and face centered cubic (fcc). While both phases can coexist at room temperature, the fcc structure is thermodynamically preferred above 450°C and the hcp phase is favored at lower temperatures.[1] For small particles, however, the fcc structure appears to be preferred even below room temperature.[2] The existence of fcc and hcp cobalt was first reported by Hull[3] in 1921 after analyzing diffraction patterns of powders prepared by several methods. Krainer and Robitsch[4] reported observing new diffraction lines in samples prepared by spark erosion of bulk cobalt surfaces, but the structure was never fully established. Kajiwara[5] observed several new lines in the diffraction pattern of cobalt nanoclusters prepared by plasma evaporation and the subsequent condensation of the metal, but attributed these lines to a polymorphous form of two known structures. Similar results are reported by Leslie-Pelecky et al.[6] with cobalt particles prepared by the

reduction of cobalt salt in solution with metallic lithium. Two recent reports by Chaudret et al.[7-8] provides some evidence for a new nonperiodic polytetrahedral structure of cobalt present in very small (1.5nm in diameter) cobalt clusters produced by the decomposition of organometallic precursors, although the structure was not identified.

2.3 Experimental

2.3.1 General

The synthesis of all samples was performed under standard air-free atmosphere. All the chemicals were as purchased: dicobalt octacarbonyl (DCOC, 95%) and trioctylphosphine oxide (TOPO, 90%) from *Strem Chemicals, Inc.*, toluene (HPLC grade) from *Mallinckrodt Baker, Inc.* Separation of the product from the reaction mixture and the following size-selective precipitation were conducted under regular lab conditions (in the air) using Omnisolv™ grade solvents purchased from "*EM Science*".

2.3.2 Synthesis

We used thermal decomposition of dicobalt octacarbonyl in solution in the presence of trioctylphosphine oxide as a coordinating ligand to prepare cobalt nanoclusters. This method provides a "clean" route for the preparation of the material since elemental cobalt is the only non-volatile product of the reaction: $Co_2(CO)_8 = 2Co + 8CO\uparrow$. The preparation procedure was as follows: 2.5g of DCOC were dissolved in 30ml of dry toluene under air-free conditions, filtered, and then loaded into a syringe. 5g of TOPO were placed in a 100ml flask and dried under vacuum at 150°C. The temperature was then brought down to 50°C and the solution of DCOC was quickly injected into the flask while vigorously stirring under nitrogen atmosphere. The temperature was slowly increased to 110°C (b.p. of toluene). This was accompanied by evolution of carbon monoxide and by a color change of the reaction mixture from deep blue to black. After completion of the reaction the heating mantle was removed and the mixture was allowed to cool to room temperature.

2.3.3 Transmission Electron Microscopy

A JEOL 200CX transmission electron microscope (TEM) with tungsten filament operated at 200 kV was used to obtain the images of individual nanocrystals in the reaction product. The samples were prepared by placing one drop of a diluted suspension of particles in hexane onto a copper grid coated with a thin (4 nm) film of amorphous carbon (*Ladd Research, Inc.*).

2.3.4 Elemental Analysis

Elemental analysis was performed via wavelength dispersive x-ray spectroscopy (WDS). A JEOL SEM 733 electron microprobe operating at 15 kV was used to determine the content of cobalt, oxygen, and all other remaining elements in the product. The samples were prepared by pressing 1cm in diameter pellets, placing them on conductive carbon tape and evaporating a thin layer of carbon on the top in order to prevent any charging effects under the electron beam.

2.3.5 X-ray Diffraction

Powder diffraction patterns were recorded on a Rigaku Rotaflex 250 mm radius diffractometer with Cu-anode radiation. Measurements were in reflection mode at 19°C, with accelerating voltage of 60 kV, flux of 300 mA, and a step size of 0.002°. The pattern was calibrated with an internal Si standard (640A, NIST, USA). The samples were prepared by mixing cobalt and silicon powders and pressing a 1cm in diameter pellets with extremely flat surface.

2.3.6 Saturation magnetization measurements

Saturation magnetization was measured using Quantum Design MPMS2 SQUID magnetometer operated in a DC mode. The samples were thoroughly washed and dried powders (approx. 3mg) weighted on the analytical balance before being loaded into the magnetometer.

2.3.7 Thermal treatment

The thermal treatment was performed at 500 C in a sealed tubular oven with continuous flow of argon over the sample.

2.3.8 Structural simulations

The calculations were performed as follows: A stick spectrum was first calculated using the atomic coordinates presented in Table 1 applying standard diffraction theory. Lorentzian lineshapes with widths calculated from the size of the crystals using the Debye-Scherrer equation were then added.

2.4 Results and Discussion

2.4.1 Reaction product

The product of the reaction was isolated as a black powder accumulated on a magnetic stirbar, leaving the liquid phase of the flask almost clear or slightly blue. The powder was thoroughly washed by sonication in excess of hexane and later methanol followed by centrifugation and the disposal of supernatant. This process was repeated several times, after which the product was dried under nitrogen. Since the resulting powder was highly susceptible to magnetic fields generated by a small permanent magnet, it clearly represented a ferromagnetic material, presumably metallic cobalt particles since no other cobalt compound could have such a strong magnetic response. In order to verify this conclusion, TEM imaging and elemental analysis of the product was performed.

2.4.2 Transmission electron microscopy

Transmission electron microscopy (TEM) showed that the powder consisted of roughly spherical particles with an average diameter of 20 nm and a 15% size distribution. Later experiments showed that the size of the crystals is not limited to this range. In fact, injection at higher temperature using butylbenzene as a solvent (b.p. 135°C) yields regular polyhedron-shaped faceted crystals as large as 0.2 μm and possibly even larger (Figure **2.1**)

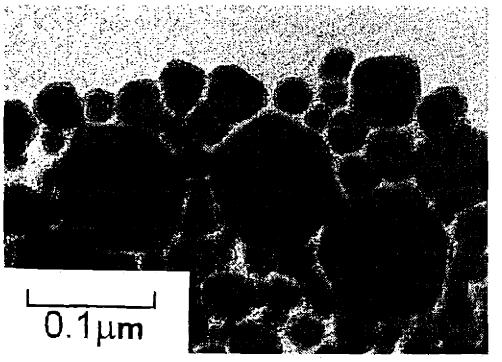

Figure 2.1 TEM image of 0.1 μm cobalt crystals with the new ε-cobalt structure

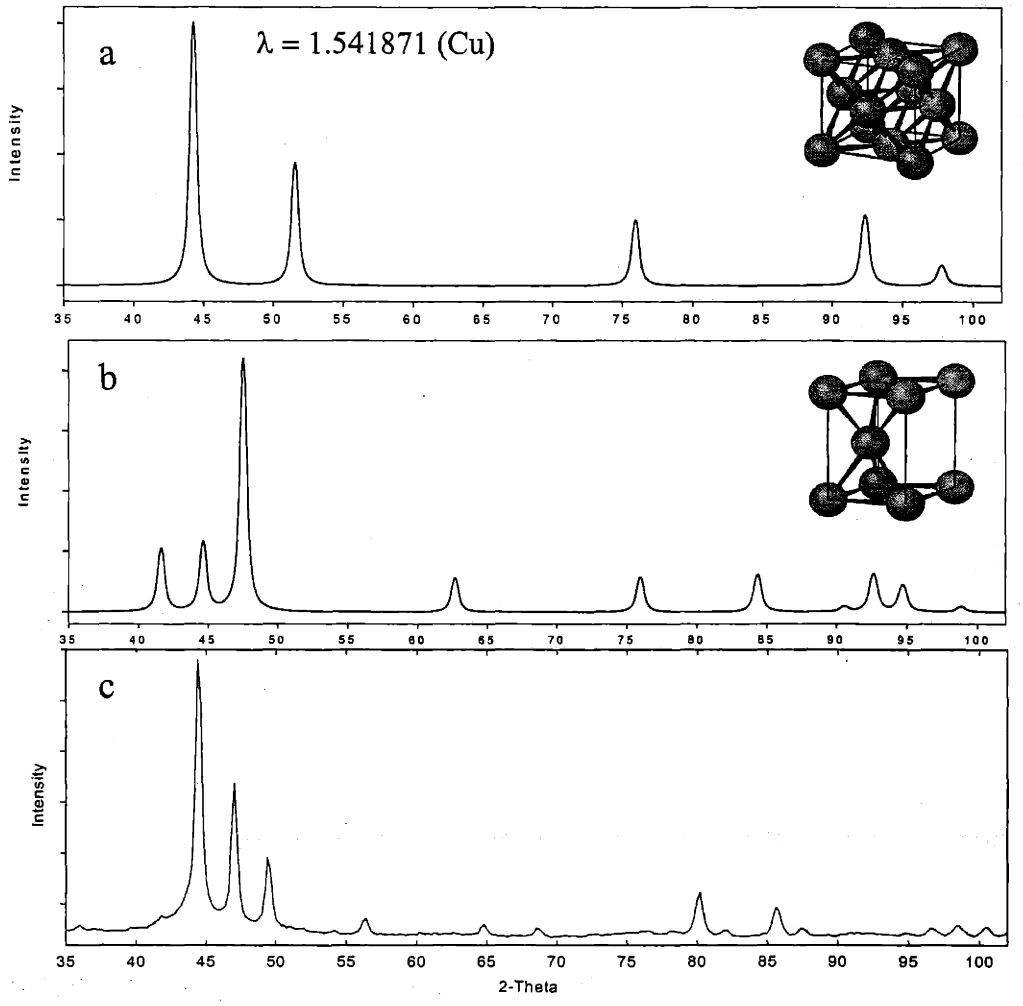

Figure 2.2 Comparison between two known diffraction patterns of elemental cobalt and a newly discovered one: **a**- fcc cobalt (simulated); **b**- hcp cobalt (simulated); **c**- epsilon cobalt (experimental).

2.4.3 Elemental analysis

Elemental analysis showed the following atomic percentage: cobalt-83%, oxygen-11%, other elements (carbon, hydrogen)-6%. The presence of oxygen indicates surface oxidation of the cobalt particles, corresponding to coverage of one to two monolayers of cobalt oxide for particle sizes in the 20 nm range. The other elements, we believe, come from residual organic solvents adsorbed on the particle surfaces. It should be emphasized here that freshly synthesized cobalt nanoparticles are extremely reactive towards oxidation. In fact, rapid exposure to air results in immediate oxidation accompanied by a red glow. Therefore, even simply washing the particles in organic solvents inevitably leads to surface oxidation by residual moisture and dissolved air. The resulting oxide layer appears to passivate the surface of the particles and considerably reduce the rate of further oxidation.

2.4.4 X-ray diffraction

Figure **2.2c** shows an X-ray powder diffraction pattern of the reaction product. For the comparison, the two known patterns (fcc and hcp) are also shown in Figure **2.2** (**a** and **b** respectively). This pattern does not correspond to either of the two known structures of cobalt. In fact, neither the positions of the peaks nor their intensity distribution correspond to known cobalt phases. After detailed analysis it was concluded that this pattern corresponds to a new, previously unknown phase of cobalt, which we call ε-cobalt. This structure is cubic (space group $P4_132$) with a unit cell parameter a = 6.097±0.001Å. The unit cell structure is similar to that of β-manganese (a high temperature phase of manganese).[9] It contains 20 cobalt atoms, which are divided into two types: 12 atoms of Type I and 8 atoms of Type II (Table 2.1). These two types of atoms differ in their local coordination.

Unlike an ideal close-packed structure, which has 12 nearest neighbors, ε-cobalt has only 3 nearest neighbors for Type I and 2 nearest neighbors for Type II atoms (Table 2.2). This results in a structure for ε-cobalt that is less dense than both the hcp and fcc structures. The calculated density of ε-cobalt is 8.635g cm^{-3}, compared to 8.788g cm^{-3} and 8.836g cm^{-3} for the fcc and hcp structures. The calculated diffraction pattern for the new phase (Figure **2.3b**) is in excellent agreement with experimental data shown in

Table 2.1 Fractional atomic coordinates in the unit cell of ε-cobalt structure

(u=0.20224, v=0.06361)[9]

	x	y	z
Type I			
1	v	v	v
2	v+1/2	1/2-v	1-v
3	1-v	v+1/2	1/2-v
4	1/2-v	1-v	v+1/2
5	3/4-v	3/4-v	3/4-v
6	v+1/4	1/4-v	v+3/4
7	1/4-v	v+3/4	v+1/4
8	v+3/4	v+1/4	1/4-v
Type II			
9	1-u	u+3/4	3/8
10	1/2-u	3/4-u	5/8
11	u	u+1/4	1/8
12	u+1/2	1/4-u	7/8
13	3/8	1-u	u+3/4
14	5/8	1/2-u	3/4-u
15	1/8	u	u+1/4
16	7/8	u+1/2	1/4-u
17	u+3/4	3/8	1-u
18	3/4-u	5/8	1/2-u
19	u+1/4	1/8	u
20	1/4-u	7/8	u+1/2

Table 2.2 Local coordination for the two types of Co atoms in ε-cobalt

	Near neighbor type (number)	Interatomic distance(Å)
Type I	Type I (3)	2.281(9)
	Type II (3)	2.487(2)
	Type II (3)	2.543(4)
	Type II (3)	2.587(0)
Type II	Type I (2)	2.487(2)
	Type I (2)	2.543(4)
	Type I (2)	2.587(0)
	Type II (4)	2.554(6)
	Type II (2)	2.580(1)

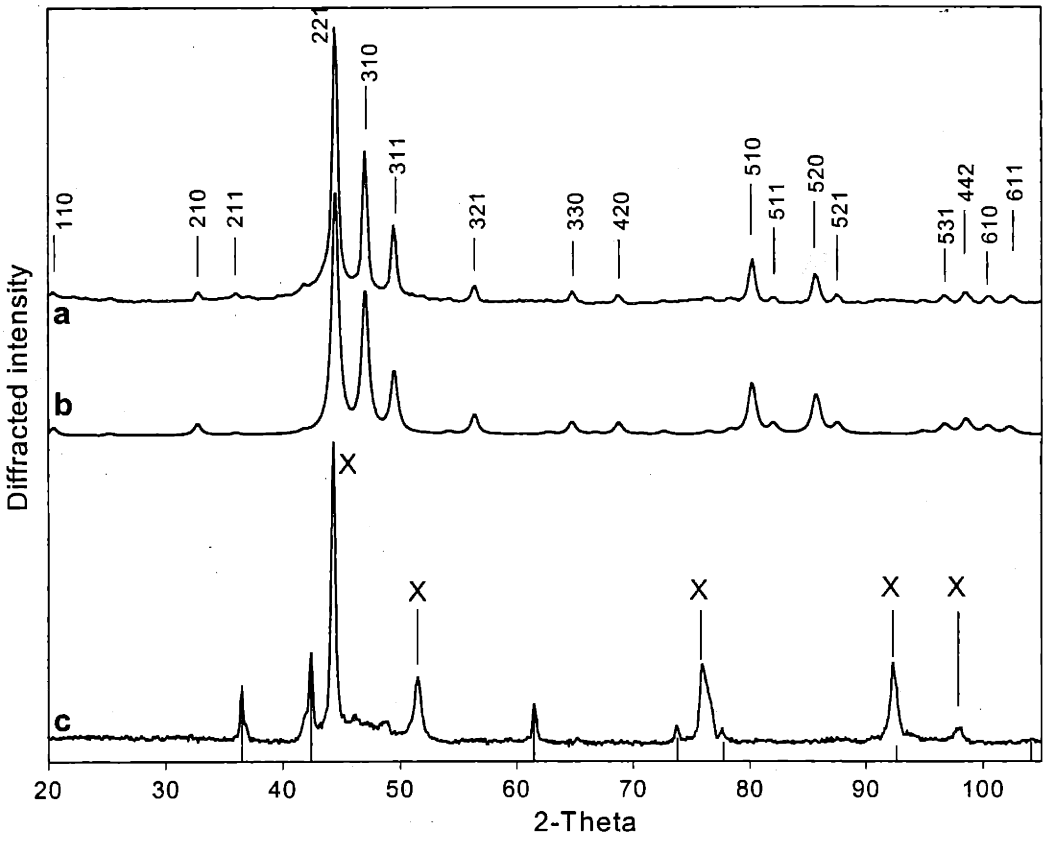

Figure 2.3 X-ray powder diffraction pattern of the ε-cobalt structure: **a** -experimental; **b** -calculated; **c** -the sample shown in **a** after being heated to 500°C, peaks corresponding to fcc cobalt are denoted by X, peaks corresponding to CoO are marked with a stick spectrum.

Figure **2.3a**. Small differences in line shape between theory and experiment are the result of the size distribution in the sample. The pattern in **c** corresponds to a pure fcc structure of cobalt with a small amount of cobalt oxide (CoO) marked with its stick spectrum. The observed sharpening of the peaks is due to sintering and annealing of the crystals. The comparison shows that the experimental pattern is clean and corresponds to a pure ε-cobalt structure. The position and intensity of each peak is precisely reproduced and there are no peaks corresponding to either known cobalt phases or cobalt oxide. The fact that no cobalt oxide peaks are observed in this experiment does not contradict the findings of elemental analysis since a few monolayers of oxide on the particle surface would not provide any significant scattering of x-rays. Numerical values for experimental and calculated peak positions and intensities are shown in Table 2.3. A model unit cell for ε-cobalt is shown in Figure **2.4**.

2.4.5 Magnetic property

The only magnetic property that is specific to the newly discovered structure of ε-cobalt is saturation magnetization because most other magnetic properties are expected to be size dependent in this size range. Since no effort was made it this point to control the size distribution in the samples, the saturation was the only value measured. The magnetic moment per atom in ε-cobalt, measured as 1.70 μ_B, is similar, within our experimental error, to that of the two known structures (1.75 μ_B and 1.72 μ_B for bulk fcc and hcp cobalt).[10]

2.4.6 Metastability and kinetic control of crystallization

The new ε-cobalt phase appears to be metastable under normal conditions. Although stable at room temperature for at least several months, heating the sample shown in Figure **2.3a** to 500°C completely transforms it to the known fcc phase (Figure **2.3c**). Subsequent cooling does not return the sample to its original ε-cobalt structure. The same preparation method but without the presence of TOPO yields nanocrystals with a pure fcc phase. When TOPO is added, ε-cobalt is formed along with fcc cobalt. Increasing the concentration of TOPO in the reaction mixture leads to the exclusive formation of ε-cobalt (Figure **2.5**). Tight coordination of ligand molecules (TOPO)

Table 2.3 Assignments of reflections and comparison between observed and calculated values for ε-cobalt.

2-Theta observed	Intensity observed	hkl	Cell parameter(Å)	2-Theta calculated	Intensity calculated	Calculated d-spacing
32.83	3.3	210	6.1002	32.848	4.5	2.728
36.10	0.6	211	6.0946	36.085	0.8	2.488
44.57	100	221	6.0989	44.585	100	2.033
47.14	55	310	6.0968	47.138	58	1.928
49.59	27	311	6.0970	49.590	25	1.838
64.88	4	330	6.0975	64.886	5	1.437
80.30	22	510	6.0966	80.293	21	1.196
82.15	3	511	6.0968	82.147	4	1.173
85.84	18	520	6.0966	85.832	19	1.132
96.85	4	531	6.0968	96.845	5	1.031
98.67	8	442	6.0981	98.694	8	1.016
100.52	6	610	6.0984	100.544	4.5	1.003
102.40	5	611	6.0980	102.422	4	0.989
			Avg.=6.097±0.001			

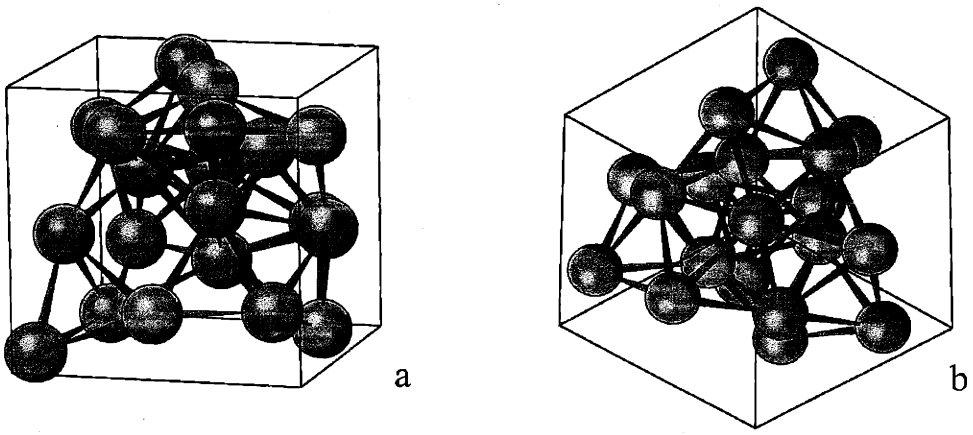

Figure 2.4 The unit cell of ε-cobalt: **a** - unit cell cube filled with 8 atoms of Type I (red) and 12 atoms of Type II (green); **b** - 111-projection of the same cube showing 3-fold symmetry along its main diagonal.

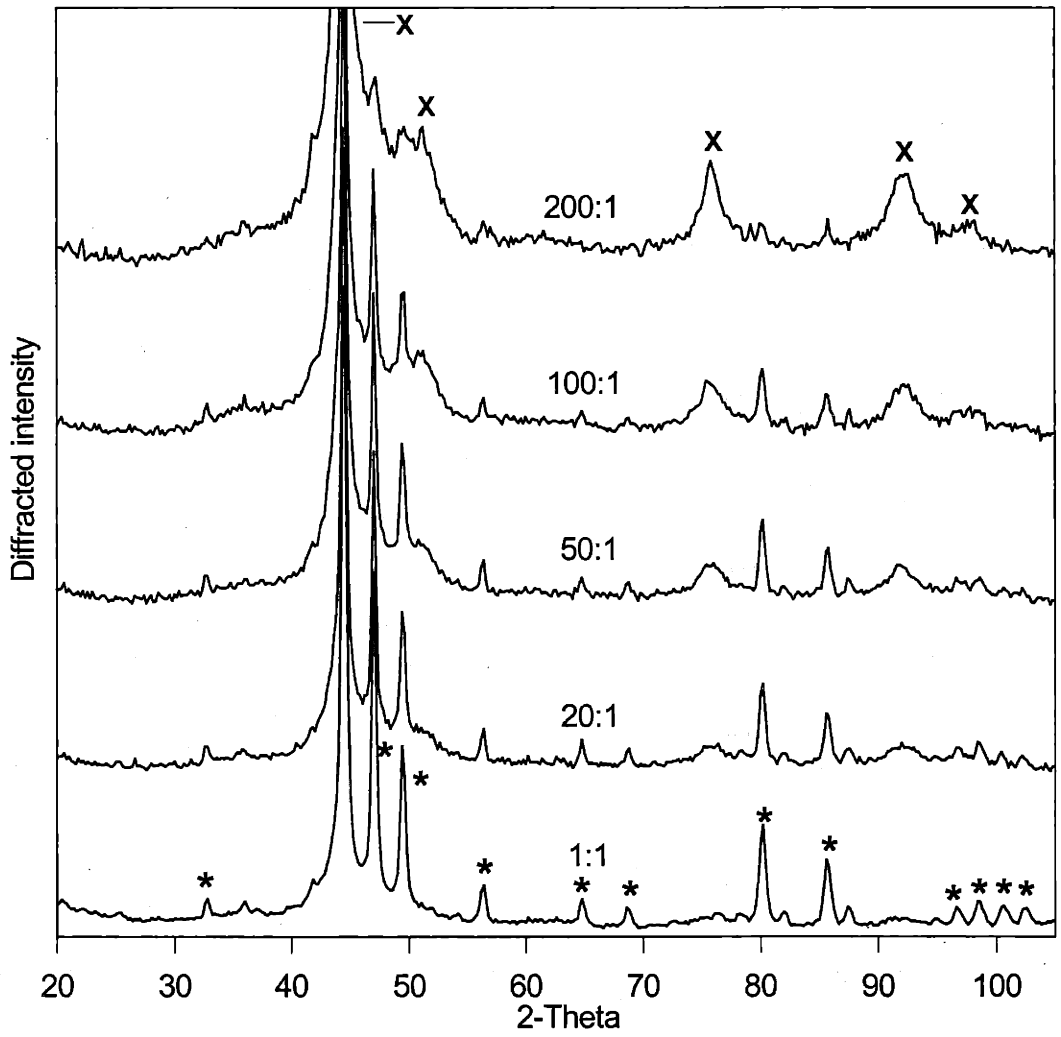

Figure 2.5 Evolution of the X-ray diffraction pattern of cobalt nanocrystals prepared with different concentrations of TOPO. The numbers shown correspond to the ratio of cobalt atoms to TOPO molecules in the reaction mixture. The gradual change from fcc (peaks denoted by X) to ε-cobalt (selected peaks denoted by *) with increasing concentration of TOPO is clearly observed. Sharpening of the peaks corresponding to improved crystallinity of the nanocrystals is also observed.

around the growing crystal and around solublized cobalt atoms is responsible for changing the energetics of growth in favor of the new, less dense phase. Due to its metastability, ε-cobalt may not be accessible by other common techniques, such as varying temperature and pressure. This may be the answer to why ε-cobalt has not been observed before.

The discovery of a new phase for a common element is an example of the critical role that ligands and surfactants can play in determining the resulting structure of crystals grown in solution at low temperatures. Such solution-phase reactions are often controlled kinetically rather than thermodynamically, leading to the initial trapping and growth of metastable phases. It is possible that similar low temperature growth conditions may lead to the discovery of previously unknown structures for other elements and for more complex systems. There is a strong correlation between crystal structure and the magnetic properties of cobalt. The anisotropic high magnetic coercivity hcp phase is the preferred structure for permanent magnet applications (recording media, etc) while the more symmetric low coercivity fcc phase is useful for soft magnetic applications. The newly discovered structure of cobalt may display magnetic properties different from the two previously known structures, and this could be scientifically interesting and technologically useful.

2.4.7 Why "ε-cobalt"?

Some people may be wondering why we named the newly discovered structure of cobalt "epsilon" if it is only the third structure known for cobalt. Here we clarify our reasoning in naming this structure. The two (fcc and hcp) known structures of cobalt have long been referred to as α- and β-cobalt. This is the alternative system of naming the structures according to the letters of Greek alphabet. The problem is that the next possible name (gamma-cobalt) widely refers to a radioactive isotope of cobalt (^{60}Co) used as a source of gamma radiation. In fact, any search of chemical databases for gamma-cobalt will yield multiple references on this subject. In order to avoid confusion, this name was ruled out. The following choice of delta-cobalt was already used by Krainer and Robitsch[4] in reference to the unidentified structure of the material they

obtained from cobalt. Since our structure was different, the next obvious choice was epsilon-cobalt.

2.4.8 The aftermath

It has been three years since ε-cobalt structure was first reported by us at an ACS conference in August 1998. Since that time the structure was confirmed by at least two groups working independently.[11,12] Interestingly, in one case the same structure was observed in cobalt nanocrystals prepared by a reduction of a cobalt salt. Since no trioctylphosphine oxide was used the preparation, it showed that this structure is not specific to one particular preparation method or surfactant, but rather general. The name of ε-cobalt was also well received by the scientific community.

2.5 References

1. Powder diffraction file PDF-2 database sets *1-44*, **1994**.
2. O. Kitakami, H. Satao, Y. Shimada, F. Sato, M. Tanaka, *Phys. Rev. B* **1997**, *56*, 13849-13854.
3. A. W. Hull, *Phys. Rev.* **1921**, *17*, 571-588.
4. E. Krainer, J. Robitsch, *Z. Metallkde.* **1974**,*65*, 729-731.
5. S. Kajiwara, S. Ohno, K. Honma, M. Uda, *Phil. Mag. Lett.* **1987**, *55*, 215-219.
6. D. L. Leslie-Pelecky, M. Bonder, T. Martin, E. M. Kirkpatrick, Y. Liu, X. Q. Zhang, S. H. Kim, R. D. Rieke, *Chem. Mater.* **1998**, 10, 3732-3736.
7. M. Respaud, J. M. Broto, H. Rakoto, A. R. Fert, L. Thomas, B. Barbara, M. Verelst, E. Snoeck, P. Lecante, A. Mosset, J. Osuna, T. Ould Ely, C. Amiens, B. Chaudret, *Phys. Rev. B* **1998**, 57, 2925-2935.
8. Dassenoy F., Casanove M.-J., Lecante P., Verelst M., Snoeck E., Mosset A., Ould Ely T., Amiens C., Chaudret B. *J. Phys. Chem.* **2000**, 112, 8137.
9. C. B. Shoemaker, D. P. Shoemaker, T. E. Hopkins, S. Yidepit, *Acta Cryst.* **1978**, *B34*, 3573-3576.
10. *Landolt-Börnstein* numerical data and functional relationships in science and technology, Vol. *19/a* (Eds.: K.H. Hellwege, O. Madelung), Springer-Verlag, Berlin, **1986**, p. 36.

11. Sun S., Murray C. B. *J. Appl. Phys.* **1999**, 85, 4325.

12. Puntes V. F., Krishnan K. M., Alivisatos P. *Appl. Phys. Lett.* **2001**, 78, 2187.

Chapter 3

Synthesis of Monodisperse Spherical Cobalt Nanocrystals and Their Assembly

3.1 Introduction

Having successfully identified the new crystal structure of cobalt (Chapter 2) here we return to our original goal. The study of the expected size-dependent magnetic properties of magnetic crystals in the nanometer size scale requires the development of a high-quality model system. In this system each sample must have a high degree of uniformity in size and shape, high crystallinity of the magnetic core, and consistent surface derivatization. Such a uniform system should permit us to distinguish between the inherent properties of a particular size nanocrystal from those associated with variations in sample quality, structural inhomogenuity, and polydispersity. We have chosen cobalt nanocrystals as a model system.

In this chapter, we present a method to prepare cobalt nanocrystals in the size range of 3–13 nm in diameter with a narrow distribution ($\sigma < 6\%$) and a choice of internal crystal structure (mixed fcc-hcp or ε-cobalt). These nanocrystals can be dispersed in a variety of solvents that further allows for the preparation of more complex two- and three-dimensional structures with a tunable spacing between lattice sites.

3.2 Background

Several methods for the preparation of metallic magnetic nanoparticles have been described in the past. Many of them include physical techniques such as sputtering and vaporization-condensation.[1-2] These methods generally do not provide sufficient control over the growth process and usually lead to large variations in the size and shape of produced nanoparticles. Moreover, such methods typically involve deposition of the particles on a substrate and do not allow any further processing of nanocrystals. The preparation of 3D ordered structures also appears to be problematic.

The other group of methods involves chemical growth of nanoparticles in solution. This can be accomplished via reduction of metal salts by various reducing

agents[3-6], sonication[7], thermal decomposition of organometallic precursors[8-9,16], or by electrolytic processes[10]. Although these techniques provide several advantages, such as further processability and manipulation of the product, deposition on various substrates, and incorporation into different matrices, most of them do not achieve the required level of control in order to prepare truly uniform samples. Moreover, some recent reports on self-organization of cobalt particles[5,9] did not extend beyond random close packing. However, a handful of methods described in the literature allow for the preparation of monodisperse metallic magnetic nanoparticles with high crystalline quality. The work of Sun and Murray has been particularly successful[6]. They developed a method for preparing nearly monodisperse cobalt nanocrystals with the newly identified ε-cobalt structure[11] by high temperature reduction of cobalt salts. Recently, they achieved similar results synthesizing monodisperse Fe-Pt particles and proposed self-assembled arrays of these nanocrystals as a novel magnetic storage medium with an ultra-high density[12].

3.3 Experimental

3.3.1 General

The synthesis of all samples was carried out under dry nitrogen atmosphere. All chemicals were used as purchased: dicobaltoctacarbonyl (DCOC, 95%) from "Strem"; tributylphosphine (TBP,97%) and trioctylphosphine oxide (TOPO, 90%) from "Aldrich"; trioctylphosphine (TOP, 90%), dioctyl ether (DOE, 97%), sodium carboxylates (stearate – 98%, palmitate – 97%, myristate – 99%, laurate – 99%, caprate – 98%) from "Fluka". Separation of the product from the reaction mixture and the following size-selective precipitation were conducted under regular lab conditions (in the air) using Omnisolv grade solvents purchased from "EM Science". For the preparation of nanocrystalline assemblies an anhydrous solvents were used as purchased from "Aldrich".

3.3.2 **Preparation Method 1** (for cobalt nanocrystals with mixed fcc-hcp structure)

The typical experimental procedure was as follows: 20 ml of DOE and 0.5 ml of TOP were placed in a 100 ml 3-neck round bottom flask equipped with a water-cooled condenser and thermocouple, as shown in Figure **3.1**. The temperature was raised to

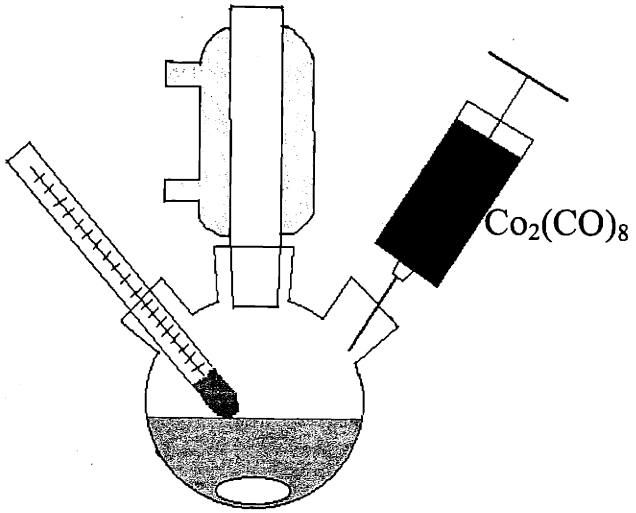

Figure 3.1 Cartoon of the experimental setup employed in the growth of cobalt nanocrystals.

50°C, and the mixture was left under vacuum for two hours to degas and dry. At the same time 0.45g of DCOC was placed in a vial inside a glove box, and 17 ml DOE were added. This mixture was allowed to stir until DCOC was completely dissolved (approx. 30 min). This solution was then filtered through a 0.2 μm syringe filter to remove any undissolved solids and loaded into a syringe. After drying was completed, the flask was flashed several times with nitrogen, and the temperature was raised to 230°C. The heating mantle was then removed, and the content of the syringe taken out of the glove box was quickly injected into the flask. The temperature dropped to 165°C, but was then raised slowly over the course of 30 min by putting the heating mantle back on. An evolution of carbon monoxide was usually observed between 190 and 200°C as the color of the solution gradually changed from brown to black. After the reaction was finished, 0.12g of sodium stearate were added to the flask. The mixture was stirred vigorously for an additional 20 min at 220°C to ensure complete dissolution of stearate and decomposition of the precursor. The heat was then removed and the flask was allowed to cool to room temperature.

This procedure can be modified in two different ways – in order to change the size of the particles produced and the length of the organic chains passivating the surface

of each particle. 1) For the preparation of smaller particles, the amount of TOP is gradually increased to 1 ml. Alternatively, the injection temperature is raised. For bigger particles, the amount of TOP is decreased and the difference compensated by the addition of an equivalent amount of TBP. Decreasing injection temperature also leads to the formation of larger nanocrystals. 2) The length of the capping groups can simply be varied by substitution of shorter chain sodium salts – palmitate ($C_{15}H_{31}$-), myristate ($C_{13}H_{27}$-), laurate ($C_{11}H_{23}$-), caprate (C_9H_{19}-) for stearate ($C_{17}H_{35}$-).

3.3.3 **Preparation Method 2** (for cobalt nanocrystals with pure ε-cobalt structure)

The typical experimental procedure was as follows: 20 ml of DOE and 0.4g of TOPO) were placed in a 100 ml 3-neck round bottom flask equipped with a water-cooled condenser and thermocouple (Figure **3.1**). The temperature was raised to 50°C, and the mixture was left under vacuum for two hours to degas and dry. At the same time 0.45g of DCOC was placed in a vial inside a glove box, and 17 ml DOE were added. This mixture was allowed to stir until DCOC was completely dissolved (approx. 30 min). This solution was then filtered through a 0.2 μm syringe filter to remove any undissolved solids and loaded into a syringe. After drying was completed, the flask was flashed several times with nitrogen, and the temperature was raised to 200°C. The heating mantle was then removed, and the content of the syringe taken out of the glove box was quickly injected into the flask. Following the injection, the temperature dropped to 140°C and the color of the reaction mixture changed from dark brown to deep blue (the complex of DCOC with TOPO). The temperature was then raised to 220 C by putting the heating mantle back on. After a while, the color of the solution gradually changed from brown to black. After the reaction was finished, 0.12g of sodium stearate were added to the flask. The mixture was stirred vigorously for an additional 20 min at 220°C to ensure complete dissolution of stearate and decomposition of the precursor. The heat was then removed and the flask was allowed to cool to room temperature.

3.3.4 **Product Separation and Size-Selection**

In order to separate the product, the reaction mixture is transferred to an Erlenmeyer flask. A small amount of black magnetic material accumulated on the stirbar

is washed off with hexane and added to the flask. This mixture is sonicated for 5min to dissolve any aggregated product, and ethanol is slowly added to the flask until the solution turned cloudy. (To facilitate the dispersion of aggregated nanocrystals, 1-2 drops of oleic acid may be added to hexane prior to sonication.) A few extra ml of ethanol are added to ensure complete precipitation of the particles. The product is then separated from the supernatant as a black greasy residue by centrifugation. The supernatant is discarded, and the solid precipitate is dried under vacuum. The resulting black powder is readily redispersed in the variety of alkanes, aromatics, and chlorinated solvents. Size distributions of 10% can be achieved at this stage before any further processing with yields close to 100% since the reaction is always carried out to the completion. To further reduce the size distribution of the nanocrystals size-selective precipitation is performed by slow addition of ethanol just to the point of initial flocculation followed by centrifugation[13-14]. This allows separation of the portion with the larger particles in the distribution while discarding the portion containing the smaller ones. Two or three size-selections are typically enough to ensure a narrow (5-7%) size distribution in the resulting samples with a yield of 50% or better.

3.3.5 Preparation of 2D and 3D Close-Packed Structures

Dropcasting of a concentrated (hexane, nonane) solution of nanoparticles on a variety of substrates led to the formation of close-packed "glassy films". The "supercrystals" of cobalt nanoparticles were formed upon slow evaporation of a warm (60°C) solution (97%-nonane, 3%-octanol) deposited on a silicon wafer or TEM grid coated with amorphous carbon at room temperature. In the case of 2D superlattices, the concentration of solution had to be adjusted in order to create one monolayer coverage of the substrate surface.

3.4 Results and Discussion

3.4.1 Nucleation and Growth

The general approach for producing uniform colloidal particles in solution, worked out by La Mer and Dinegar[15], consists of very fast and homogeneous nucleation

phase followed by a slow growth phase of the previously formed nuclei. The general kinetics of this mechanism is shown on Figure 3.2. This strategy was particularly successful in preparation of II –VI semiconductor nanocrystals developed by Murray et al.[13] In our case fast nucleation was accomplished by rapid injection of the precursor (DCOC), which starts to decompose at as low as 50°C, into a flask containing solvent at 230°C. Upon injection, a small portion of the precursor decomposes instantly forming tiny nucleation centers. The remaining portion of the precursor gets retained in a molecular form by forming a complex compound with trialkylphosphine (or trialkylphosphine oxide) present in the flask. In the case of TOP, the complex has a

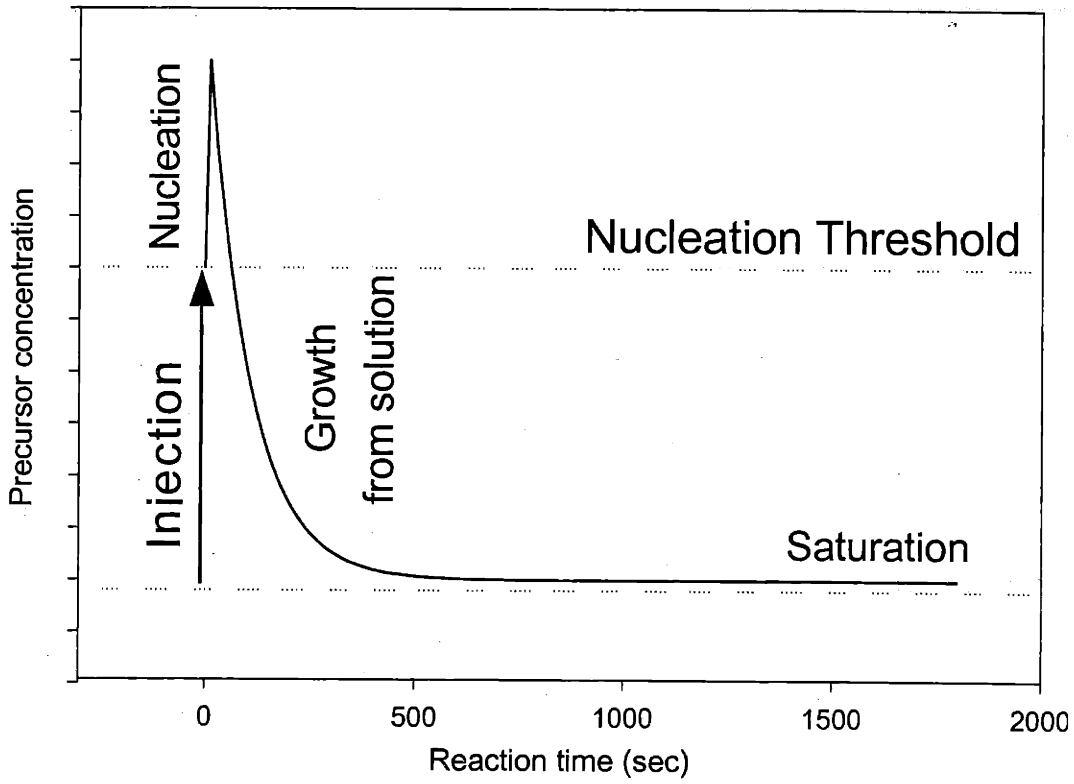

Figure 3.2 General kinetics of monodisperse colloidal growth mechanism described by La Mer and Dinegar.[15]

bright brown color with absorption maximum at 375 nm and is stable at temperatures below 180°C. Provided that after injection the temperature in the flask drops well below 180°C, this portion of the precursor is largely responsible for the growth of the crystals upon slowly raising the temperature above 180°C. The growth of the cobalt nanocrystals in the presence of TOP appears to be irreversible. Unlike similar procedure for semiconductor particles, which can grow further by the mechanism of "Ostwald ripening," cobalt nanoparticles do not show any change in their size or composition upon prolonged heating after complete depletion of precursors in the reaction mixture. In fact, the growth of the particles stops when all of the precursors have decomposed. A possible explanation is that the TOP-Co complex has a higher free energy in solution than TOP complexed to a Co surface. This would inhibit Ostwald ripening, making TOP an additive that acts as a growth inhibitor by binding tightly to the Co surface. In the presence of TOPO, however, the growth mechanism appears quite different from that of TOP. Although both TOPO and TOP proved to be good coordinating ligands, TOPO appears to have a higher binding energy for cobalt compared to TOP, enabling it to remove cobalt atoms from the high-energy surface of a nanocrystal. In other words, it appears that the free energy of a TOPO-Co complex in solution is slightly lower than that of TOPO bound to the Co surface. TOPO appears then to aid in the ripening process and promotes growth and annealing by keeping an equilibrium population of TOPO-Co complexes in solution. In this case, even after the initial decomposition of the precursors is complete, the growth of larger nanocrystals can continue at the expense of smaller ones, making the overall time of the growth an additional size control factor. The role of TOPO here is then similar to its role in the growth of semiconductor nanocrystal. Similar findings on this mechanism were recently reported by Puntes et al.[16]

In the case of both TOP and TOPO the size of the resulting particles is determined by the concentration ratio of the precursors vs. coordinating ligands. Increasing the concentration of DCOC in the reaction mixture while keeping the amount of other reagents constant leads to the formation of larger particles. Alternatively, an increase in the concentration of coordinating ligands – TOP or TOPO leads to the formation of smaller crystals. Due to the equilibrium between the concentrations of these ligands in solution and on the surface of the growing particles, the increased ligand concentration

leads to a more complete coverage of the surface and, therefore, inhibits further growth. The length of alkyl-chain on the phosphines also has an effect on the size of the resulting crystals: the longer alkyl chain in trioctylphosphine provides greater steric hindrance to the growth of the nanocrystals than the shorter alkyl chain of tributylphosphine, leading to smaller particles.

Although trialkylphosphines or their oxides prove useful in mediating the nucleation and controlling the growth via reversible coordination around the growing particles, they are unable to prevent the nanocrystals from aggregating after their separation from the reaction mixture. This is due to rather weak and reversible binding of trialkylphosphines and trialkylphosphine oxides to the cobalt surface at room temperature, which requires a significant excess of capping molecules in solution in order to keep a portion of them attached to the surface of the particles. Protecting Co nanocrystals from aggregation is more challenging compared to other non-magnetic types of nanoparticles since the particles are subjected to both van der Waals and magnetic attractive force. For the same size cores, Co particles generally required longer alkyl chain capping molecules compared to their semiconductor counterparts. This is accomplished by using small amounts of long-chain sodium carboxylates, which strongly bind to the particle surfaces and therefore remain attached during separation, size-selective processing, and redispersion in various non-polar solvents. The longest surfactant (sodium stearate) proved effective in stabilizing Co particles for the complete size range up to 13 nm in diameter. Shorter chains can be used to stabilize smaller particles.

Another important function of the capping groups is to protect the Co core from oxidation upon their exposure to air. A bare cobalt surface is extremely reactive toward oxygen. In fact, Co particles prepared in a similar fashion but without addition of surface passivating molecules oxidize immediately when exposed to air with a dramatic red glow. Well-passivated nanocrystals, on the other hand, oxidize much slower and can retain their magnetic properties intact for a few days after being processed in air and gradually oxidize with a time scale of several weeks (for details, see Chapter 5).

3.4.2 Formation of 2D and 3D Structures

Formation of these close-packed structures was accomplished by well known self-assembly techniques, which have been successfully applied for cadmium selenide[17], gold[18], silver[19], and, recently, cobalt[6, 20] nanoparticles. There are two major requirements for a successful self-assembly. First, the particles have to be very uniform in size and shape, with the polydispersity not exceeding 8-10%. Second, the right combination of solvents and other parameters (such as temperature, pressure, speed of crystallization, etc.) must be found in order to provide the most favorable conditions for crystallization. Generally, these conditions include slow destabilization of particles in solution by adjusting the solvent composition, which leads to a reversible and controlled crystallization. If these conditions are not met, amorphous or relatively disordered structures are usually formed. Figure **3.3** shows the result of dropcasting out of concentrated hexane solution. TEM and electron diffraction analysis confirms that this structure is indeed a close-packed glassy solid. The same sample deposited from the mixture of solvents (see above) at elevated temperature is shown in Figure **4.4**. In this case, the process of crystallization was much slower (about 2 hours compared to 1 min. for hexane). Since the high-boiling polar component (1-octanol) evaporates more slowly than the nonpolar one (nonane), the solution gradually shifts toward a more polar mixture. This, in turn, forces particles out of solution and leads to a well-ordered fcc-superlattice. The ratio of the polar/nonpolar solvent in the proper mixture also depends on the size of the ordering nanocrystals. Small particles, with minimal attraction between them, require a stronger driving force for close-packing and therefore a more polar solvent, where as the largest particles may not require the second (polar) solvent at all.

3.5 References

1. Hayashi T., Hirono S., Tomita M., Umemura S. *Nature* **1996**, 381, 772.

2. Yamamuro S., Sumiyama K., Kamiyama T., Suzuki K. *J. Appl. Phys.* **1999**, 86, 5726.

3. Yiping L., Hadjipanayis G. C., Sorensen C., M., Klabunde K., J. *J. Appl. Phys.* **1990**, 67, 4502.

4. Osuna J., de Caro D., Amiens C., Chaudret B., Snoeck E., Respaund M., Broto J.-M., Fert A. *J. Phys. Chem.* **1996**, 100, 14571.

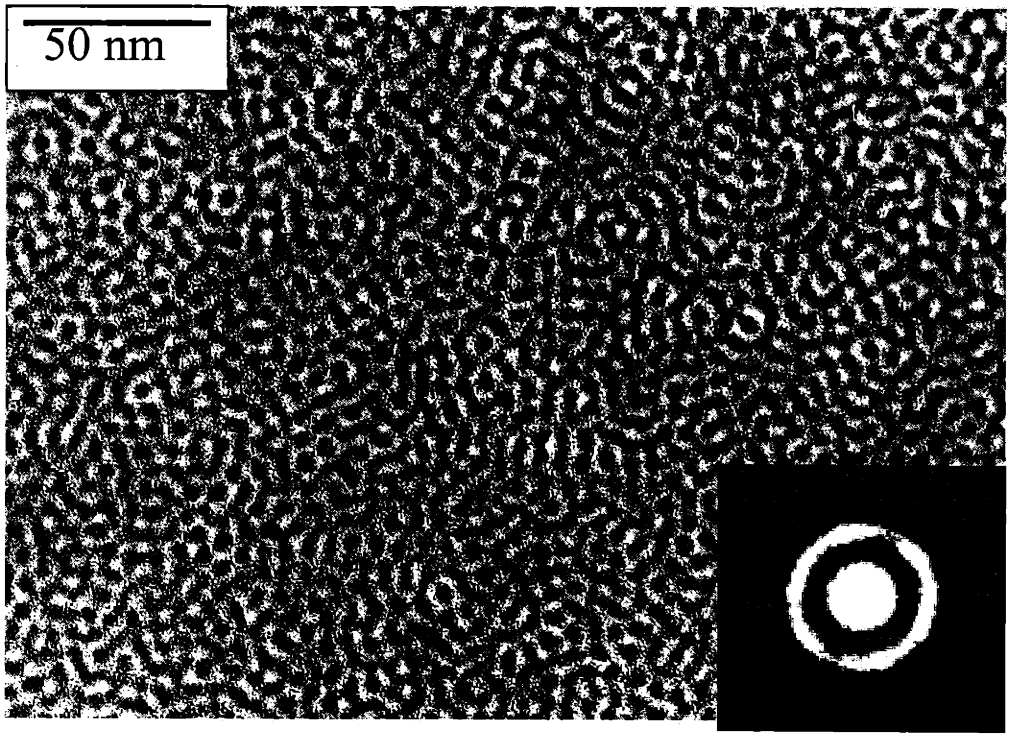

Figure 3.3 TEM image of close-packed 4nm cobalt nanocrystals (the same sample as on Figure 4.4) dropcast from concentrated hexane solution; no long-range order is observed. Small angle electron diffraction (inset) shows ring typical for an amorphous material.

5. Petit C., Taleb A., Pileni M.-P. *Adv. Mater.* **1998**, 10, 259.

6. Sun S., Murray C. B. *J. Appl. Phys.* **1999**, 85, 4325.

7. Gibson C. P., Putzer K., J. *Science* **1995**, 267, 1338.

8. Thomas J. R. *J. Appl. Phys.* **1966**, 37, 2914.

9. Yin J. S., Wang Z. L. *NanoStructured Materials* **1999**, 11, 845.

10. Becker J. A., Schäfer R., Festag R., Ruland W., Wendorff J.H., Pebler J., Quaiser S. A., Helbig W., Reetz M. T. *J. Chem. Phys.* **1995**, 103, 2520.

11. Dinega D. P., Bawendi M. G. *Angew. Chem. Int. Ed.***1999**, 38, 1788.

12. Sun S., Murray C. B., Weller D., Folks L., Moser A. *Science*, **2000**, 287, 1989.

13. Murray C. B., Norris D. J., Bawendi M. G. *J. Am. Chem. Soc.***1993**, 115, 8706.

14. Chemseddine A., Weller H. *Ber. Buns. Ges.* **1993**, 97, 636.

15. LaMer V. K., Dinegar R. H. *J. Am. Chem. Soc.* **1950**, 72, 4847.

16. Puntes V. F., Krishnan K. M., Alivisatos A. P. *Science* **2001**, 291, 2115.

T., Amiens C., Chaudret B. *J. Phys. Chem.* **2000**, 112, 8137.

17. Murray C. B., Kagan C. R., Bawendi M. G. *Science* **1995**, 270, 1335.

18. Andres R. P., Bielefeld J. D., Henderson J. I., Janes D. B., Kolagun V. R. *Science* **1996**, 273, 1690.

19. Harfenist S. A., Wang Z. L., Alvarez M. M., Vezmar I., Whetten R. L. *J. Phys. Chem.* **1996**, 100, 13904.

20. Puntes V. F., Krishnan K. M., Alivisatos P. *Appl. Phys. Lett.* **2001**, 78, 2187.

Chapter 4

Structural Characterization of Individual Nanocrystals and Their Assemblies

4.1 Introduction

Having succeeded in the preparation of nearly monodisperse cobalt spheres we accomplished the first part of building our model system – we achieved minimal size and shape variation in our samples. The second part is to investigate the internal morphology of our nanocrystals and to assess the possible variations in crystallinity, surface derivatization, etc., and also to explore the ways to minimize those variations.

In this chapter we employ a set of standard characterization techniques, such as elemental analysis, transmission electron microscopy, electron diffraction, and X-ray diffraction analysis combined with structural simulations to build a consistent model for the structure of individual nanocrystal. Moreover, we explore the morphology of nanocrystalline assemblies and their dependence on the size of comprising nanocrystals.

4.2 Experimental

4.2.1 Elemental Analysis

Quantitative elemental analysis of the reaction product was carried out on thoroughly washed and dried powders of nanocrystals using inductively coupled plasma - atomic emission spectrometry to determine the metal content and combustion studies to measure organic content (carbon and hydrogen). These studies were performed by Galbraith Laboratory in Tennessee.

4.2.2 Transmission Electron Microscopy and Diffraction

Low-resolution TEM studies were conducted in a bright field mode using a JEOL 2000FX microscope. The smallest objective aperture was used for imaging of individual particles to produce high Z-contrast pictures. The electron diffraction patterns of superlattices were obtained at 280 cm camera length by selecting the desired area of the

sample with appropriate size diffraction aperture. High-resolution imaging was performed on JEOL 2010 microscope. A number of different size apertures were selected to permit the imaging of desirable lattice projections. Both instruments were operated at 200 kV and had LaB_6-based filaments. Copper grids (400 mesh) coated with a thin layer of amorphous carbon (3-4 nm) were purchased from *Ted Pella, Inc.* The samples were prepared by dropcasting from dilute hexane solutions or, in the case of superlattices, from specially prepared mixed solutions (see above).

4.2.3 X-ray Powder Diffraction

X-ray powder diffraction patterns were recorded on Rigaku Rotaflex 250 mm radius diffractometer with Cu-anode radiation. The accelerating voltage was set at 60 kV with 300 mA flux. The samples were prepared from freshly synthesized and thoroughly washed and dried powders by either pressing a 0.5 in. diameter pellets or depositing the powder directly on a substrate containing an adhesive surface. A variety of slits as well as appropriate step-size and collection time were used to achieve desirable resolution/intensity signals.

4.3 Results and Discussion

4.3.1 Elemental Analysis

The sample for elemental analysis was prepared after three consecutive size-selections and contained 10 nm diameter particles. The results were as follows: cobalt – 76.5%, sodium – 1.1%, carbon – 9.3%, hydrogen – 1.8%. A trace amount of phosphorous was also detected. The other 11.3% remained unaccounted and attributed mostly to oxygen as well as experimental error. Two main conclusions can be drawn from these results. First, the amounts of carbon, hydrogen, and sodium are consistent with the stoichiometry of the capping molecule – sodium stearate ($C_{18}H_{35}O_2Na$). Assuming that the amount of sodium is correct, the corresponding amounts of carbon and hydrogen based on the formula should be 10.3% and 1.67%, respectively. This is in a good agreement with experiment and within experimental error. This amount of surfactant should also account for 1.5% of the total oxygen content. The additional

amount of oxygen comes from the oxidation of the cobalt surface upon exposure to air. Since no cobalt oxide was observed in x-ray diffraction or in TEM analysis, the amount of cobalt oxide must be limited to a few monolayers on the surface of the particles, and should be on the order of a few to about 10% by weight depending on the size of the nanocrystals.

Second, the coverage of the nanocrystalline surface with surfactant (sodium stearate) can be estimated from the ratio of sodium (or carbon) atoms to cobalt atoms and the size of the nanocrystals (10 nm). The calculated value for the area per adsorbed molecule in our case yields 46 $Å^2$, which is well within the range of values for typical long chain anionic surfactants (40 – 55 $Å^2$)[1], indicating a complete close-packed coverage of the nanoparticle surface.

4.3.2 Transmission electron microscopy and diffraction

Transmission electron microscopy allows direct observation of nanocrystals and their assemblies, thereby making possible precise measurements of their sizes and shapes. In addition, high-resolution imaging provides useful information about the internal morphology of the particles, presence of defects, etc. Electron diffraction is a convenient tool for investigating the internal structure of the superlattices.

Figure **4.1** shows high-resolution TEM images of single cobalt nanocrystals prepared with the use of TOP (**a**, **b**) and TOPO (**c**). The projection in Figure **4.1a** shows no defects with the measured spacing between the planes of 2.06 Å. These planes correspond to the $<111>_{fcc}$-projection (d=2.046 Å) or $<002>_{hcp}$-projection (d=2.03 Å) of the cobalt lattice. The fact that this projection does not show any defects is in good agreement with the model developed after analysis of the x-ray diffraction data. If stacking faults along the $<111>_{fcc}$-direction are, indeed, the main defects present in our nanocrystals, they will not appear in the $<111>_{fcc}$-projection, but should appear in all other projections. Although the $<111>_{fcc}$-projection does not show any defects in the alignment of atomic planes, a variation in image contrast is observed throughout the particle. Two opposite ends of the image appear much darker than the middle. Since the scattered intensity in the TEM is dependent on the orientation of the crystal, this indicates a change in the orientation of the underlying lattice (three areas of different contrast

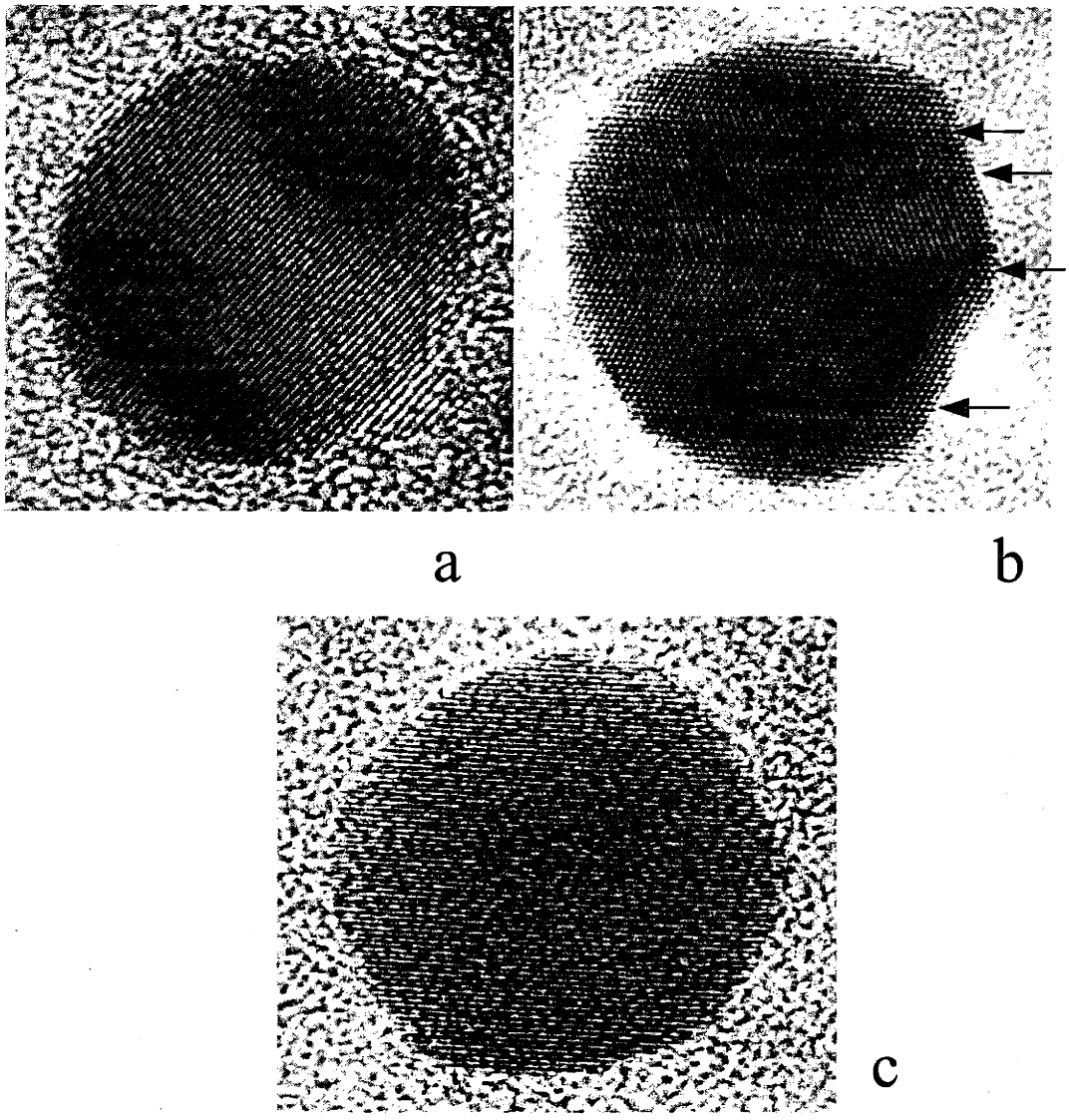

Figure 4.1 High-resolution TEM image of: **a** - the $<111>_{fcc}$ or $<002>_{hcp}$ -projection in single cobalt nanocrystal; the stacking of atomic planes (2.06 Å spacing) in this direction shows no visible defects; **b** - the <110>-projection (2.5 Å spacing) shows a number of stacking faults per particle; **c** - the <221>-projection (1.99 Å) of ε-cobalt shows no defects; all other projections also show no defects.

separated by two stacking faults). Since this specific (defect free) orientation is relatively rare compared to all other possible orientations, only a small fraction of nanocrystals appear as defect free. The majority of particles (with all other possible orientations with respect to the electron beam) shows a number of defects. For example, Figure **4.1b** shows the $<110>_{fcc}$-projection of a nanocrystal. As expected, at least three faults are clearly observed. This further validates our model.

Similar TEM analysis of ε-cobalt nanocrystals prepared with TOPO (Figure **4.1c**) showed no visible defects for the great majority of particles regardless of their orientation, confirming the presence of truly single crystals deduced from the x-ray analysis.

The morphology of 2D and 3D supercrystals grown out of nanoparticles was further investigated. Wang et al.[2] recently reported a deviation from the conventional close packing in the assembly of cobalt nanocrystals prepared by the method of Sun and Murray[3]. The reason for such a deviation was given as the polyhedral shapes of nanocrystals with highly developed facets. In our case, however, the particles appeared to have a spherical shape and, therefore, assembled in the conventional manner. Figure **4.2a** shows a close-packed monolayer of 8 nm cobalt particles prepared with the use of TOP. These particles have a roughly spherical shape with a size distribution of 7%. Spacing between the particles is controlled by the length of the organic molecules attached to the particle surface and can be varied in the range of 2-4 nm by using commercially available reagents. The spacing of 4 nm as in Figure **4.2a** corresponds to a pair of non-penetrating stearate capping groups ($C_{17}H_{35}$-) bound to the particle surface. Shorter coordinating agents (palmitate –$C_{15}H_{31}$-, myristate – $C_{13}H_{27}$-, laurate – $C_{11}H_{23}$-, caprate – C_9H_{19}-) led to smaller interparticle distance. The only limiting factor in varying the spacing was the reduced stability of larger particles protected by shorter hydrocarbon chains. For example, 8 nm and larger particles could be stabilized only by palmitate and stearate, whereas shorter capping groups led to significant aggregation. A monolayer of 12 nm ε-cobalt nanocrystals prepared with the use of TOPO is shown in Figure **4.2b**. A significant increase in the concentration of the deposition solution leads to the formation of 3D "supercrystals" (inset in Figure **4.3**). The size of the crystals can extend from sub-micron to tens of microns depending on deposition conditions. The crystals

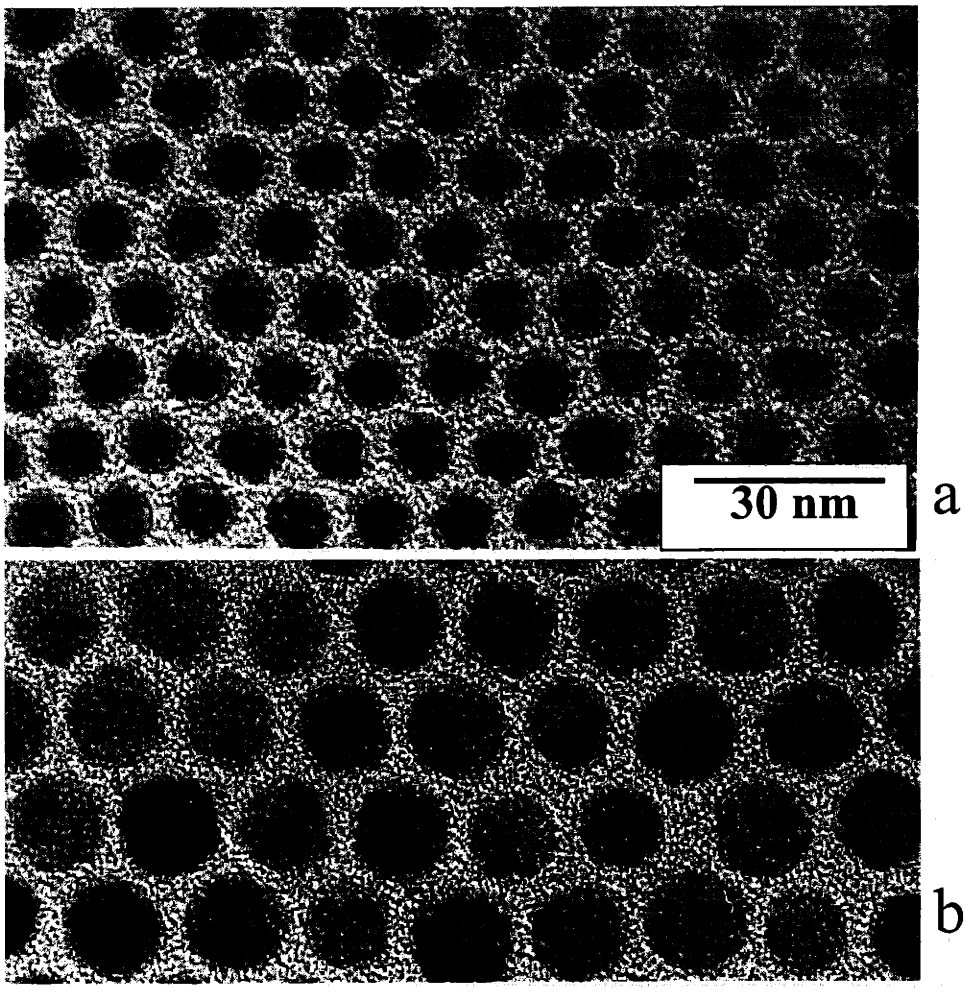

Figure 4.2 **a** - close-packed monolayer of 8 nm cobalt particles prepared with TOP; 4 nm spacing corresponding to two non-penetrating stearate surface ligands; **b** - a monolayer of 12 nm ε-cobalt nanocrystals (4 nm spacing) prepared with TOPO.

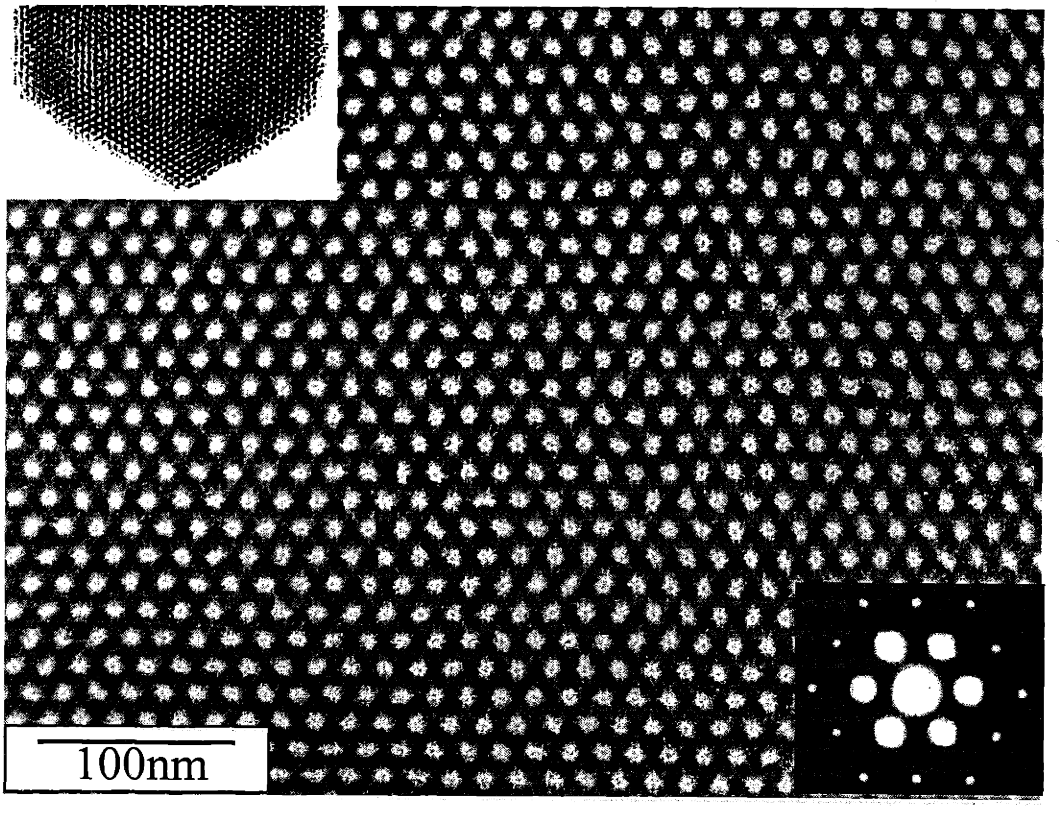

Figure 4.3 TEM image of the <111>-projection of three-dimensional hcp-superlattice formed by dropcasting 9 nm cobalt nanocrystals from the mixed solvent; inset on the right shows well defined facets of the supercrystal; small angle electron diffraction pattern shows lateral perfection of the superlattice.

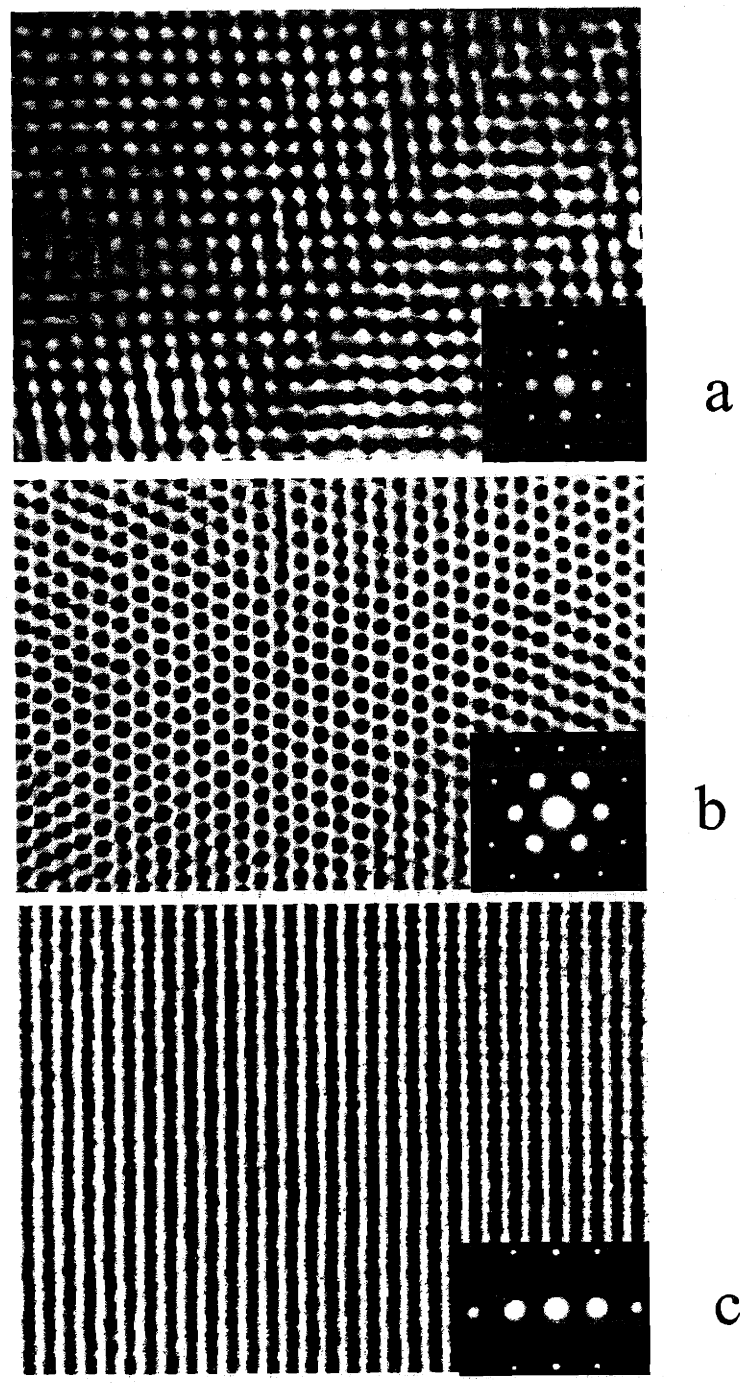

Figure 4.4 TEM images of the three main projections of fcc-superlattice and their corresponding electron diffraction patterns formed by dropcasting 4.1 nm nanocrystals: **a** - <100>, **b** - <110>, **c** - <211>.

usually have a triangular or a hexagonal shape with well-developed facets. A closer analysis reveals hexagonal close-packed ordering in the superlattice (Figure **4.3**). In this structure, every other close-packed monolayer parallel to the substrate surface is situated exactly above each other, thus leading to an ABAB..... sequence of stacking. The third possible C- positions always remain vacant. This leads to a buildup of the contrast upon increasing thickness of the crystal in the TEM image taken along <111>-projection. A small angle electron diffraction pattern, shown in inset, demonstrates the lateral perfection of the superlattice.

Although self-assembly of cobalt nanocrystals always led to the formation of close-packed structures, the type of the superlattice appeared to be size-dependant. The larger particles (8-12 nm) preferentially formed an hcp-lattice (as in Figure **4.3**). However, smaller particles (3-5 nm) tend to form fcc-lattice. Three main projections of such a lattice are shown in Figure **4.4**. The fourth main <111>-projection is not shown because of poor contrast in the TEM. Unlike the hcp-structure, in the fcc-lattice all three possible positions for close-packed layers are equally occupied, leading to an ABCABC type of structure. This structure lacks the long empty channels parallel to the electron beam, which give an hcp-lattice its high contrast. As a result, the density of the crystal appears uniform and Z-contrast disappears.

The change in the type of the superlattice from fcc to hcp with increasing particle size may be due to the influence of magnetic dipolar interactions, which increase with the particle size.

4.3.3 X-ray Diffraction and Structural Simulations

X-ray diffraction patterns are primarily sensitive to the size, shape, and symmetry of underlying crystalline lattice of the nanocrystals in analogy to TEM lattice contrast imaging. Unlike TEM, though, X-ray diffraction probes a statistically large number of crystallites and therefore can be combined with the observations of TEM to construct a representative model of average crystallite structure and morphology.

Cobalt nanocrystals prepared with the use of TOP. An experimental x-ray powder diffraction pattern of cobalt nanocrystals prepared with the use of TOP is shown

in Figure **4.5a**, where the fcc-pattern of cobalt is represented by a stick spectrum. Visual analysis of this pattern shows evidence of finite size broadening in all reflections (see inset in Figure **4.5**). For smaller particles several peaks significantly overlap. Although the experimental spectrum appears to be similar to the fcc-pattern, the positions of several lines are shifted from their original locations. The relative intensities also appear anomalous. In order to understand the nature of these deviations, structural simulations were undertaken.

The Debye equation that is valid in the kinematical approximation is shown below:

$$I(q) = I_0 \sum_m \sum_n F_m F_n \frac{\sin(q \cdot r_{m,n})}{q \cdot r_{m,n}}$$

where I(q) is the scattered intensity, I_0 is the incident intensity, q is the scattering parameter ($q = 4\pi\sin(\theta)/\lambda$) for X-ray of wavelength λ diffracted through the angle θ, F_m and F_n are the atomic scattering factors of atoms m and n with $r_{m,n}$ distance between them. A discrete form of the Debye equation[4] is shown below:

$$I(q) = I_0 \frac{f^2(q)}{q} \sum_k \frac{\rho(r_k)}{r_k} \cdot \sin(q \cdot r_k)$$

where f(q) is the angle dependent scattering factor. The summation is over all interatomic distances, and $\rho(r_k)$ is the number of times a given distance r_k occurs. Since the number of discrete interatomic distances in an ordered structure grows much more slowly than the total number of distances, using the discrete form of the equation is significantly more efficient in the simulation of large crystallites.

The simulations were performed as follows[5,6,7]. First, the diffraction pattern was calculated using the discrete form of the Debye equation for a single spherical particle of certain size having pure fcc structure. Then stacking faults were successively introduced into the particle until the pure hcp structure was reached. For each number of faults the corresponding pattern was calculated. In all calculations interatomic distances remained unchanged relative to the bulk cobalt. Thermal effects were simulated by the introduction of a Debye-Waller factor. A constant Debye-Waller factor was used based on a mean-square displacement of 0.03 $Å^2$ for each cobalt atom. The resulting spectra

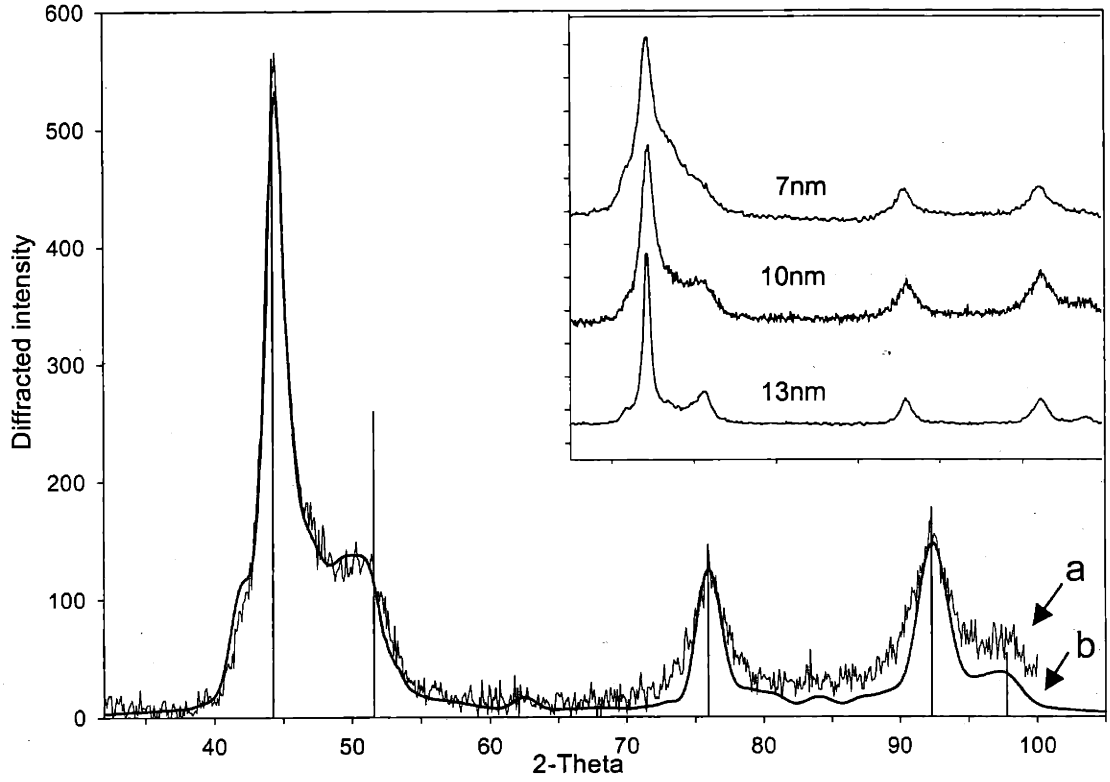

Figure 4.5 **a** - experimental x-ray powder diffraction of 10 nm cobalt nanocrystals prepared with the use of TOP; **b** - simulated pattern for a mixture of 10 nm spherical particles containing pure fcc structure (15.6%), pure hcp structure (11.5%), and a mixed structure containing from 1 to 7 stacking faults per particle (72.9%). The inset shows the size evolution of XRD patterns.

were then statistically weighted by a Gaussian distribution and added together to mimic the distribution of particles with random numbers of defects in the powder. The distributions were usually centered around three to five stacking faults per nanocrystal depending on size, so that the overall density of defects remained constant. The evolution of the diffraction pattern for a single 10 nm cobalt particle with an increasing number of stacking faults is shown in Figure **4.6**. This clearly demonstrates the sensitivity of the pattern to the defects. The presence of just one stacking fault in the particle leads to a significant change in the spectra [**a** to **b** and **e** to **f**]. Our simulations show that the experimental pattern can be reproduced very accurately assuming that the product consists of a mixture of particles ranging from pure fcc to pure hcp structure with a distribution of stacking faults. As a result, the diffraction patterns generally consist of five peaks, similar to pure fcc-cobalt, with each peak being slightly shifted from its original position. Furthermore, each peak (including the strongest $<111>_{fcc}$-reflection) undergoes significant broadening due to the presence of the stacking faults. These peaks, therefore, become almost insensitive to the overall size of the crystal. In the case of an ideal hcp lattice, the width of the $<002>_{hcp}$- peak (or its equivalent $<111>_{fcc}$ peak) should not be affected by the presence of stacking faults along this direction of the crystal. However, the hcp structure of cobalt deviates from the ideal case through its closer packing of planes than the fcc lattice. The position of the $<002>_{hcp}$-peak does not, therefore, coincide with the $<111>_{fcc}$-peak, but it is shifted to higher angles. Since the difference in d-spacing is rather small (2.046 Å for fcc vs. 2.03 Å for hcp)[8], these peaks significantly overlap, and the combined broad peak shifts to the right. As a result, all the peaks in the pattern are affected by the presence of stacking faults, and none can serve as a rough measure of the crystal size (see inset in Figure **4.5**). The widths of the peaks in this case serve as a measure of defect free regions of the crystals rather than of a total crystalline size. Since the density of the stacking faults remains almost constant for the whole size range the widths of the peaks exhibit very weak dependence on the overall particle size. The simulated pattern is shown in Figure **4.5b**. It demonstrates, indeed, a good agreement with the experiment.

Cobalt nanocrystals prepared with the use of TOPO. The x-ray diffraction pattern for 12 nm cobalt nanocrystals (depicted in Figure **4.2b**) prepared with the use of

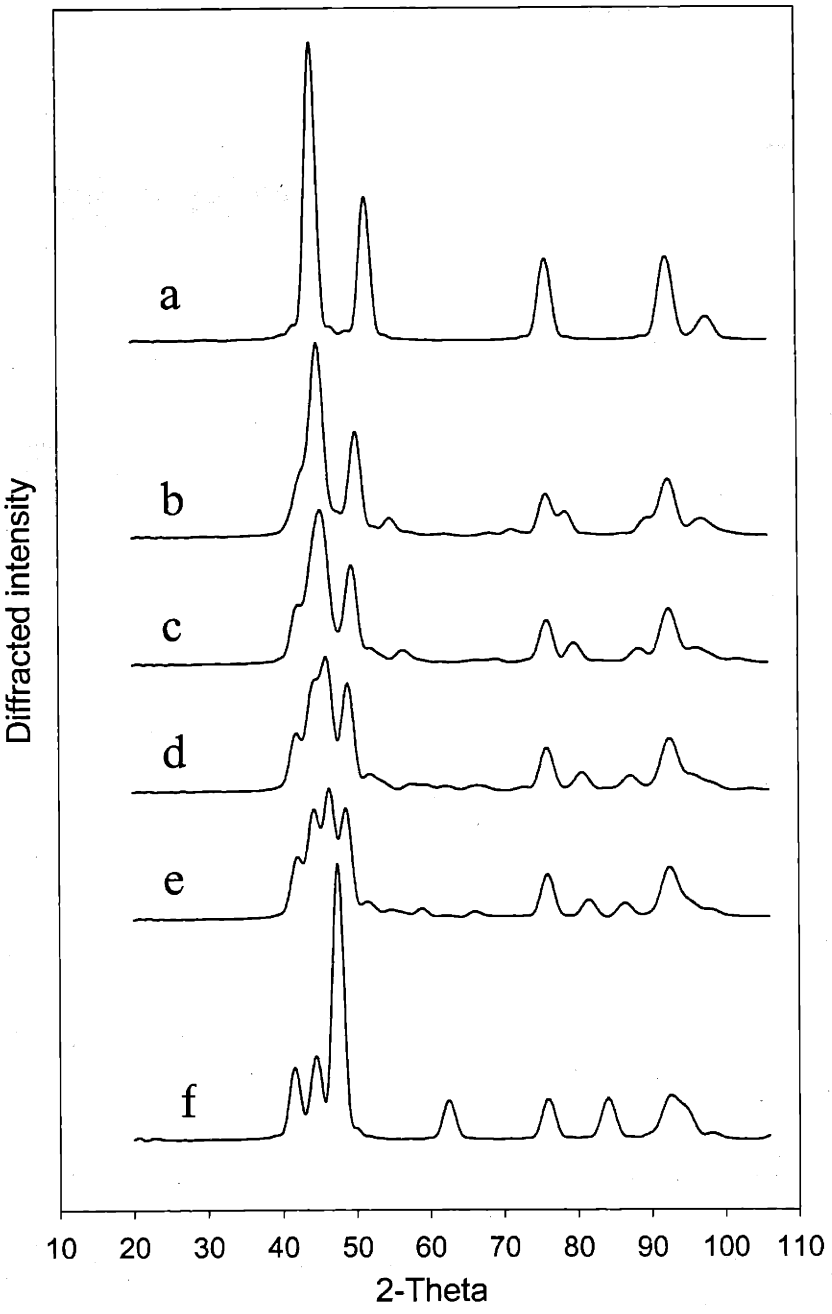

Figure 4.6 Evolution of simulated XRD pattern for a single 10 nm cobalt particle upon successive introduction of stacking faults into the lattice: **a** - pure fcc, **b** - fcc with one fault, **c** - fcc with two faults, **d** - fcc with three faults, **e** - hcp with one fault, **f** - pure hcp.

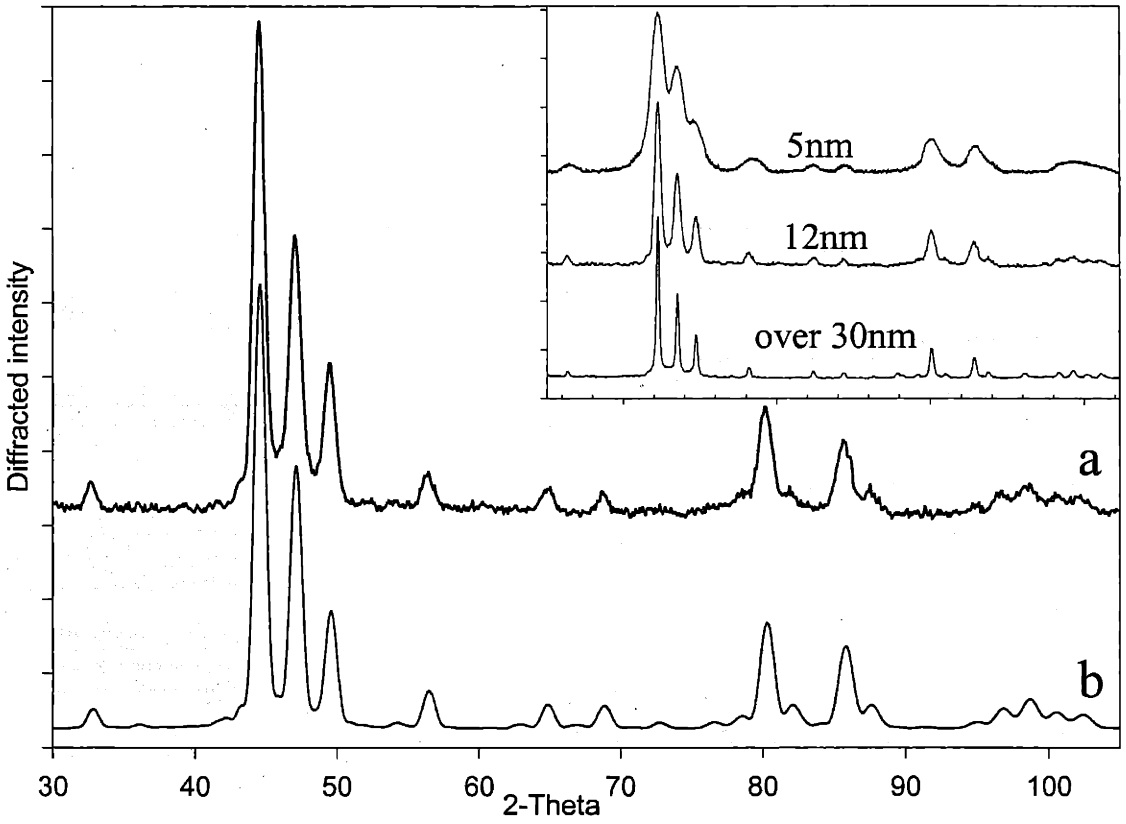

Figure 4.7 **a** - experimental x-ray powder diffraction of 12 nm cobalt nanocrystals prepared with the use of TOPO, **b** - simulated pattern for a mixture of 12 nm spherical particles containing pure ε-cobalt structure; the widths of the peaks in both patterns are virtually identical. The inset shows the size evolution of XRD patterns.

TOPO as a coordinating ligand is shown in Figure **4.7a**. This pattern corresponds to a pure ε-cobalt structure reported by us earlier[9] (also see Chapter 2) with excellent agreement in all the peak positions as well as their relative intensity. In order to probe the internal morphology of this particles and a possible presence of defects, which would contribute to the overall line shape, the structural simulations were also undertaken. The general approach to the calculations was essentially the same as described above for nanocrystals prepared with the use of TOP. The calculated diffraction pattern for a single 12 nm particle with ε-cobalt structure is shown in Figure **4.7b**. The striking agreement of the overall line shape with the experimental pattern made any further simulations unnecessary. It indicates that in the case of ε-cobalt the overwhelming majority of particles are truly single crystals, as was suggested by high-resolution TEM imaging. Furthermore, the width of each peak in this case can serve as a good measure of the overall nanocrystal size (see inset in Figure **4.7**).

4.4 References

1. *Handbook of detergents*, (Editor: U. Zoller), Marcel Dekker, Inc., New-York, **1999**, p. 53.
2. Wang Z. L., Dai Z., Sun S. *Adv. Mater.* **2000**, 12, 1944.
3. Sun S., Murray C. B. *J. Appl. Phys.* **1999**, 85, 4325.
4. Hall, B. D., Monot R. *Comput. Phys.* **1991**, 5, 414.
5. Bawendi M. G., Kortan A. R., Steigerwald M. L., Brus L. E. *J. Chem. Phys.* **1989**, 91, 7282.
6. Murray C. B., Norris D. J., Bawendi M. G. *J. Am. Chem. Soc.* **1993**, 115, 8706.
7. Murray C. B., Kagan C. R., Bawendi M. G. *Annu. Rev. Mater. Sci.* **2000**, 30, 545.
8. *Powder diffraction file PDF-2 databasesets 1-44,* **1994.**
9. Dinega D. P., Bawendi M. G. *Angew. Chem. Int. Ed.* **1999**, 38, 1788.

Chapter 5

Magnetic Properties of Individual Cobalt Nanocrystals

5.1 Introduction

Having succeeded in developing a novel preparation procedure that yields nearly monodisperse cobalt nanocrystals and establishing a good structural model for these colloids we can now address the second part of our original goal – looking at magnetic properties of individual nanocrystals. The size dependent properties can also be uncovered through the study of size series of these nanocrystals.

5.2 Experimental

Magnetic measurements were carried out using Quantum Design MPMS2 SQUID magnetometer operated in DC mode. The samples were prepared by dispersing concentrated hexane solution of nanocrystals in melted paraffin wax with subsequent evaporation of the solvent and cooling the mixture to form solid pellets. During the low temperature data collection the samples were warmed up to room temperature after each measurement in order to reset them to the same original state.

5.3 Results and Discussion

5.3.1 General

In order to study the magnetic properties of individual cobalt nanocrystals measurements were carried out on samples consisting of cobalt particles embedded in wax with the total volume of cobalt not exceeding 2%. This morphology ensures considerable separation between the neighboring particles and therefore minimizes their magnetic interaction and enables the interpretation of the results in the limit of non-interacting system. The weak diamagnetic response of the matrix was taken into account and corrected for by performing the same experiment on pure wax samples of equal volume.

5.3.2 Room Temperature Magnetization Measurements

In the size regime of up to 12 nm diameter the particles exhibit superparamagnetic behavior at room temperature, since no measurable hysteresis was observed upon sweeping the field in both directions up to 5 Tesla. This is because the magnetocrystalline anisotropy energy $E_M = KV$ (K – magneto- crystalline anisotropy constant, V – volume of the particle) is smaller than the thermal energy kT (T=300 K) in this size range (see Appendix A). The total magnetic moment inside the particle, therefore, is not fixed with respect to its crystal lattice and can be rotated by random thermal fluctuations. The magnetization behavior of such particles is generally described by the classical Langevin equation (see Appendix B), which describes magnetization of an ideal superparamagnetic particle:

$$M = \coth x - \frac{1}{x} \qquad \text{where} \qquad x = \frac{M_S \cdot V \cdot H}{k \cdot T}$$

(M_S – saturation magnetization of the material, V – particle volume, H – magnetic field, T-temperature, k – Boltzman constant). The size distributions of the samples were modeled by a Gaussian distribution function[1], leading to a final integral equation shown below:

$$M(H) = \int_0^{\infty} \frac{\left[\coth\left(\frac{M_S \cdot \pi \cdot D^3 \cdot x^3 \cdot H}{6 \cdot k \cdot T}\right) - \left(\frac{6 \cdot k \cdot T}{M_S \cdot \pi \cdot D^3 \cdot x^3 \cdot H}\right)\right] e^{\frac{-(D \cdot x - D)^2}{2 \cdot \Delta D^2}}}{\sigma \cdot \sqrt{2\pi}} dx$$

Fitting experimental magnetization curves with this function allows for determination of two fitting parameters – the average diameter (<D>) and the standard deviation ($\sigma = \Delta D/\langle D \rangle$). The results of this analysis can be summarized as follows.

1) The cobalt nanocrystals in the size range of 3-5 nm in diameter can be described precisely at room temperature (300 K) by the Langevin formalism. A typical example for the sample depicted in Figure **4.4** is shown in Figure **5.1a**. With the best-fit parameters (<D>=3.86 nm, σ =11%), the experimental and simulated curves are virtually indistinguishable. The overall shape of the simulated curve is very sensitive to small

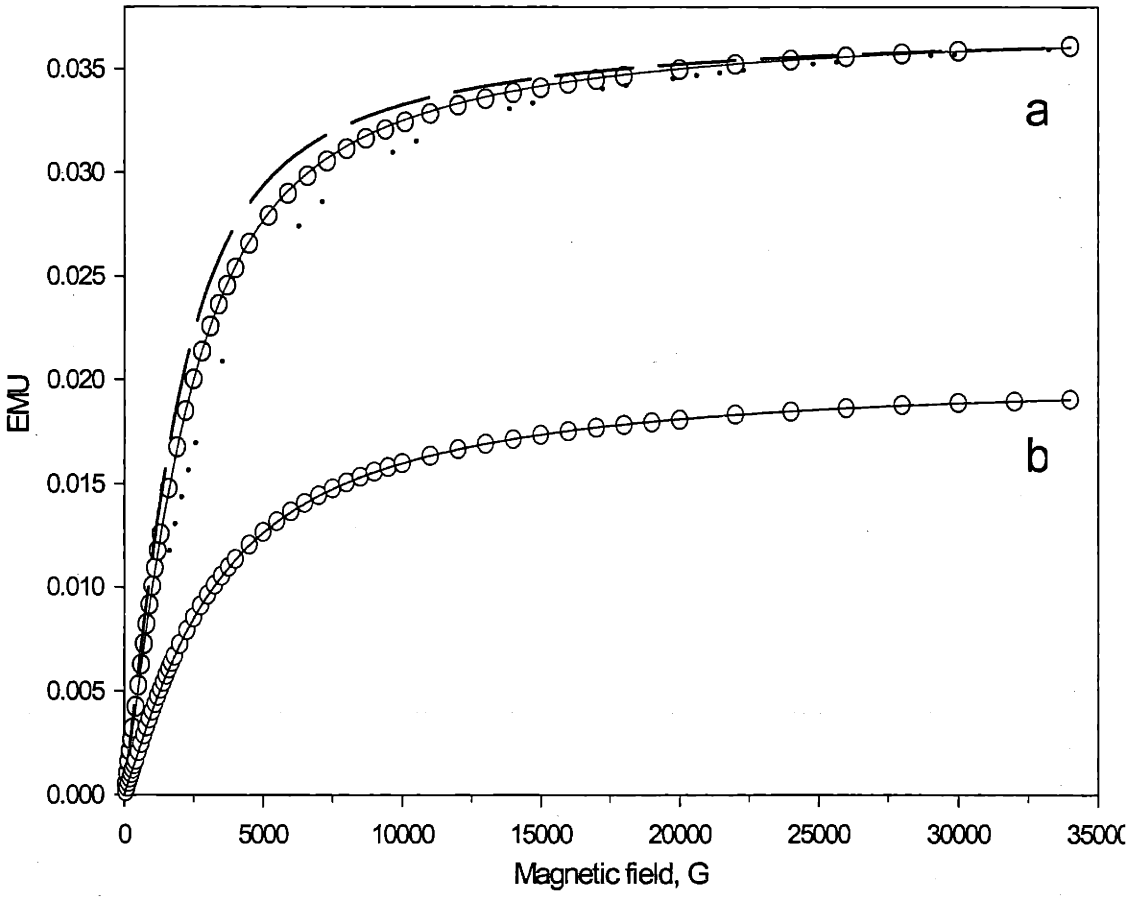

Figure 5.1 Room temperature (300 K) magnetization results (circles) and the corresponding Langevin fits (solid line) for the sample of 4.1 nm cobalt nanocrystals as depicted in Figure **4.4**; **a** - measurement taken the next day after preparation; **b** - the same sample as in **a** measured 20 days later. The best fit parameters <D> and σ are shown in Table **5.1**. The accuracy of the fit in **a** is demonstrated for the following parameters – 4.1 nm and 6% (dashed line), 3.5 nm and 11% (dotted line).

changes in the fitting parameters, making the determination of magnetic size and the size distribution accurate. As seen in Figure **5.1a**, simulated curves with slightly different values of <D> and σ deviate significantly from the experimental data. Furthermore, the accuracy of the magnetic size determination is supported by the comparison of the average volume change of the magnetic core and the change in the saturation intensity of magnetization upon oxidation of the nanocrystals. As shown in Table **5.1**, the ratios of these two parameters are virtually identical. This result is a strong indication that magnetically determined average size of the nanocrystals is, indeed, accurate and valid number and not an artifact of the fitting procedure.

Larger cobalt nanocrystals (6 nm and up) start to deviate from Langevin behavior even at room temperature. This is due to a gradual breakdown of the main approximation of the ideal superparamagnetic model ($E_M = KV << kT$) in this size regime, on which the Langevin formalism is based. Respoud, *et al.*[2] recently reported similar findings.

Table 5.1 Comparison of several parameters of samples described in the text

Parameter / Method	Average diameter <D>, nm	Standard deviation σ, %	Average volume $\langle V \rangle = \pi \langle D^3 \rangle / 6$ nm^3	Volume ratio	Saturation intensity, EMU	Saturation intensity ratio
TEM imaging	4.1	6	36.441			
Next day magnetization (Fig. **5.1a**)	3.86	11	31.207	1.840	0.03752	1.835
20 days later magnetization (Fig. **5.1b**)	3.08	19	16.955		0.02045	

(**2**) The average size of the nanocrystals determined from magnetization measurements is consistently smaller than the size obtained from TEM images for the same sample. The size distribution parameters determined magnetically, on the other hand, are consistently larger than those obtained from TEM. Chantrell, *et al.*[3] has observed similar results for a number of commercial ferrofluids. Chen, *et al.*[4], however, has found the magnetic size to be systematically larger than the corresponding TEM size based on determination of the magnetic moment per particle from susceptibility measurements. Such an anomaly, we believe, could be avoided by analyzing a complete magnetization curve rather than its initial part, which is equivalent to susceptibility measurements. Our results are summarized in Table **5.1**. These data indicate that even though the surface of each nanocrystal is protected by a close-packed shell of organic surfactant, the particles still inevitably oxidize upon exposure to air regardless of whether they are in solution or embedded in a solid matrix. Even freshly prepared samples processed in air show a 2.5 Å shell of oxide surrounding the metallic core of cobalt. Such a shell should account for 3-10% of total oxygen amount by weight per nanocrystal in the size range of 3-13 nm. This is in good agreement with the results of the elemental analysis, where about 9% of unaccounted atoms were attributed to oxygen for 10 nm particles.

The observed oxidation of the particle surface followed by further growth of the oxide shell differs significantly from the results reported by Puntes, *et al.* on cobalt nanocrystals prepared under very similar conditions.[5] In this report the authors "observed no evidence for the formation of cobalt oxides for months by x-ray diffraction, electron microscopy and other related spectroscopies (EDX, EELS)." Although we also do not observe the presence of oxide in our samples by XRD or TEM, the measurement of the total magnetization over time (as described above) provides, we believe, the most sensitive measure for the extent of oxidation.

Another important observation is the non-uniformity of the oxidation process. Fairly monodisperse nanocrystals (as observed by TEM) become increasingly non-uniform magnetically upon their exposure to air. Oxidation, therefore, can defeat the original goal of achieving a uniform magnetic response from a physically monodisperse sample.

5.3.3 Low Temperature Magnetization Measurements

Magnetization measurements at low temperature revealed the appearance of hysteresis below the blocking temperature T_B for a particular size sample as expected. The widths of the hysteresis loops were temperature dependent with minimal widths appearing just below the blocking temperature and gradually increasing upon cooling further down. The coercivity dependence on temperature was measured on five different size samples by recording the complete hysteresis loops at constant temperatures and then changing the temperature in a stepwise fashion. The average diameter of the nanocrystals in the samples as well as their size distribution were determined magnetically at high temperature as described in the previous section.

The coercivity data were analyzed using a Stoner-Wohlfarth model for coherent rotation during magnetization reversal (see Appendix C). Although this model describes the behavior of the collection of uniaxial particles (such as purely hexagonal cobalt nanocrystals with anisotropy constant K_{hcp}) it could be still valid in a more general case. The easy direction of magnetization in the fcc cobalt crystal is <111>, which is the same as the <002> easy direction in hcp crystal. The presence of multiple stacking faults along $<111>_{fcc}$-direction of our nanocrystals, therefore, breaks the symmetry of the cubic crystal and defines a unique preferred direction in the crystal. The value of the effective anisotropy K_{eff} in this case is expected to be different from K_{hcp} and lie somewhere between K_{hcp} and K_{fcc} of cobalt.

In order to include the variation of particle sizes in the samples into our model the average volume of nanocrystals and volume distributions were used. The final equation for temperature dependent coercivity was the following:

$$H_C(T) = \int_{\left(\frac{180kT}{\pi D^3 K}\right)^{\frac{1}{3}}}^{\infty} \frac{H_0}{\sigma\sqrt{2\pi}}\left(1-\sqrt{\frac{180kT}{\pi D^3 x^3 K}}\right)\cdot e^{\frac{-(D\cdot x-D)^2}{2\cdot\Delta D^2}}\,dx$$

The uniaxial anisotropy constants K_{eff} were determined by fitting the above equation to the experimental data while varying two parameters – H_0 and K, and calculating the values of K_{eff} from H_0: $K_{eff} = H_0 * M_S/0.96$

Figure **5.2** shows the results of the fitting for five samples of different size prepared under the same procedure. The deviation of experimental data from linear behavior as temperature approaches the blocking temperature T_B is due to the variation of particle size in the samples. (For single size particles the linear behavior would be observed until the intersection of the line with x-axis at temperature T_B). In this region the fits describe experimental data very well. At low temperature, however, the experimental points deviate systematically from linear behavior towards the higher coercivity. This deviation may likely be due to the limitations of our model which does not include the temperature dependence of the anisotropy constant K. The value of this constant generally increases with lowering the temperature. (*e.g.* for hcp cobalt the value of K_1 changes from 5×10^6 erg/cm^3 at 300 K to 8×10^6 erg/cm^3 at 0 K).

The size distribution parameters as well as the anisotropy value K_{eff} determined for each sample are listed in Table **5.2**. The values for anisotropy constant vary in the range of 4-10 $\times 10^6$ erg/cm^3 with no correlation between the size of nanocrystals and K_{eff}. Although some of these values are lower than the anisotropy constant K_1 of hcp cobalt at absolute zero (K_1=8 $\times 10^6$erg/cm^3) as expected, the two values appear to be higher. The value of 8.4 $\times 10^6$ can still possibly be explained by including a second order anisotropy constant K_2 that for hcp cobalt reaches 1 $\times 10^6$ erg/cm^3 at absolute zero.[6] The second value of 9.45 $\times 10^6$ erg/cm^3, however, cannot be reached even by including a higher order constants. The high values of the effective anisotropy constant indicate the presence of additional sources of anisotropy in the nanocrystals besides the magnetocrystalline anisotropy of pure cobalt. The shape anisotropy can be ruled out on the basis of TEM analysis where no elongation in the shape of the nanocrystals was found. The stress anisotropy also appears unlikely since no stress in the particles was observed. The most likely source of additional anisotropy is the exchange anisotropy due to the presence of oxide shell around each nanocrystal, as was evident from the previous section. It is well known that cobalt oxide (CoO) is antiferromagnetic below the Neel temperature of 289 K in the bulk.[7] An exchange anisotropy[8-9], which develops on the Co/CoO interface at lower temperatures significantly changes the properties of cobalt nanocrystals that one would expect without the presence of oxide. Therefore, such commonly measured quantities as the anisotropy constant and coercivity often provide misleading quantitative information

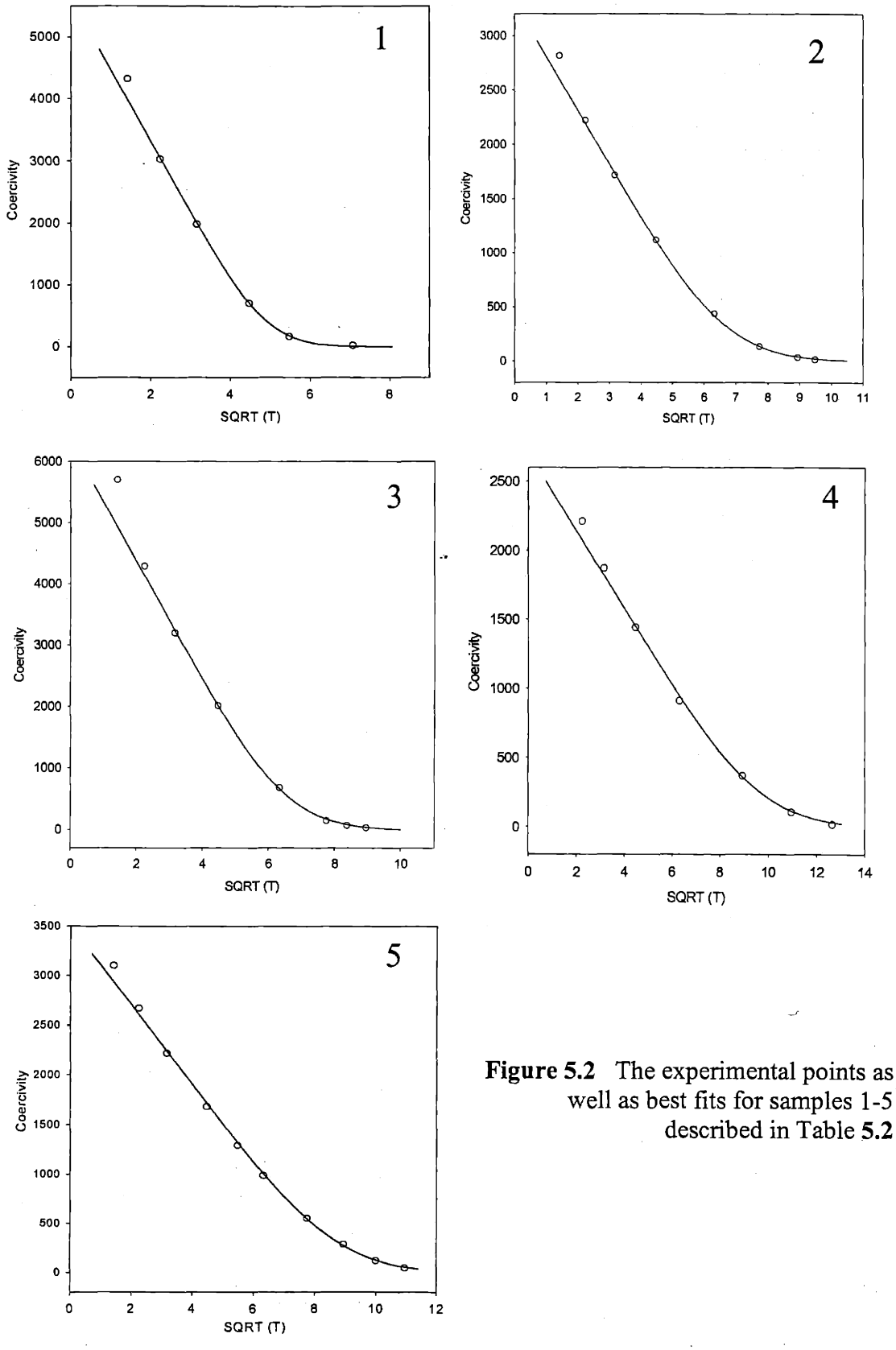

Figure 5.2 The experimental points as well as best fits for samples 1-5 described in Table **5.2**

Table 5.2 Several parameters calculated for the samples 1-5 shown in Figure **5.2**

Sample number	Average diameter <D>, nm	Standard deviation σ, %	K_{eff} at 0 K erg/cm^3	Average volume <V>, cm^3	Blocking temperature T_B, K	K calculated erg/cm^3
1	3.86	12	$8.4*10^6$	$30.11*10^{-21}$	44	$6.34*10^6$
2	4.8	14.5	$9.45*10^6$	$57.91*10^{-21}$	88	$6.29*10^6$
3	5.3	16	$4.95*10^6$	$77.95*10^{-21}$	110	$5.84*10^6$
4	6.9	15	$4.05*10^6$	$172.01*10^{-21}$	220	$5.30*10^6$
5	6.9	14	$5.25*10^6$			

about the intrinsic properties of cobalt nanocrystals without carefully assessing the extent of their oxidation and the effect of the oxide shell on the measured quantities. This, we believe, can also explain the large discrepancy (more than an order of magnitude) in the value of the magnetocrystalline anisotropy constant (K_M) for cobalt nanocrystals reported by various authors.[10, 11, 4,12] The hysteresis loop measurement for the field-cooled (FC) samples, used by many authors as a litmus test for the presence of cobalt oxide, also appeared to be unreliable. We found that a noticeable shift of the hysteresis loop from its zero field position (due to a unidirectional exchange anisotropy built up upon field-cooling) takes place only after a significant portion of the sample was oxidized. The smaller amounts of oxide, on the other hand, do not cause the FC hysteresis loop to shift from its central position, but still widen it compared to unoxidized sample due to the added exchange anisotropy. Therefore, the absence of the shift cannot serve as a reliable evidence for the oxide free sample. Meiklejohn[8] reported similar results for cobalt powders.

Since the widening of the hysteresis loop due to the presence of the oxide shell is still valid under normal zero field-cooled (ZFC) measurements, we found it equally

difficult to extract quantitative information about the intrinsic properties of cobalt based on coercivity measurements.

Although our original goal of studying the size-dependant properties of cobalt nanocrystals proved to be difficult to accomplish due to the oxidation problem, we hardly anticipated such a strong influence of a thin oxide shell on the overall magnetic behavior of cobalt nanocrystals. This study, therefore, led us to believe that a good deal of science could still be learned for such systems with ferromagnetic/antiferromagnetic coupling in the future.

5.3.4 Temperature dependence of magnetization

The temperature dependence of magnetization for field-cooled (FC) and zero field-cooled (ZFC) samples was typical for single domain particles following a gradual transition from a ferromagnetic to superparamagnetic regime. The experimental curves for sample 1 (also depicted in Figure **4.4**) with different applied fields are presented in Figure **5.3**. The FC curves show a gradual decay of magnetization upon warming up the sample with an inflection point at the blocking temperature T_B where the thermal energy just overcomes the anisotropy energy barrier. At this point, the magnetization starts to rotate freely inside the crystals, and the steepest decline is observed. For ZFC samples, on the other hand, the signal initially increases as the increasing thermal energy helps mobilize frozen spins and reaches its maximum at the blocking temperature T_B. After that point the signal drops similarly to the FC case. The increase in the strength of the applied field significantly widens the peak (as seen in Figure **5.3**) and causes it to shift slightly towards the higher temperatures. This could be explained by the fact that at higher fields the thermal energy needs to overcome not only the crystalline anisotropy (present in the absence of the field), but also the aligning force the applied field. This, obviously, requires a higher temperature.

The temperature dependence of magnetization for ZFC samples 1-4 under the applied field of 100 Gauss is shown in Figure **5.4**. As expected, the blocking temperature T_B shows clear size dependence. This is well understood since the magnetocrystalline anisotropy energy is proportional to the volume of the nanocrystals – $E_M = KV$. The values of the anisotropy constant K calculated from the blocking temperature T_B are

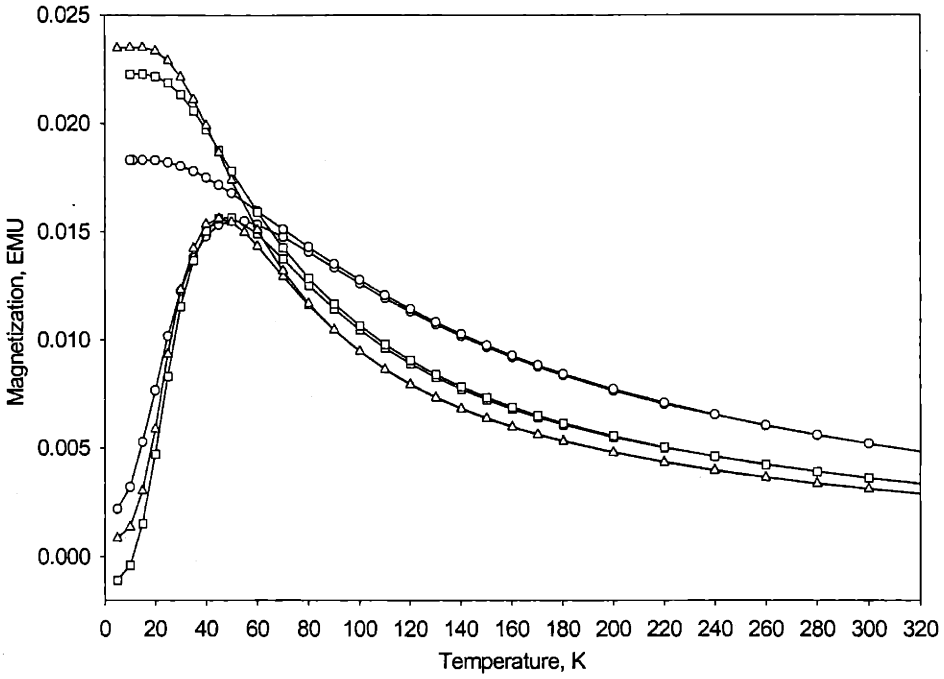

Figure 5.3 Temperature dependence of magnetization (FC and ZFC) for sample 1 at three different applied fields: 50 Gauss (triangles), 100 Gauss (squares), and 500 Gauss (circles).

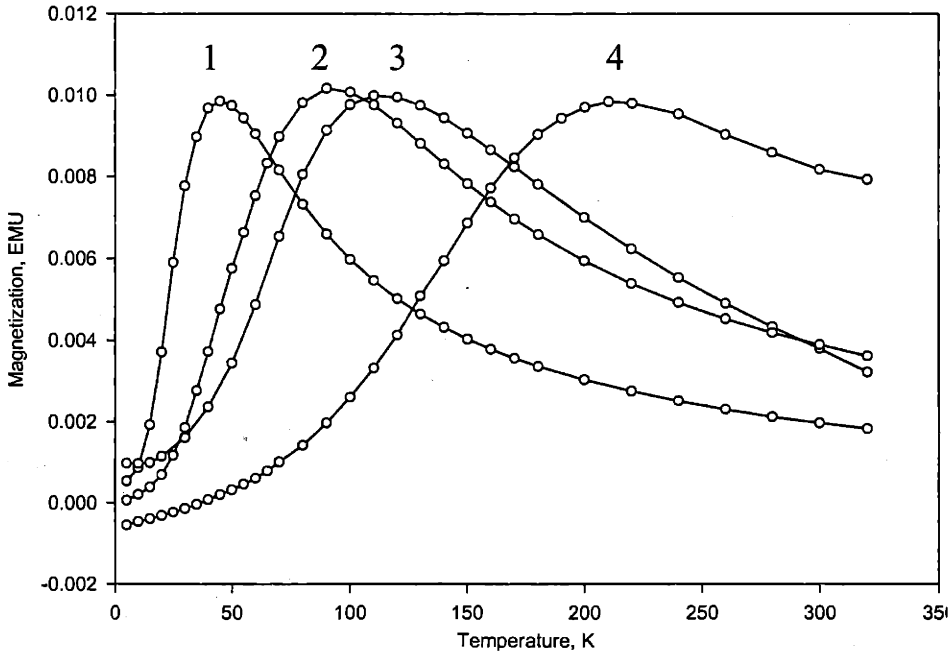

Figure 5.4 Temperature dependence of magnetization for ZFC samples 1-4 with parameter listed in Table **5.2**; applied field 100 Gauss.

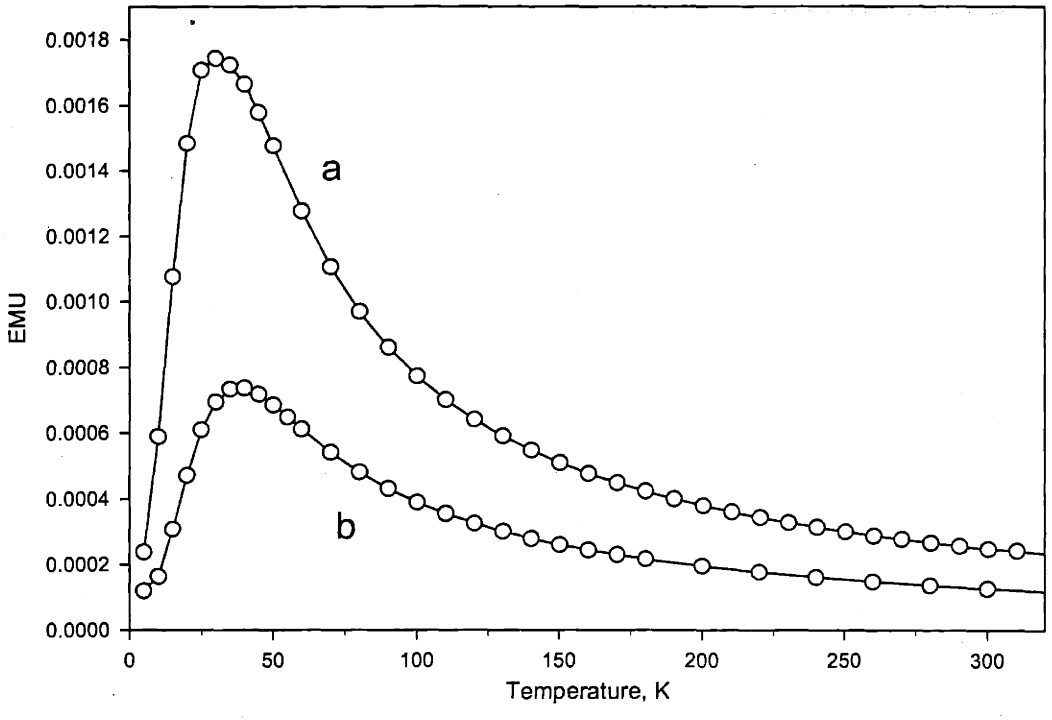

Figure 5.5 Temperature dependence of magnetization for the two zero field-cooled samples shown in Figure **5.1** and Table **5.1**. The applied field is 50 Gauss. The observed broadening of the peak in **b** is due to the increased size distribution of the sample upon oxidation.

shown in the last column of Table **5.2**. Although the range of these values (5.3-6.4 x 10^6 erg/cm^3) is in a good agreement with K_1 anisotropy constant of hcp cobalt, each value may not be very accurate because of the rather arbitrary mathematical definition of the blocking temperature itself. A clear size dependence observed in the calculated values of K can also be explained. Since each calculation is performed at a particular temperature (at blocking temperature T_B that is), the gradual decrease in K with increasing temperature may be the manifestation of temperature dependence of the anisotropy constant. For hcp cobalt, the value of K_1 constant changes from about 7.5 x 10^6 erg/cm^3 at 50 K to 6 x 10^6 erg/cm^3 at 200 K.[6] Alternatively, such a trend can also be explained by the presence of an oxide shell. Since smaller nanocrystals are more sensitive to surface effects, the oxide shell of the same thickness should have a stronger effect on smaller particles. This argument is supported by the data in Figure **5.5** that shows the magnetization vs. temperature dependence of zero field cooled (ZFC) samples described above (Figure **5.1** and Table **5.1**). The blocking temperatures defined at the maximum of each curve remain virtually unaffected for the two samples, even though the average volume of particles in sample **b** is almost half of that in sample **a**. Since the size effect and the oxide effect would shift the blocking temperature in opposite directions, we argue that in this case the exchange anisotropy due to the oxide shell provides a comparable contribution to the overall magnetic anisotropy compared to the crystalline anisotropy of the magnetic core. Therefore, we found it difficult to extract information on the intrinsic properties of cobalt with any significant confidence from these data.

5.3.5 Oxidation studies

In order to access the influence of surface oxidation on the magnetic properties of cobalt nanocrystals the following study was undertaken. After preparing sample 5 using a standard procedure and dispersing it in a paraffin wax, the sample was divided into two parts. The first part was then studied as prepared along with four other samples (see part 5.3.3). The second part was exposed to a bubbling forming gas (5% hydrogen, 95% nitrogen) at 200 C for 8 hours under inert atmosphere. Under these conditions any cobalt oxide layer covering the surface of the nanocrystals should be reduced to metal, eliminating the exchange anisotropy as an additional source of anisotropy in the crystals.

Upon cooling down, the sample was transferred into the glove box, prepared as the rest of the samples, and loaded into a nitrogen filled test tube. The only time the sample was exposed to air was during its loading into magnetometer. Since this exposure lasted only several seconds it was assumed to cause no effect on the subsequent magnetic measurements.

During the reduction process one problem become apparent. Heating the paraffin solution of the particles to 200 C for an extended time with continuous bubbling of the gas lead to the partial removal of the capping groups from the surface of the nanocrystals. As a result, significant aggregation of particles occurred. This development was certain to cause some problems with subsequent magnetic measurements. For example, magnetic size determination of the reduced sample was impossible because of the strong magnetic interactions in the resulting aggregate. The coercivity change between the original and reduced samples also could not be quantitatively compared for the same reason. Nevertheless, some observations were still useful.

The temperature dependent coercivity for samples **a** (before reduction), **b** (immediately after reduction), and **c** (three days after reduction) is shown in Figure **5.6**. Although the coercivity of the reduced sample drops significantly, the samples **a** and **b** cannot be compared because of the aggregation problem in sample **b**. However, the samples in **b** and **c** are structurally the same and can be compared directly. This clearly shows how three-day air exposure leads to a dramatic increase in coercivity due to the added effect of exchange anisotropy. Moreover, a weeklong air exposure of the same sample causes the oxide layer to totally dominate over the crystalline anisotropy. This is demonstrated in Figure **5.7**. The ZFC curve appears similar to those described in section 5.3.4 but with a flat tail and a very sharp peak. The FC plot, though, also appears flat at low temperatures with a small bump corresponding to a sharp rise of the ZFC curve. We argue that, in this case, the transition is determined not by the blocking temperature of the magnetic core (as described in section 5.3.4), but rather the Neel temperature of the oxide layer. The bump on the FC curve is therefore due to the contribution of additional spins freed up by Neel transition. Since the Neel temperature for the bulk cobalt oxide (CoO) is 289 K, it should definitely be lower for the nanometer range crystals. All of these arguments are supported by our data.

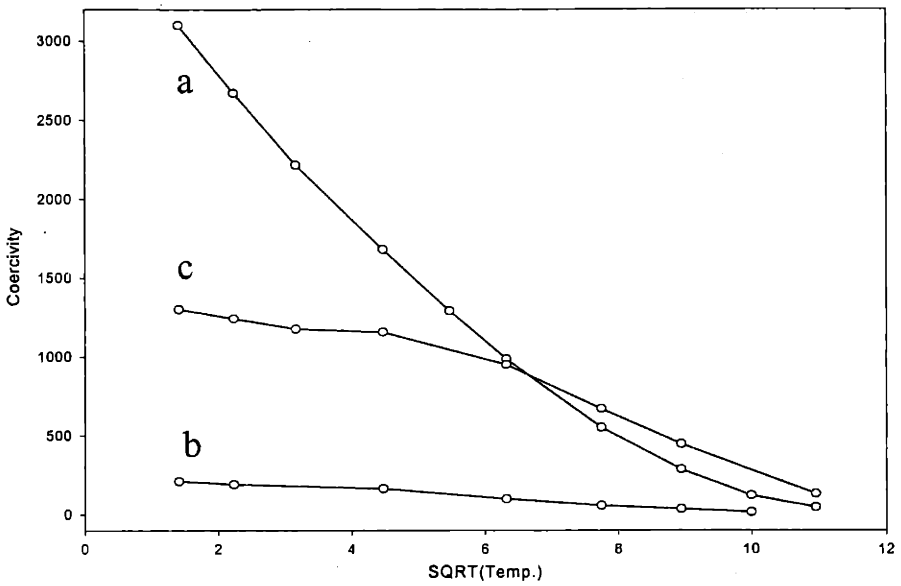

Figure 5.6 Temperature dependence of coercivity for sample 5: **a**- before the reduction, **b**-immediately after the reduction, **c**-three days after the reduction.

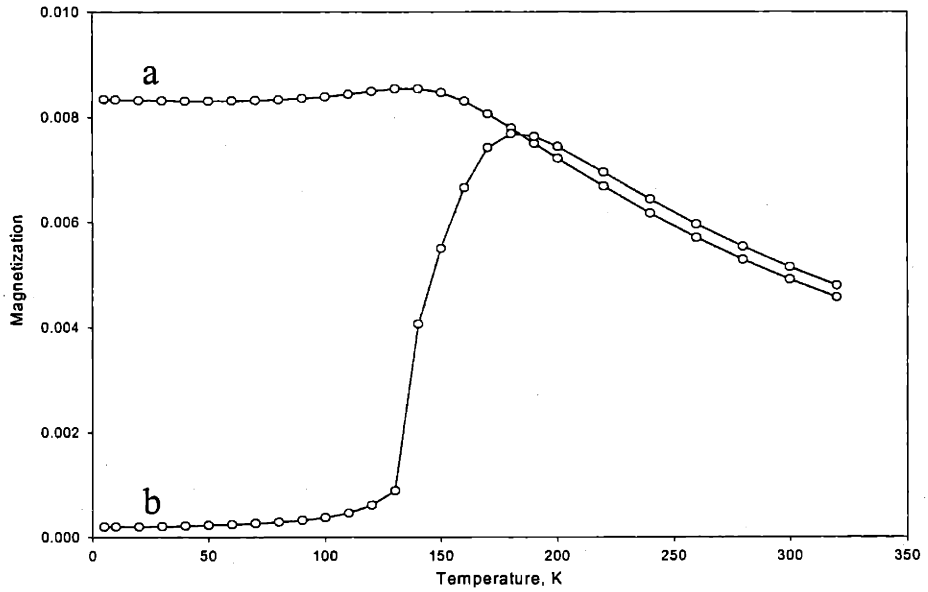

Figure 5.7 Temperature dependence of magnetization for sample 5 after it was reduced and exposed to air for one week: **a** – field-cooled; **b** – zero field-cooled. The applied field was 100 Gauss.

5.4 References

1. Although several authors described the size distribution of nanoparticles in colloidal systems by a lognormal distribution function we found that for relatively narrow distributions (5-20%) the difference between the two was minimal.
2. Respaud M. *J. Appl. Phys.* **1999**, 86, 556.
3. Chantrell R. W., Popplewell J., Charles S. W. *IEEE Trans. Magn.* **1978**, 14, 975.
4. Chen J. P., Sorensen C. M., Klabunde K. J., Hadjipanayis G. C. *Phys. Rev. B* **1995**, 51, 11527.
5. Puntes V. F., Krishnan K. M., Alivisatos P. *Appl. Phys. Lett.* **2001**, 78, 2187.
6. *Landolt-Börnstein numerical data and functional relationships in science and technology, Vol.19/a* (Editor: H. P. J. Wijn), Springer, Berlin, **1986**, p. 44.
7. *Landolt-Börnstein numerical data and functional relationships in science and technology, Vol.27/g* (Editor: H. P. J. Wijn), Springer, Berlin, **1992**, p. 8.
8. Meiklejohn W. H., Bean C. P. *Phys. Rev.* **1957**, 105, 904.
9. Meiklejohn W. H. *J. Appl. Phys.* **1962**, 33, 1328.
10. Osuna J., de Caro D., Amiens C., Chaudret B., Snoeck E., Respaund M., Broto J.-M., Fert A. *J. Phys. Chem.* **1996**, 100, 14571.
11. Becker J. A., Schäfer R., Festag R., Ruland W., Wendorff J.H., Pebler J., Quaiser S. A., Helbig W., Reetz M. T. *J. Chem. Phys.* **1995**, 103, 2520.
12. Petit C., Taleb A., Pileni M. P. *J. Phys. Chem. B* **1999**, 103, 1805.

Chapter 6

Shape Variation of Cobalt Nanocrystals: From Triangles to Rods to Wires

6.1 Introduction

Succeeding in the preparation of nearly monodisperse spherical nanocrystals and looking at their size-dependent properties addresses only one part of the story - namely, the size evolution of the system with a single type of magnetic anisotropy. Indeed, in an ideal spherical nanocrystal of a pure magnetic material, such as cobalt, the magnetocrystalline anisotropy is the only source of anisotropy. A more general approach, however, should include consideration of additional sources of anisotropy, such as shape anisotropy. This type of anisotropy is present in crystals with a shape other than spherical. Depending on the form of such crystals, the shape anisotropy can be as high as intrinsic crystalline anisotropy, leading to a combined effect of a "mixed" anisotropy or, in some cases, totally dominate the properties. In certain cases, the shape anisotropy can greatly exceed the crystalline anisotropy. This phenomenon was successfully utilized in some technological applications of crystals in a micron-range regime such as storage media. The study of these effects on a much smaller size scale is therefore not only of great interest to basic science but can also lead to the development of new materials and technological applications.

Undoubtedly, the desire to study these phenomena on a much smaller (nano-size) scale runs into the problem of preparing such materials. Similarly to the spherical particles, the "shaped" nanocrystals should be fairly uniform in the size and shape in order to uncover any useful size/shape-dependent information. In this chapter, we attempt the first steps toward this goal following a simple modification to the procedure described earlier (Chapter 2) for the preparation of spherical nanocrystals.

6.2 Background

The interest in preparing nanocrystals with a distinct shape other than spherical has increased dramatically in the last few years. When this work was started back in

1995, there were only a handful of successful preparations reported in the literature. Now, such examples are numerous. The reason for intensified research is this area was the realization that in the very small size regime the properties of crystals become not only size- but also shape-dependent. This is also something that is not observed in the bulk state. In the "nano" size regime, however, the changes in crystal shape result in modification of not only magnetic, as described above, but also electronic, optical, and catalytic properties. Semiconductor quantum rods, for example, have two different levels of electronic confinement along their long and short axes, leading to a significant change in their electronic structure.[1] On the other hand, the carriers in longer wires are confined to the directions perpendicular to the wire axis, and confinement along the axis is not observed. Similarly, the gold nanorods exhibit two plasmon frequencies along two axes and, therefore, two absorption peaks in the visible unlike a single peak for spherical particles.[2] Catalytic activity of the small particles was also reported to depend on a particle size and shape since certain facets of a crystal associated with a particular shape are more catalytically active than others.[3]

Various methods for preparing "shaped" nanocrystals have been reported. The most successful among physical methods was the so called vapor-liquid-solid growth of nanowires. This method employs metal nanocrystals as nucleation centers for other inorganic materials, the vapors of which are absorbed by the liquid phase of the metal at high temperatures. The pure inorganic material gradually recrystallizes on one side of a supersaturated liquid solution droplet, leading to the formation of a long wire. Many single element as well as compound semiconductors have been prepared by this method - Ge, Si,[4] and CaAs[5] among others.

Another approach to shape control is the synthesis of nanocrystals in restricted environments. This can be achieved in both gas and liquid phases. Carbon nanotubes were successfully used as templates for the preparation of carbide[6-8] and nitride[9] nanowires. Nanometer-sized pores in membranes[10] and zeolites have also been used. Although template-based techniques are easy to implement, they have important limitations. For example, growth in porous membranes typically produces polycrystalline materials. Further processability of prepared nanoparticles is also hard to achieve.

The other major approach to preparing "shaped" nanocrystals is a more traditional growth from solutions, with tailoring the composition of a solution and other factors, such as temperature, to favor one particular morphology. There are two competing theories on how this can be accomplished. One theory points to the fact that the crystal growth takes place not in a homogeneous solution but in a complex system where different components of the solution organize themselves into micelles, or reverse micelles, serving as immediate "nanoreactors." The shape of the resulting crystals, therefore, depends on the shape of these micelles and can be changed from spheres to cylinders to long channels by solvent composition. This is called "soft templating." This method was used to prepare nanorods and nanowires of copper[11-13], gold[2], CdS and CdSe[14], $BaCrO_4$[15], $BaCO_3$[15], and $CaSO_4$[17] among others. Although several authors have demonstrated a good correlation between the microscopic structure of solution and the resulting shape of grown nanocrystals, no direct evidence of templating have been provided. Recently, even the strongest supporters of this theory have raised questions about its validity. Pileni, *et al.*[18] has shown that the shape of copper nanocrystals grown in reverse micelles was greatly affected by addition of small amounts of salts (NaCl, $NaHSO_3$) to the colloidal solution, even though the concentrations of all other components were kept constant. These small amounts of salts did not alter the microscopic structure of the growth media, but the shape of the crystals was strongly affected.

The other competing theory of shape control in solution is based on the notion that the different faces of the crystal can grow at different rates. One of the first experimental results explained on the basis of the Kossel-Stranski theory of face-selective growth was the preparation of gold particles with platelike shapes by the slow reduction of gold chloride in solution.[19] The difference in the growth rates can be further enhanced by addition of surfactants, which can selectively bind to the particular facets of the growing crystals and lead to formation of crystals with a specific shape. During such growth, the main factors determining the final crystal shape would be the selectivity and concentration of the surfactants present in the solution as well as the overall kinetics of the growth. By the reduction of copper acetate in the presence of poly(vinyl-2-pyrrolidone) as a surfactant, thin platelike particles with hexagonal outlines were

produced.[20] El-Sayed, *et al.*[21] reported the preparation of platinum nanocrystals by reduction of K_2PtCl_4 with hydrogen gas in water and in the presence of sodium polyacrylate as a capping molecule. Particles with predominantly cubic or triangular morphology were formed by simply changing the concentration of the polymer. The recent report by Reetz, *et al.* points to the selectivity of α-hydroxy carboxylates in the growth of triangular-shaped nickel and palladium nanocrystals.[22] Similar carboxylates without α-hydroxy functionality led, in this case, to the formation of regular spherical particles. The most significant understanding of shape control to date was achieved by Alivisatos and coworkers in the preparation of CdSe nanocrystals.[23-24] Through selection of appropriate surfactants and careful adjustment of concentrations during the growth process, they were able not only to "tune" the transition from spheres to short to long rods but also produce more exotic crystalline shapes, such as arrows, teardrops, and tetrapods.

Although accepted conventional wisdom has always been growth by a gradual addition of atoms or ions to the surface of the crystal, a number of recent reports challenge this perception. Banfield, *et al.*[25] discovered the growth by "oriented attachment" in which a number of 2-3nm in diameter crystallites can come together to form a bigger crystal. In this mechanism, the nanocrystals orient each other into a perfect 3D alignment before fusing together to form a bigger crystal. The interesting fact is that this process occurs naturally and has been observed in certain geological samples. However, it may also occur under laboratory conditions. Furthermore, this mechanism was predicted to be useful for creating advanced artificial materials.[26] For example, Hyeon, *et al.*[27] reported the preparation of the crystalline iron nanorods from spherical iron nanocrystals in which "oriented attachment" could be one possible explanation of the observed phenomenon.

6.3 Experimental

6.3.1. General

The synthesis of all samples was carried out under a dry nitrogen atmosphere. All chemicals were used as purchased: dicobaltoctacarbonyl (DCOC, 95%) from "Strem";

tributylphosphine (TBP, 97%) from "Aldrich"; dioctyl ether (DOE, 97%), sodium carboxylates (stearate – 98%, caprate – 98%) from "Fluka". Separation of the product from the reaction mixture and the following size-selective precipitation were conducted under ambient conditions using Omnisolv^{Tm} grade solvents purchased from "EM Science".

6.3.2. Preparation procedure

The typical preparation procedure was as follows: 0.15g of sodium stearate is placed into a 100 mL round bottom flask and 18 mL of DOE were added. This mixture is allowed to dry under vacuum at 55°C for two hours. Meanwhile, 0.55g of DCOC is placed into 20 mL vial inside a glove box and 17 mL of dioctyl ether are added. This mixture is allowed to stir vigorously until all of the DCOC is completely dissolved (typically 1 hour). 2 mL of TBP is slowly added to the vial. The evolution of carbon monoxide is immediately observed and the color of the solution changes from dark brown to yellow. After this reaction is complete (10-15min), the yellow compound is loaded into a 20 mL syringe for injection. After drying under vacuum the flask is filled with nitrogen, the temperature is raised to 230°C, and the mixture is allowed to stir rapidly to ensure complete dissolution of the stearate. The content of the syringe is then injected into the flask under vigorous stirring. After the initial drop the temperature is slowly raised to 200°C, and the mixture is allowed to stir until the completion of the reaction – change of the color from dark brown to black (typically 1 hour). The heat is then removed and the flask is allowed to cool to room temperature.

This procedure can be modified in two different ways – in order to increase the length of the nanorods produced and to increase the yield of the triangular-shaped nanocrystals. The first goal is achieved by introduction of 0.1g of sodium caprate into the flask in addition to stearate. In the second case, the composition of the chemicals is the same, but the content of the syringe is slowly introduced into the flask at 160°C, instead of 230°C, at which temperature decomposition of precursors does not take place.

6.3.3 Separation of the product

The contents of the flask are transferred into a centrifuge tube (if there is any aggregation of the product on the stirbar, it can be washed off with hexane) and an appropriate amount of ethanol is added to the tube to cause precipitation of the product (original solution turns cloudy). The product is then separated by centrifugation. The liquid portions of the tubes are discarded, and the product is redispersed by an addition of hexane. Subsequent addition of ethanol leads to precipitation of the product again. This procedure is typically repeated several times to remove excessive surfactant and other impurities from the product. The size selective precipitation can then be carried out similar to the one used for separation of spherical particles on page 37.

6.3.4 Orientation by magnetic field study

The orientation of cobalt nanorods by an applied magnetic field was studied by casting a drop of the solution containing nanorods onto a TEM grid placed between the poles of an electromagnet. A higher boiling solvent was used (nonane instead of hexane) in order to allow sufficient time for the magnetic field to interact with the nanorods in the liquid phase before the solvent evaporates (typically 5min). The uniform magnetic field with a tunable range of 0-1 Tesla was created by an electromagnet of an EPR spectrometer ("Bruker", Type B-E30 magnet).

6.3.5 Transmission electron microscopy and diffraction

Low-resolution TEM studies were conducted in a bright field mode using a JEOL 2000FX microscope. The smallest objective aperture was used for imaging individual particles to produce high Z-contrast pictures. Dark field imaging was used to evaluate the crystallinity of individual nanorods. The electron diffraction images of oriented nanorods were obtained at a 130 cm camera length by selecting the desired area of the sample with the appropriate size diffraction aperture. High-resolution imaging and single crystal diffraction were performed with a JEOL 2010 microscope. A number of different size apertures were selected to permit the imaging of desirable lattice projections. The diffraction images of individual nanocrystals were collected in a "nanodiffraction" regime by focusing the beam on a particular nanocrystal and recording the pattern at a 25

cm camera length. Both instruments were operated at 200 kV and had LaB_6-based filaments. Copper grids (400 mesh) coated with a thin layer of amorphous carbon (3-4nm) were purchased from Ted Pella, Inc. The samples were prepared by dropcasting from dilute hexane solutions.

6.4 Results and Discussion

6.4.1 Shape control

As indicated in the experimental section above, the main modification of the preparation procedure leading to the formation of "shaped" nanocrystals, as opposed to the spherical ones described in Chapter 3, was the introduction of ionic surfactants (sodium carboxylates) into the flask before the nucleation stage of the crystal growth. It appears, therefore, that these surfactants play a major role in controlling the shape of the resulting nanocrystals. In fact, introducing the ionic surfactant after the nucleation stage is completed, while keeping the concentrations of all the other ingredients constant, led to the formation of only spherical particles. Carrying out the nucleation stage in the presence of carboxylates, however, leads to the formation of a significant number of the triangular and rod-shaped nanocrystals. This observation is similar to the one reported by Reetz.[22]

The other major factor affecting the shape of the resulting nanocrystals was the way of introducing the precursors into the reaction vessel. In one case, the precursors are quickly injected into a hot solution, similar to the preparation of spherical particles described in Chapter 3, leading to the immediate decomposition of a fraction of the precursors and the formation of tiny nuclei. These nuclei then grow further by heating the reaction vessel and decomposing the remaining portion of the precursors. In the second case, the precursors are introduced into a reaction vessel at a lower temperature, prompting no initial decomposition, and are allowed to mix thoroughly with all of the other reagents. A very slow decomposition then follows upon gradually raising the temperature of the reaction mixture.

A TEM image of the reaction product prepared by a fast injection of the precursor into the hot solvent (230°C) containing sodium carboxylates (stearate and caprate) is

shown in Figure **6.1a**. Along with the spherical particles (~60%) this sample consists of a significant number of cobalt nanorods (~40%). Only a few triangular and other shape crystallites are found (~2-3%). The length of the nanorods is fairly uniform and falls in the range of 70-100nm. For comparison, Figure **6.1b** shows a TEM image of the reaction product prepared with the same composition of reagents but with addition of the precursors at a lower temperature (160°C), where no initial decomposition took place. Along with the regular spherical particles (~60%), however, this product contains a large number of triangular crystals (~30%). Only a small number of rods (~10%) are observed.

The two examples above are quite typical in terms of the reaction product compositions. First, they clearly demonstrate the formation of two distinct shapes of the nanocrystals upon introducing sodium carboxylates as surfactants into the growth process. Second, they show the presence of a significant number of spherical particles along with the "shaped" ones. Although effort was made to increase the yield of the nanorods by changing the various preparation conditions (such as concentrations of the precursors and surfactants, injection temperature, and a temperature ramp), the relative amount of the rods could reach only ~40% of the total in the best samples. In average samples, however, this amount is even lower (~15-20%).

Since the introduction of carboxylates leads to the formation of nanorods or triangles, it seems logical that the relative concentration of the surfactants should be further increased in order to increase the yield of these particles relative to the regular spherical ones, obtained without the presence of carboxylates. However, this is hard to achieve with the current preparation procedure. The problem is that the crystal growth takes place in an essentially nonpolar environment. This is important for several reasons. The cobalt precursors, dicobalt octacarbonyl or its complex with tributylphosphine, are nonpolar compounds and therefore soluble in nonpolar solvents (dioctyl ether in our case). Furthermore, the synthesized nanocrystals themselves are soluble in only nonpolar solvents. This property keeps them in the solution during the growth and prevents them from aggregating. The sodium carboxylates, however, are ionic compounds, which are much more soluble in polar rather than nonpolar solvents. In the current preparation procedure, the concentration of sodium stearate used as a surfactant almost reaches the solubility limit in dioctyl ether and can be increased only by a factor of two. Such an

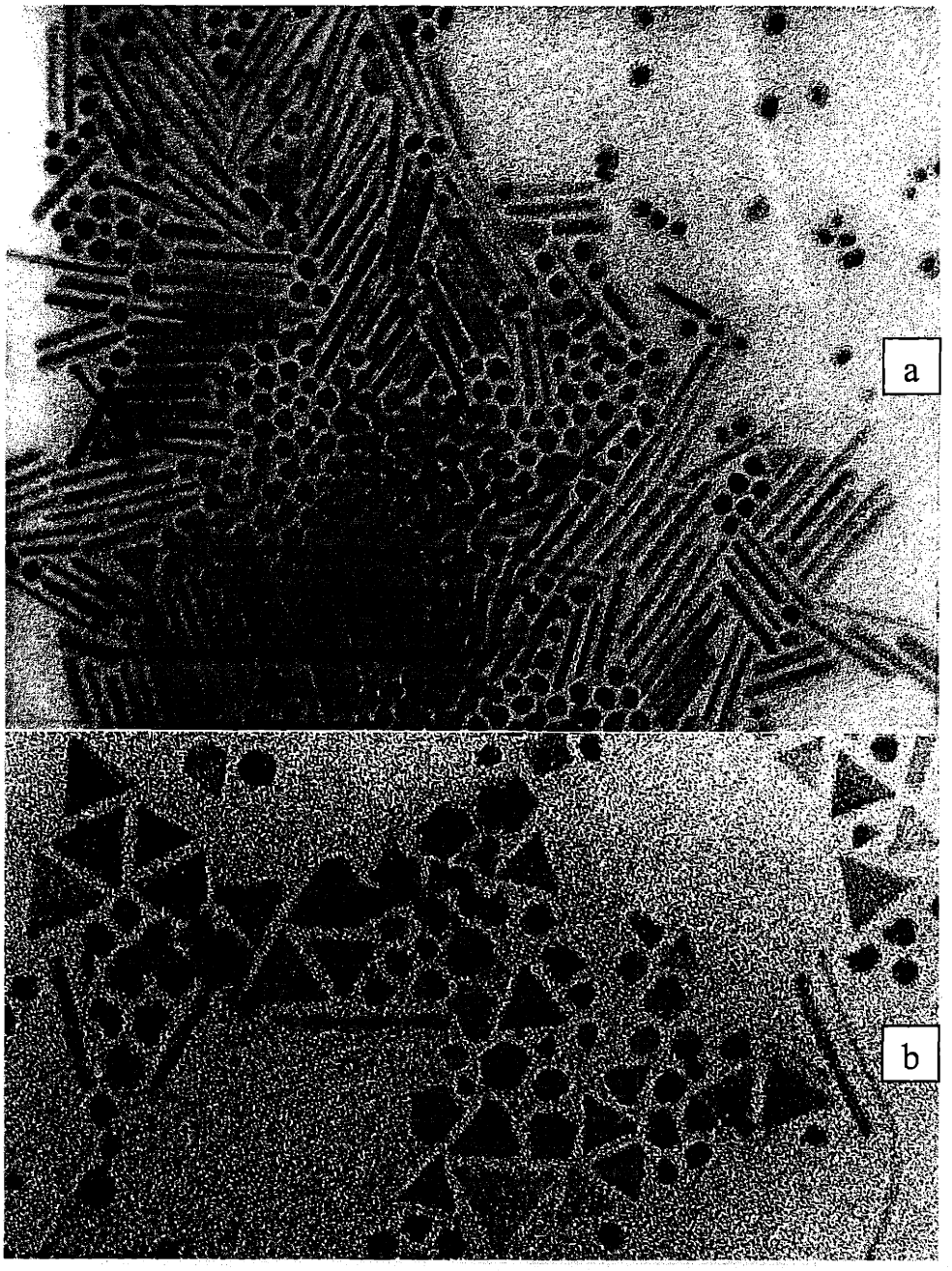

Figure 6.1. TEM images of the reaction product prepared with the same concentrations of the reagents by: **a** - fast injection of precursors into a hot solvent; **b**- slowly heating solution containing precursors.

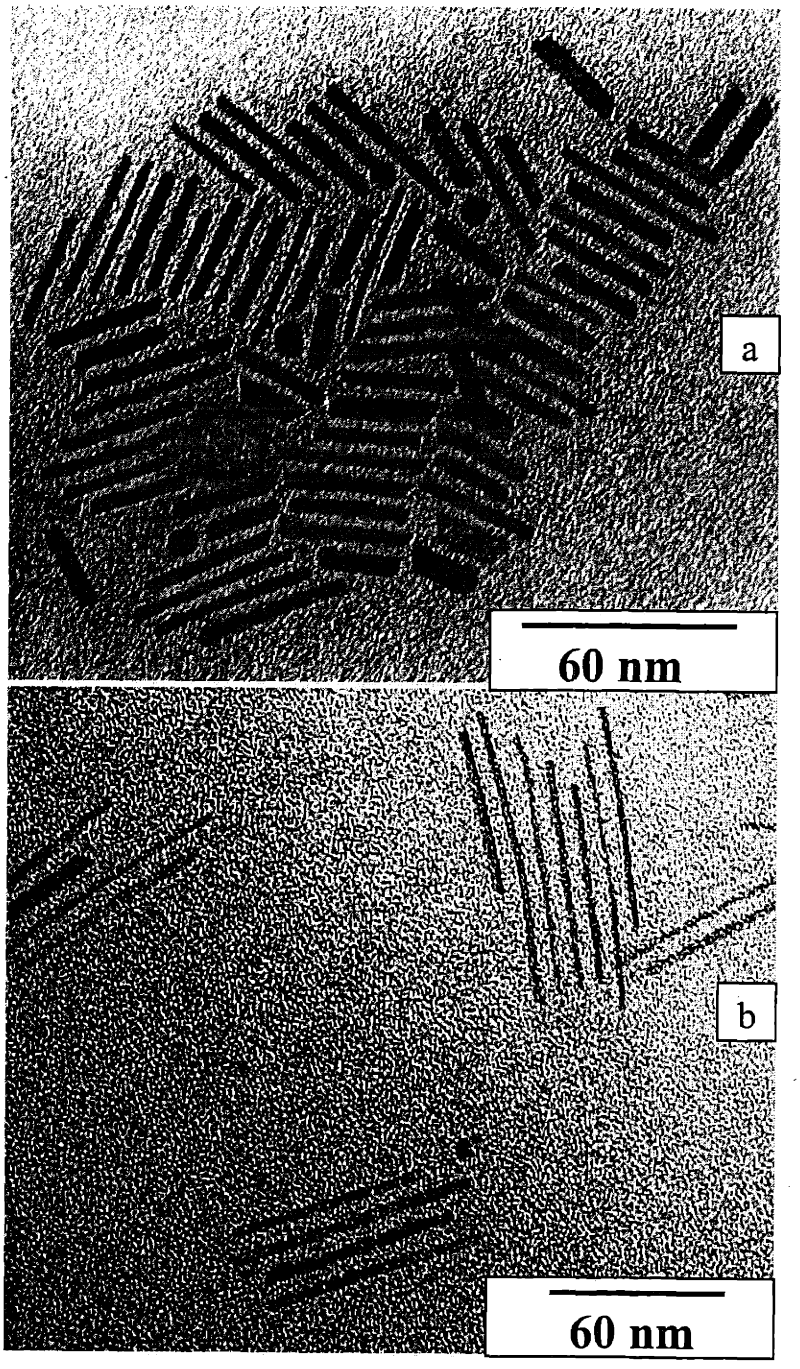

Figure 6.2. TEM images of cobalt nanorods prepared with different concentrations of ionic surfactants: **a**- 0.12g of sodium stearate; **b**- 0.12g of sodium stearate and 0.1g of sodium caprate.

increase, however, does not significantly affect the yield of the nanorods.

Another interesting observation is related to the length of the nanorods produced. It appears that although the increase in carboxylates concentration did not increase the relative amount of the rods, it certainly affected their length. Figure **6.2a** shows an image of nanorods produced by introduction of 0.12g of sodium stearate into the growth solution. In this case, the rods are rather short and thick (length ~ 40-60 nm, width ~5-7 nm). In comparison, the rods produced with 0.12g of stearate and 0.1g of caprate are shown in Figure **6.2b**. They are thinner (3-5nm in width) and longer (80-100nm in length). Further increase in the amount of sodium caprate can result in the production of even longer rods, which would be more appropriatly called nanowires. An image of one such wire is shown in Figure **6.3**. Having the width of only 4 nm this wire reaches the length of 500 nm. These nanowires appear to be flexible since most of them bend when deposited on the substrate.

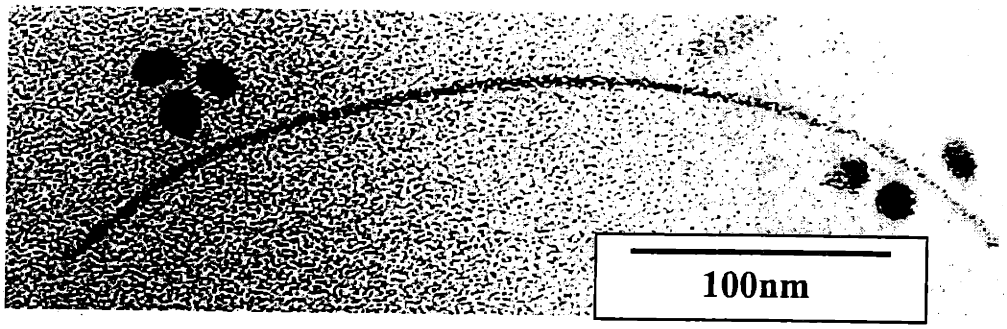

Figure 6.3. One of the longest cobalt nanowires observed in the reaction products.

6.4.2 Orientation by magnetic field

Since all the samples of cobalt nanorods also contained a large number of regular spherical particles, it was impossible to study their magnetic properties by a conventional method such as SQUID magnetometry. However, some insights into the magnetic behavior of the nanorods could be obtained by a direct observation of samples exposed to the magnetic field. This was accomplished by dropcasting a dilute solution of particles

containing nanorods onto a TEM grid and applying a homogeneous magnetic field during the drying process. The results of these studies are shown in Figure **6.4**. Before application of the field the nanorods are randomly oriented on the surface of the grid. After the external field is applied, the nanorods rotate in the solution until their long axes align with the field. The strength of the applied field was varied (in fact, gradually reduced) in order to estimate the minimal field needed to orient the rods in solution. At 100 Gauss, the effect of alignment was still noticeable. A simple estimate for the field strength needed to orient nanorods in solution can be calculated from the equation kT = MH, where kT is the disorienting thermal energy of a solution and MH is the orienting energy of a magnetic interaction. For a typical cobalt nanorod of 50 nm x 6 nm this estimation yields a field strength of about 60 Gauss. This is in a good agreement with experimental results.

The ability of nanorods to rotate by an external magnetic field yields two main conclusions. First, it clearly demonstrates the effect of the shape anisotropy on the

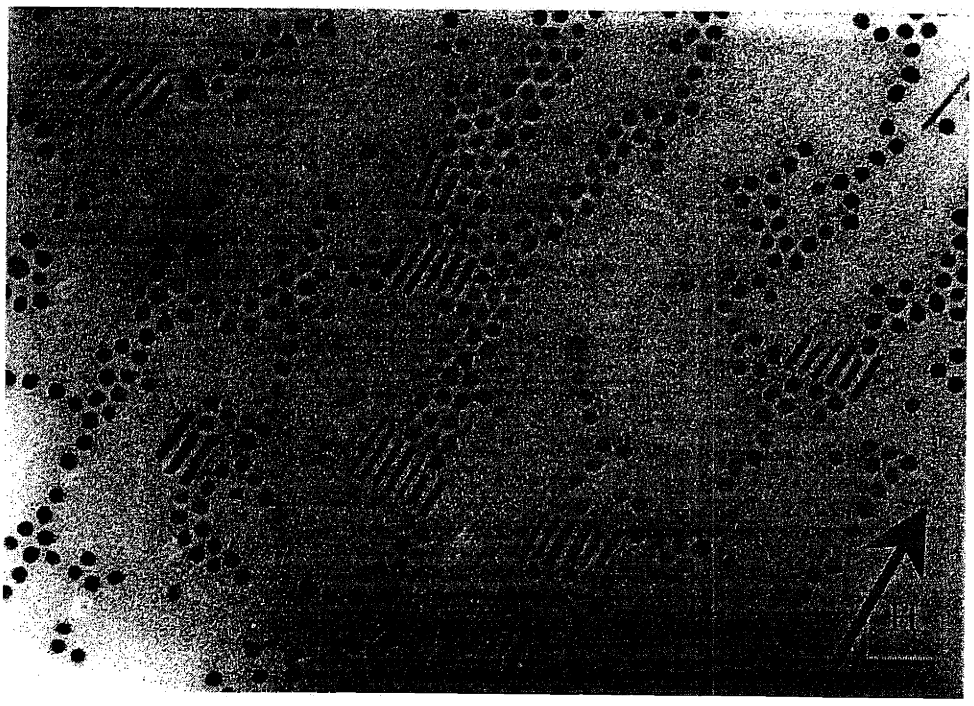

Figure 6.4. TEM image of cobalt nanocrystals after external magnetic field was applied; the alignment of nanorods is clearly observed.

overall magnetic properties of nanorods. Unlike the spherical nanocrystals, in which magnetocrystalline anisotropy alone is insufficient to "lock" magnetization in one particular direction at room temperature, the nanorods clearly have such a direction along their long axis. The nanorods, therefore, remain ferromagnetic even at room temperature and should have a measurable hysteresis. Second, the shape anisotropy (Appendix D) plays a dominant role and its value should be larger than that of magnetocrystalline anisotropy. Figure **6.5** shows calculated values for the shape anisotropy of cobalt nanorods as a function of their aspect ratios. The value of K_S reaches 6 x 10^6 erg/cm^3 for a typical nanorod with an aspect ratio of 10. This is larger than the value of K_M even for the pure hcp cobalt structure at room temperature (~5 x 10^6 erg/cm^3).[28] These rods, however, are cubic, as shown in the next section, and should have an even smaller crystalline anisotropy constant (~ 4 x 10^5 erg/cm^3).[28] The shape

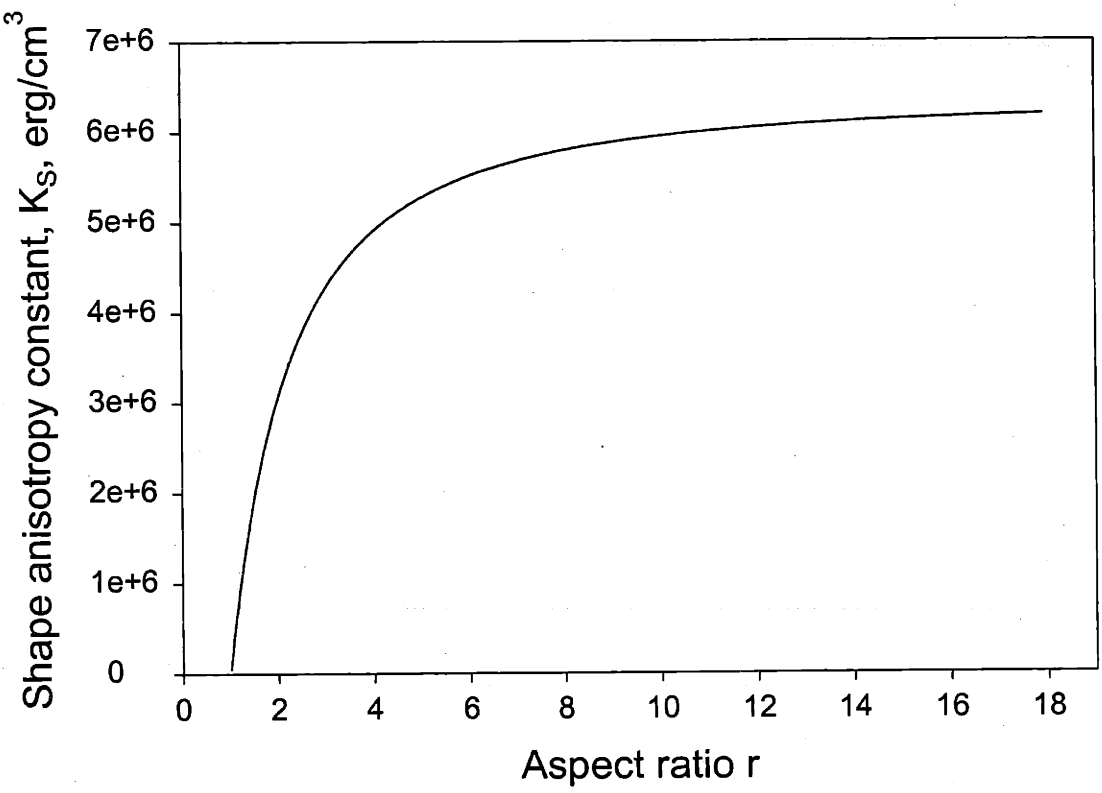

Figure 6.5. Shape anisotropy constant, K_S, for a single domain cobalt nanorod as a function of its aspect ratio, calculated with a prolate spheroid approximation.

anisotropy, therefore, exceeds the crystalline anisotropy by more than an order of magnitude and, indeed, plays the dominant role in determining the magnetic properties of these nanorods.

6.4.3 TEM imaging and electron diffraction

The most striking discovery about the nanocrystals of triangular as well as rod-like shapes was the fact that the great majority of them did not have any defects in their crystalline lattice and were, therefore, single crystals. This was in a sharp contrast with the spherical particles made in the same preparation that contained multiple stacking faults and were, in essence, polycrystalline.

High resolution imaging of triangular nanocrystals reveal the presence of two major projections shown in Figure **6.6**. Although some of the triangles showed no lattice

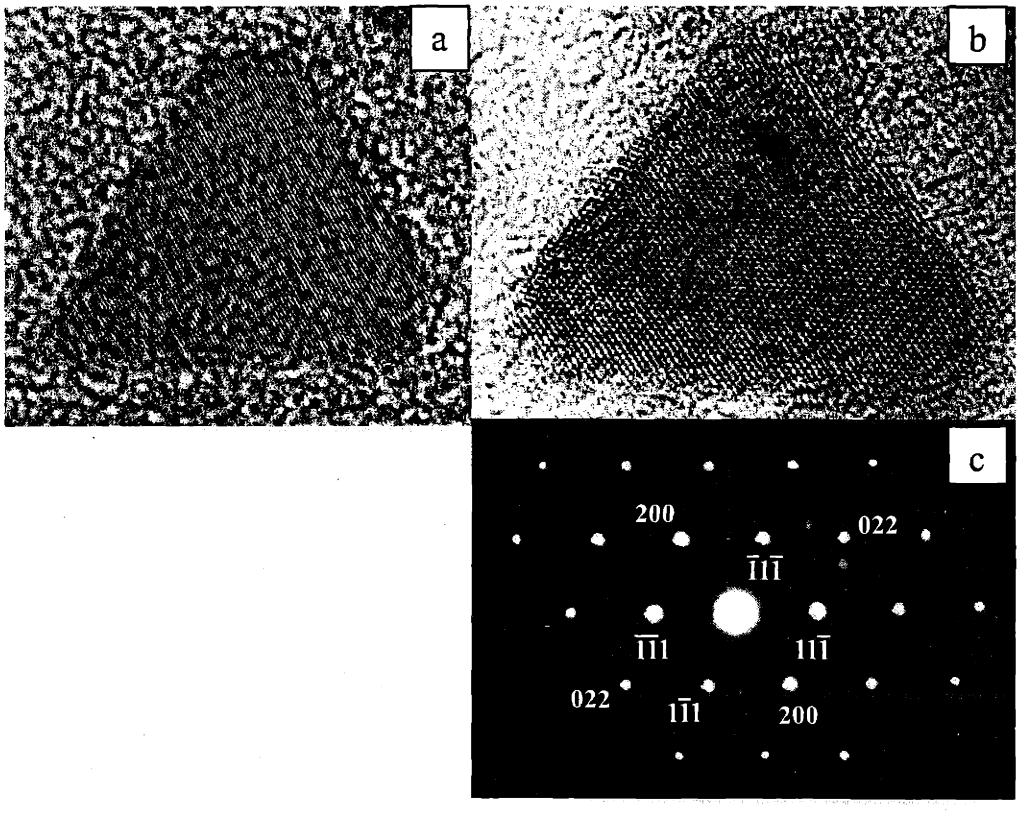

Figure 6.6. High resolution TEM images of triangular cobalt nanocrystals showing two major projections of an fcc lattice: **a** - <111>, **b** - <110>; image in **c** shows a corresponding pattern for the projection in **b**.

fringes because of their improper orientation with respect to the electron beam, all others show one of these two projections. The projection in **a** shows no defects with a measured atomic planes spacing of 1.99 Å. This could correspond to either a $<111>_{fcc}$ projection (d = 2.046 Å) or a $<002>_{hcp}$ projection (d = 2.023 Å). Since the corresponding electron diffraction patterns have the same symmetry for both these projections, no attempt was made to record a diffraction pattern for this nanocrystal. The measured lattice spacing in image **b** yields the value of 2.5 Å, which corresponds to the $<110>_{fcc}$ projection. In order to verify this conclusion the diffraction pattern of this nanocrystal was recorded (Figure **6.6c**). The symmetry of this pattern, indeed, corresponds to the $<110>_{fcc}$ lattice projection. Furthermore, the distances from the central spot of the identified reflections on the negative slide were 3.1 mm, 3.55 mm, and 5.05 mm for <111>, <200>, and <220> respectively. Taking into account the camera length used in the experiment (25 cm) and the wavelength of incoming electrons at 200kV acceleration (λ = 0.0251 Å), the lattice spacing corresponding to these reflections was calculated. They yield 2.024 Å, 1.768 Å, and 1.243 Å. All these numbers are in a good agreement with the reported values of the fcc cobalt structure (2.047 Å, 1.772 Å, and 1.253 Å respectively). Based on the symmetry of the recorded diffraction pattern and the subsequent calculations of corresponding lattice spacings, the hcp structure can be safely ruled out. It was concluded, therefore, that the triangular shaped cobalt nanocrystals have face-centered cubic structure.

Following this conclusion, a three-dimensional model for these crystals has been developed (Figure **6.7**). The two main projections are observed by bringing one vertex of the triangle either forward (Figure **6.7c**) or backward (Figure **6.7b**). In the first case, the two-dimensional projection of the equilateral triangle appears as an isosceles triangle with a reduced base. In the second case, it appears as an isosceles triangle with an expanded base. These observations are found in a good agreement with TEM images (Figure **6.6**).

A high resolution TEM study of cobalt nanorods revealed their highly crystalline nature as well. Similar to the triangular nanocrystals, a significant fraction of nanorods did not display any lattice fringes, which was attributed to their improper orientation with respect to the electron beam. In order to verify this conclusion, dark field imaging was

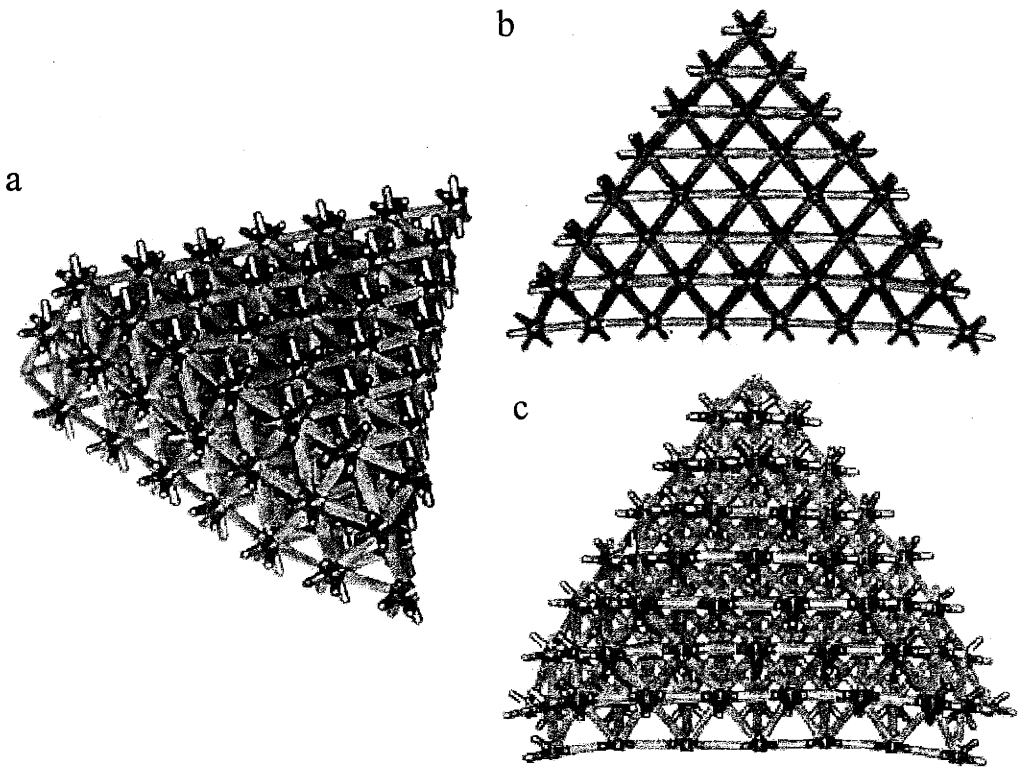

Figure 6.7 Three-dimensional model of triangular cobalt crystals: **a** - side view, **b** - <110>-projection, **c** - <111>-projection.

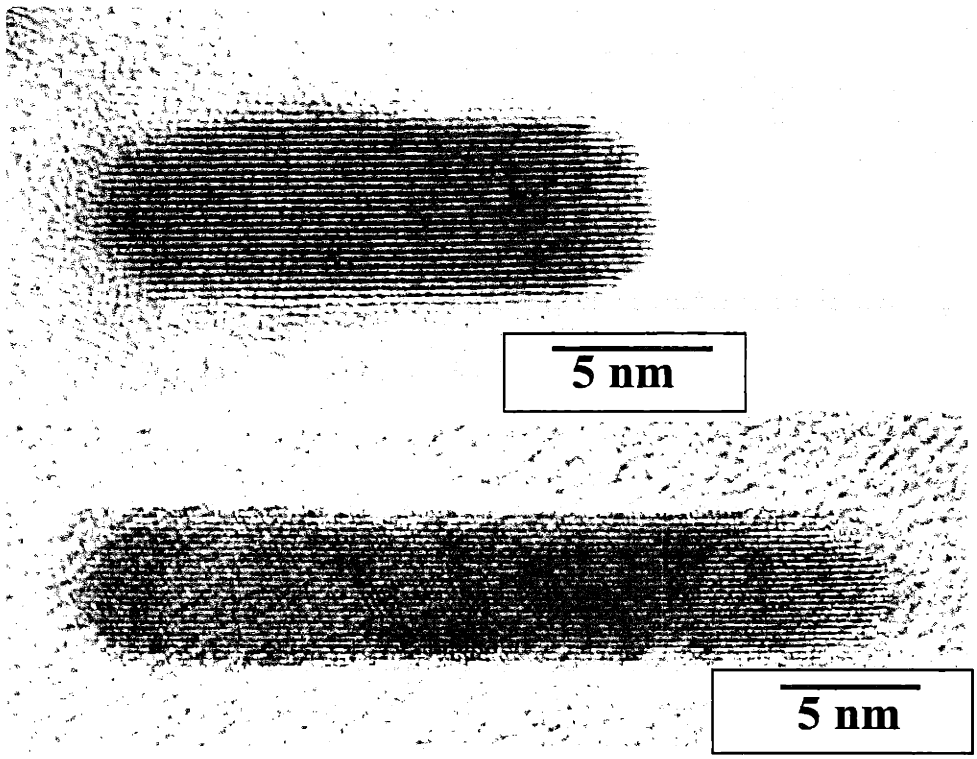

Figure 6.8. High-resolution TEM images of cobalt nanorods showing no defects in the crystal structure.

performed. It showed that the great majority of nanorods uniformly "light up" across their total volume, confirming the single crystalline nature of their structure. The exception consisted of the long and very thin rods (wires), which would understandably deviate from the perfect dark imaging conditions due to their flexibility and, therefore, the tendency to bend and twist. Among the fraction of nanorods that do show the lattice fringes, the most common projection is shown in Figure **6.8**. The measured lattice spacing yields 2.03 Å, which could again correspond to either cobalt structure. In order to distinguish between fcc and hcp, a diffraction study was needed. Unlike the previous case with triangular crystals, however, we found it impossible to focus the electron beam on a single nanorod because of its extremely small thickness. Instead, the following procedure was undertaken. First, a concentrated solution containing a significant number of nanorods (~30%) was exposed to a homogeneous magnetic field during its deposition on a TEM grid. This led to the alignment of the nanorods along the field as well as their partial phase separation from the spherical nanocrystals, as shown in Figure **6.9**. Subsequently, a diffraction pattern from the aligned nanorods was collected using a small diffraction aperture. This pattern is shown in Figure **6.10**. It consists of faint concentric rings overlaid with bright spots. The rings come from the small number of spherical nanocrystals mixed with the rods and randomly oriented on the TEM grid. The spot pattern, however, comes from the oriented rods. The brightest spots of the pattern correspond to a calculated lattice spacing of 1.26 Å that can be attributed to either $<220>_{fcc}$ or $<110>_{hcp}$ reflections (1.253 Å and 1.252 Å respectively). They were assigned to the growth direction of the rods. In order to distinguish between the two structures, the whole pattern was analyzed based on the following assumption: since the difference between the aligned rods is only in the rotational orientation around their long axes, the total diffraction pattern should be composed of multiple projections of a single rod while it is rotated around its long axis. In the case of cubic structure, the complete pattern should be reproduced by a rotation of 90° (as shown in Figure **6.11a**). For the fcc structure, only six distinct projections will contribute to the total pattern during such a rotation (shown in Figure **6.10**). After a detailed analysis, it was concluded that only the fcc structure can account for all of the observed diffraction spots without requiring the presence of new ones (Figure **6.11b**). The hcp structure, due to its lower symmetry,

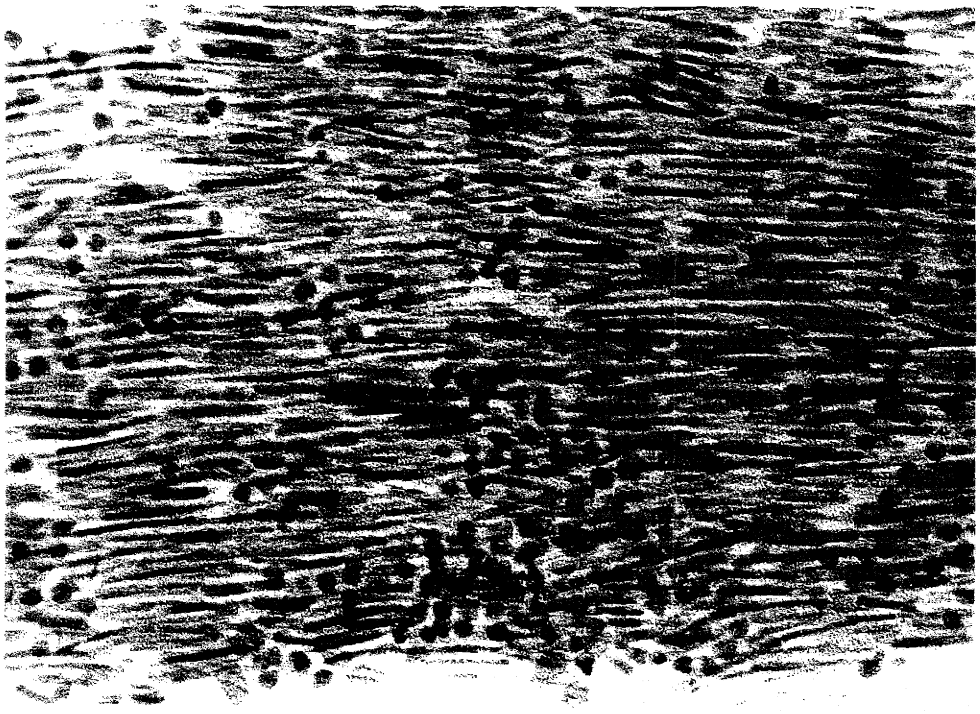

Figure 6.9. TEM image of the area with magnetically aligned cobalt nanorods from which a diffraction pattern was collected.

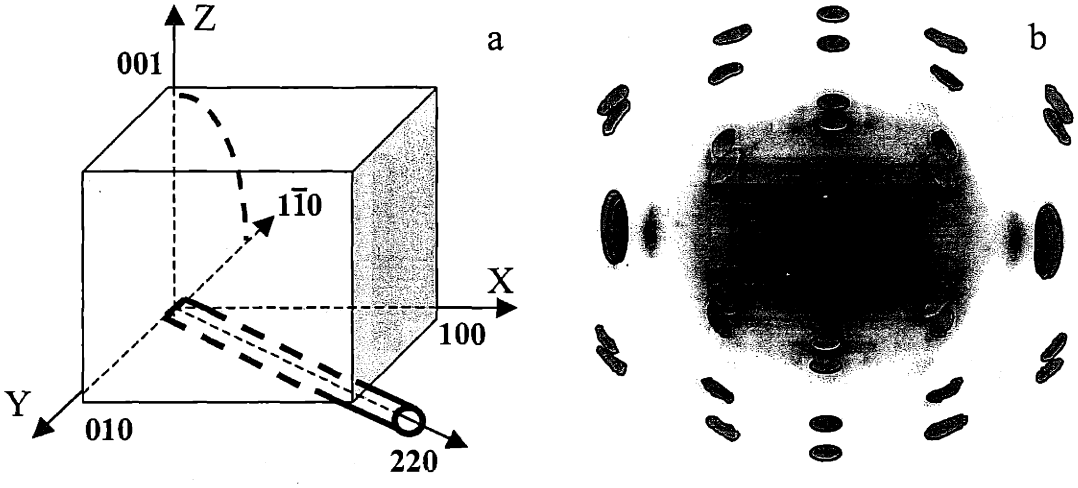

Figure 6.11 **a**-deconvolution of the diffraction pattern of oriented nanorods by projecting a single rod over its rotation by 90° (dashed line); **b**-the result of such deconvolution.

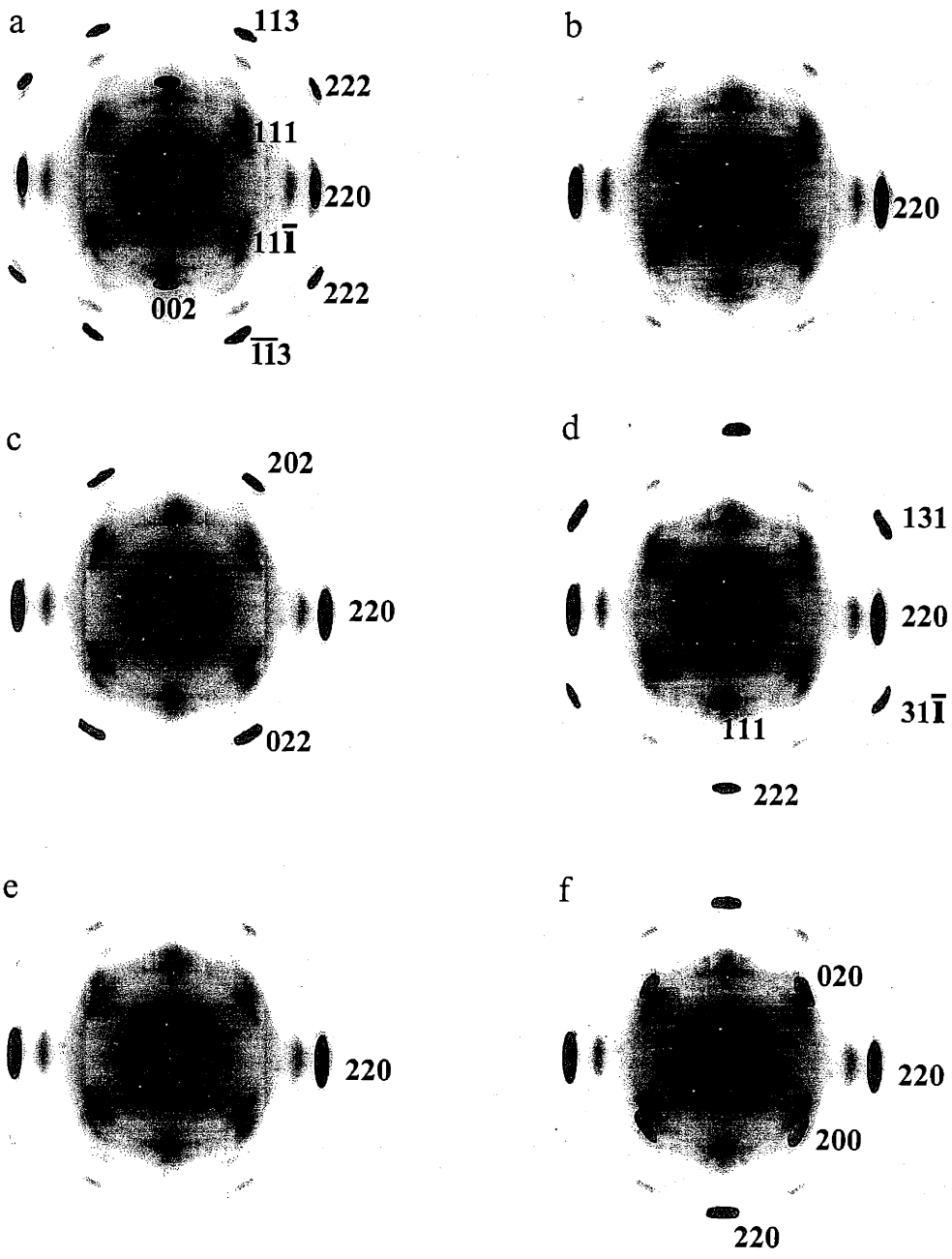

Figure 6.10 Electron diffraction pattern of aligned cobalt nanorods and its deconvolution into distinct single crystal projections: **a** - <1$\bar{1}$0>, **b** - <2-21>, **c** - <1$\bar{1}$1>, **d** - <1$\bar{1}$2>, **e** - <1$\bar{1}$3>, **f** - <001>.

would require the appearance of additional spots which are not observed in this pattern. It was, therefore, ruled out. Several spots left unaccounted in the analysis did not belong to cobalt. In fact, these spots appeared as soon as the sample was illuminated by the electron beam but quickly faded away thereafter. This was a strong indication that an organic material was decomposing under the intense electron beam and was attributed to the excessive amount of surfactants (sodium stearate) crystallizing in the narrow channels between the rods.

The cubic nature of the nanorods came as a surprise since this shape does not carry the high symmetry of the cubic lattice whereas the rod shape would be a natural shape for the hexagonal structure. Moreover, this is different from the results of Alivisatos, *et al.*, who recently reported a hexagonal structure for cobalt nanorods.[29] Although our preparation conditions as well as surfactants were slightly different from those used by Alivisatos, the product similarities are striking -- in both cases a number of triangular particles is observed along with the nanorods. Although it is quite possible for the cobalt nanorods prepared by Alivisatos, *et al.* to have a hexagonal structure, which is essential to their proposed growth mechanism, we believe the method of structure determination described in the report is not very reliable.

6.4.4 Proposed nucleation and growth mechanism

In the course of this research, three main conclusions become apparent. First, the sodium carboxylates play a critical role in the formation of both triangular and rod-shaped nanocrystals. As was shown in Chapter 4, the sodium carboxylates strongly bind to the surface of cobalt nanocrystals, forming a close-packed layer. It is therefore possible that in the nucleation stage of the growth, where the energy differences between various faces of the tiny crystals are the largest, these surfactants could selectively bind to specific facets leading to nuclei with a well-defined nonspherical shapes. Second, the kinetics of the growth also play an important role: a slow nucleation and growth leads to the formation of primarily triangular nanocrystals, whereas a rapid injection and a fast growth results in the formation of mostly nanorods. Third, the triangles and rods are always present together, and the difference is only in their relative amounts. Furthermore, they seem to relate to each other structurally. For example, many of the

shorter rods exhibit sharply cut edges which can be extrapolated to make a perfect triangle. Moreover, high-resolution images show that <111>-planes are always parallel to one side of a triangle or the long axis of a rod.

Based on these conclusions, the following growth mechanism is proposed: both triangular and rod-shaped nanocrystals originally nucleate as tiny triangles. This shape is "natural" to the fcc lattice since it carries the cubic symmetry. Then, depending on the kinetics of further growth, two different routes are possible (shown in Figure **6.12**). At slow growth and when there is enough surfactant in solution to evenly passivate all three facets of the nuclei, the growth rate is equal in all three directions and the triangles are formed. At very fast growth, on the other hand, or when there is not enough surfactant in the vicinity of the nuclei right after injection, the growth in any two directions can proceed faster than in the third one to the point that the addition of atoms to the third facet becomes energetically unfavorable. After that point, the growth continues in two directions only, leading to the formation of a rod.

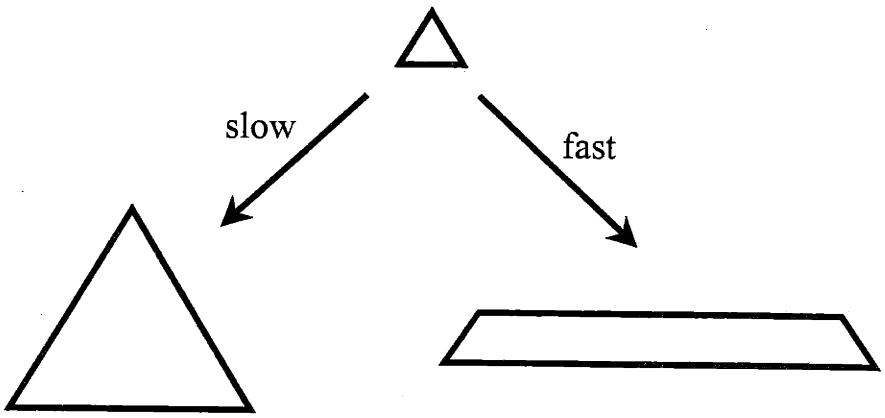

Figure 6.12 A proposed growth mechanism for triangular and rod-shaped nanocrystals with fcc structure.

The most interesting fact is that this mechanism is valid not only in the case of cobalt but appears universal for any metal with fcc structure. In several reports by Pileni, *et al.* on copper nanorods, the presence of triangular crystals is clearly observed.[11] The structures of palladium and nickel triangular nanocrystals prepared by Reetz *et al.* appear identical to ours. The absence of rods in the reaction product can be explained by the extremely slow growth processes (6 and 16 hours respectively). The simultaneous formation of triangular and rod-shaped nanocrystals was also observed in the case of gold.[30] Platinum nanocrystals prepared by El-Sayed, *et al.* appeared identical to ours but were reported to be tetrahedral, although no evidence for that was provided in the report.[21]

6.5 References

1. Hu J., Li L., Yang W., Manna L., Wang L., Alivisatos A. P. *Science* **2001**, 292, 2060.
2. Yu Y. Y., Chang S. S., Lee C. L., Wang C. R. C. *J. Phys. Chem. B* **1997**, 101, 6661.
3. Clint J. H., et al. Faraday Discuss. Chem. Soc.**1993**, 95, 219.
4. Holmes J. D., Johnston K. P., Doty R. C., Korgel B. A. *Science* **2000**, 287, 1471.
5. Hu J., Odom T. W., Lieber C. M. *Acc. Chem. Res.* **1999**, 32, 435.
6. Dai H., Wong E. W., Lu Y. Z., Fan S., Lieber C. *Nature* **1995**, 375, 769.
7. Wong W., Maynor B. W., Burns L. D., Lieber C. M. *Chem. Mater.* **1996**, 8, 2041.
8. Han W., *et al. Chem. Phys. Lett.* **1997**, 265, 374.
9. Han W., Fan S., Li Q., Hu Y. *Science*, **1997**, 277, 1287.
10. Whitney T. M., Jiang J. S., Searson P. C., Chien C. L. *Science* **1993**, 261, 1316.
11. Tanori J., Pileni M. P. *Langmuir* **1997**, 13, 639.
12. Pileni M. P., *et al. Adv. Mater.* **1999**, 11, 1358.
13. Filankembo A., Pileni M. P. *Appl. Surf. Sci.* **2000**, 164, 260.
14. Chen C. C., Chao C. Y., Lang Z. H. *Chem. Mater.* **2000**, 12, 1516.
15. Li M., Schnablegger H., Mann S. *Nature*, **1999**, 402, 393.
16. Qi L., Ma J., Cheng H., Zhao Z. *J. Phys. Chem. B* **1997**, 101, 3460.
17. Rees G. D., Evans-Gowing R., Hammond S. J., Robinson B. H. *Langmuir* **1999**, 15, 1993.
18. Filankembo A., Pileni M. P. *J. Phys. Chem. B* **2000**, 104, 5865.

19. Brüche V. B. *Kolloid-Zeitschrift* **1960**, 170, 97.

20. Curtis A. C., *et al. Angew. Chem. Int. Ed.* **1988**, 27, 1530.

21. Ahmadi T. S., Wang Z. L., Green T. C., Henglein A., El-Sayed M. A. *Science* **1996**, 272, 1924.

22. Bradley J. S., Tesche B., Busser W., Maase M., Reetz M. T. *J. Am. Chem. Soc.* **2000**, 122, 4631.

23. Manna L., Scher E. C., Alivisatos A. P. *J. Am. Chem. Soc.* **2000**, 122, 12700.

24. Peng Z. A., Peng X. *J. Am. Chem. Soc.* **2001**, 123, 1389.

25. Banfield J. F., *et al. Science* **2000**, 289, 751.

26. Alivisatos A. P. *Science* **2000**, 289, 736.

27. Park S. J., Kim S., Lee S., Khim Z. G., Char K., Hyeon T. *J. Am. Chem. Soc.* **2000**, 122, 8581.

28. Landolt-Börnstein numerical data and functional relationships in science and technology, Vol. 19/a (Eds.: K.H. Hellwege, O. Madelung), Springer-Verlag, Berlin, **1986**, p. 44-45.

29. Puntes V. F., Krishnan K. M., Alivisatos A. P. *Science* **2001**, 291, 2115.

30. Colvin V., *et al.* unpublished results.

Conclusions and Future Directions

After five and a half years of research and an enormous amount of spent chemicals, it is a good time to ask ourselves one very important question – what have we actually learned? In a short answer, we have learned quite a bit.

We realized a critical role played by surfactants in determining the crystal structure of chemically grown nanocrystals and discovered a new crystal structure of elemental cobalt. Although this structure was originally thought to be metastable (see Chapter 2), later experiments cast doubt on this conclusion. In particular, the observation that the structure nucleates not immediately upon injection, but can be formed by "reprocessing" of conventional structure using TOPO, suggests thermodynamic stability of ε-cobalt nuclei passivated by TOPO compared to both fcc and hcp structures.

We successfully developed a procedure for preparing nearly monodisperse nanocrystals of cobalt with control over their size, shape, and internal structure. Assembly of these single domain particles into two- and three-dimensional supercrystals has opened the way to a new class of magnetic materials – artificial ferromagnets. The domain sizes as well as interactions between different domains in these materials can be precisely engineered. Although the properties of such "designer materials" were not addressed in this thesis, this would certainly be an interesting endeavor in the future.

Magnetic characterization of cobalt nanocrystals was greatly hindered by their oxidation, which appeared as a formidable and not easily avoidable problem. Moreover, the very strong influence of a thin oxide layer on the magnetic properties of the metallic core came as surprise. Although the effect of surface oxidation was only qualitatively addressed in this thesis, a more precise control over the oxidation process and the thickness of an oxide shell can provide valuable information about a ferromagnetic/ antiferromagnetic interfaces in general. For all practical purposes, however, the oxidation should be avoided. One possible way to achieve that is to overcoat the size-selected cobalt nanocrystals with a thin layer of noble metal, such as gold. This could be useful in not only protecting the surface from oxidation, but also in enabling the use of various other surfactants and functional entities developed for gold nanocrystals.

Although the development of effective shape control methods for chemically grown nanocrystals is in its infancy, this work certainly provided some significant insights into possible mechanisms of such control. Moreover, a proposed mechanism for triangular and rod-shaped cobalt nanocrystals appears rather general and valid for many fcc metals. The yield of the "shaped" nanocrystals remained nevertheless relatively low with the use of sodium carboxylates. Higher yields, we believe, might be achieved with the use of more metal-specific carboxylates such as those functionalized in the α-position.

Appendix A

On Magnetocrystalline Anisotropy

Magnetocrystalline anisotropy energy E_m arises from the fact that not all the directions inside the crystal are equally capable of supporting magnetization. For cubic lattices (such as fcc cobalt) the anisotropy energy per unit volume is expressed by

$$E_m = K_0 + K_1\left(\alpha_1^2\alpha_2^2 + \alpha_2^2\alpha_3^2 + \alpha_3^2\alpha_1^2\right) + K_2\left(\alpha_1^2\alpha_2^2\alpha_3^2\right) + ...$$

where K_0, K_1, K_2,...are the anisotropy constants for a particular material and are expressed in engs/cm^3 or J/m^3, α_i,α_j, α_k are the direction cosines of the angle between the magnetization vector and the crystallographic axes. Higher powers are generally not needed, and sometimes K_2 is so small that the term involving it can be neglected. The first term, K_0, is independent of angle and is usually ignored.

The values of K define the hard and easy magnetic directions in the crystal as shown below.

Crystal Anisotropy Energies for Various Directions in a Cubic Crystal

h, k, l	α_1	α_2	α_3	E_m
[100]	1	0	0	K_0
[110]	$1/\sqrt{2}$	$1/\sqrt{2}$	0	$K_0 + K_1/4$
[111]	$1/\sqrt{3}$	$1/\sqrt{3}$	$1/\sqrt{3}$	$K_0 + K_1/3 + K_2/27$

Directions of Easy, Medium, and Hard Magnetization in a Cubic Crystal

K_1	+	+	+	−	−	−
K_2	$+\infty$ to $-9\,K_1/4$	$-9\,K_1/4$ to $-9\,K_1$	$-9\,K_1$ to $-\infty$	$-\infty$ to to $9\ K_1\ /4$	$9\ K_1\ /4$ to $9\ K_1$	$9\ K_1$ to $+\infty$
Easy	⟨100⟩	⟨100⟩	⟨111⟩	⟨111⟩	⟨110⟩	⟨110⟩
Medium	⟨110⟩	⟨111⟩	⟨100⟩	⟨110⟩	⟨111⟩	⟨100⟩
Hard	⟨111⟩	⟨110⟩	⟨110⟩	⟨100⟩	⟨100⟩	⟨111⟩

For hexagonal lattices (such as hcp cobalt) magnetocrystalline anisotropy energy E_m usually depends on only a single angle θ between the magnetization vector and the c crystallographic axis. Therefore,

$$E_m = K_0' + K_1' \cos^2\theta + K_2' \cos^4\theta + ...$$

However, in a hexagonal lattice it is customary to white this equation in powers of sin θ ($\sin^2\theta = 1-\cos^2\theta$). This substitution yields

$$E_m = K_0 + K_1 \sin^2\theta + K_2 \sin^4\theta + ...$$

Directions of Easy and Hard Magnetization in a Hexagonal Crystal

K_1	+	+	−	−
K_2	$K_2 > -K_1$	$K_2 < -K_1$	$K_2 < K_1\ /2$	$K_2 > K_1\ /2$
Easy	c-axis	a-b plane	a-b plane	$\theta = \sin^{-1}(-K_1/2K_2)^{-1/2}$
Hard	a-b plane	c-axis	c-axis	$\theta = \sin^{-1} -(-K_1/2K_2)^{-1/2}$

Appendix B

On Langevin Equation for Paramagnetism

The Langevin theory of paramagnetism is based on the assumption that in the absence of an applied magnetic field the directions of the spins are totally random and therefore equally distributed throughout the sample by thermal fluctuations. When the external magnetic field is applied, the preferred orientation is introduced and the spins start to align along the field.

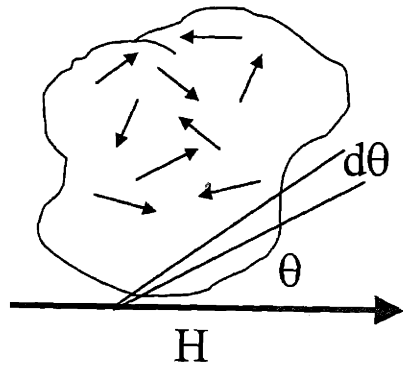

Let n(θ)dθ be the number of spins in the unit volume that makes an angle between θ and θ + dθ with the direction of the field. This number must be proportional to the solid angle 2πsinθdθ and also to Boltzman factor exp(MHcosθ/kT). This factor describes the relative probability of a spin to make an angle θ with H. Then we have

$$n(\theta)d\theta = 2\pi n_0 e^{(MH\cos\theta)/kT}\sin\theta d\theta$$

where n_0 is a normalization factor determined by the fact that the total density of spins is N; that is

$$\int_0^{\pi} n(\theta)d\theta = 2\pi n_0 \int_0^{\pi} e^{(MH\cos\theta)/kT}\sin\theta d\theta = N$$

The intensity of magnetization is given by

$$I = \int_0^{\pi} M\cos\theta n(\theta)d\theta$$

Substituting from the above we can rewrite this equation in the following form:

$$I = NM\frac{\int_0^{\pi} n(\theta)\cos\theta d\theta}{\int_0^{\pi} n(\theta)d\theta} = NM\frac{\int_0^{\pi} e^{(MH\cos\theta)/kT}\cos\theta\sin\theta d\theta}{\int_0^{\pi} e^{(MH\cos\theta)/kT}\sin\theta d\theta}$$

Changing the variables to MH/kT=α and cos(θ)=x we would get

$$I = NM\frac{\int_1^{-1} e^{\alpha x} x dx}{\int_1^{-1} e^{\alpha x} dx} = NM\left(\frac{e^{\alpha}+e^{-\alpha}}{e^{\alpha}-e^{-\alpha}} - \frac{1}{\alpha}\right) = NM\left(\coth\alpha - \frac{1}{\alpha}\right)$$

The function in parentheses is called the Langevin function. When applied field is relatively small and the temperature is high (α<<1) this function may be expanded as

$$L(\alpha) = \frac{\alpha}{3} - \frac{\alpha^3}{45} + ...$$

Neglecting the terms beyond the first one, we have the result

$$I = \frac{NM^2}{3kT}H \qquad \text{or} \qquad \chi = \frac{I}{H} = \frac{NM^2}{3kT}$$

This is the well-known Curie law for temperature dependence of the susceptibility for paramagnetic substance.

Appendix C

On Blocking Temperature and Temperature Dependence of Coercivity for a Coherent Rotation (Stoner-Wohlfarth) Model

Let's assume that an assembly of uniaxial particles has been magnetized to some state by an applied magnetic field, and the field is then switched off at time t=0. The initial magnetization will begin to decay, with the rate of decay being proportional to the magnetization existing at that time and to the Boltzman factor exp(–KV/kT), because this exponential gives the probability of a particle having enough thermal energy to overcome the energy gap $\Delta E = KV$ required for reversal. Therefore,

$$-\frac{dM}{dt} = f_0 M e^{-KV/kT} = \frac{M}{\tau}$$

where f_0 is the frequency factor and has a value of about 10^9 sec^{-1}, τ is the relaxation time. To find how the magnetization decays with time we integrate:

$$\int_{M_i}^{M_r} \frac{dM}{M} = -\int_0^t \frac{dt}{\tau} \quad \text{or} \quad \ln\frac{M_r}{M_i} = -\frac{t}{\tau} \quad \text{or} \quad M_r = M_i e^{-t/\tau} \quad \text{with} \quad \frac{1}{\tau} = f_0 e^{-KV/kT}$$

Because τ varies very rapidly with V and T, small changes in τ do not produce much change overall and it becomes possible to arbitrarily set the value of τ to 10^4 seconds for a typical time of the SQUID experiment (10^4 = 2hour 45min.) over which magnetization is measured. In this case

$$10^{-4} = 10^9 e^{-KV/kT} \qquad \text{or} \qquad \frac{KV}{kT} = 30$$

Therefore, for the particles of a particular size it is possible to define the **blocking temperature T_B,** at which the behavior will switch from superparamagnetic to ferromagnetic:

$$T_B = \frac{KV}{30k}$$

Let's now assume the assembly of uniaxial particles with their easy axes parallel to the z-axis. This assembly is initially saturated in the +z direction. A field H is then applied in

the –z direction, so that magnetization M_S in each particle makes an angle θ with +z. The total energy is then

$$E = V\left(K\sin^2\theta + HM_S\cos\theta\right)$$

The energy barrier for reversal is the difference between the maximum and the minimum values of E, which are found by setting the derivative to zero:

$$\frac{dE}{d\theta} = 2VK\sin\theta\cos\theta - VHM_S\sin\theta = V\sin\theta\left(2K\cos\theta - HM_S\right) = 0$$

This provides for two extreme points $\sin\theta = 0$ and $\cos\theta = HM_S/2K$ with corresponding energy values

$$E_1 = VHM_S \qquad \text{and} \qquad E_2 = VK + \frac{VH^2M_S^2}{4K}$$

So that

$$\Delta E = E_2 - E_1 = KV\left(1 - \frac{HM_S}{2K}\right)^2$$

When the applied field is increased, the barrier will be reduced until 30kT, when thermally activated reversal would become possible. This field will be the coercivity H_C, give by

$$\Delta E = KV\left(1 - \frac{H_CM_S}{2K}\right)^2 = 30kT$$

This leads to the following temperature dependence of coercivity

$$H_C = \frac{2K}{M_S}\left[1 - \left(\frac{30kT}{KV}\right)^{1/2}\right]$$

When the temperature approaches zero, the coercivity approaches the maximum value of $2K/M_S$ since it is unaided by thermal energy.

For the assembly with randomly oriented particles the coercivity reaches only 0.48 of it's maximum value, as was calculated by Stoner and Wohlfarth [7.23]

Appendix D

On Shape Anisotropy

Before explaining the origin of the shape anisotropy it is necessary to introduce the concept of *demagnetizing fields*. Suppose a bar is magnetized by a magnetic field applied from left to right, and subsequently removed. Then a north pole is formed at the right end, and a south pole at the left end (see Figure).

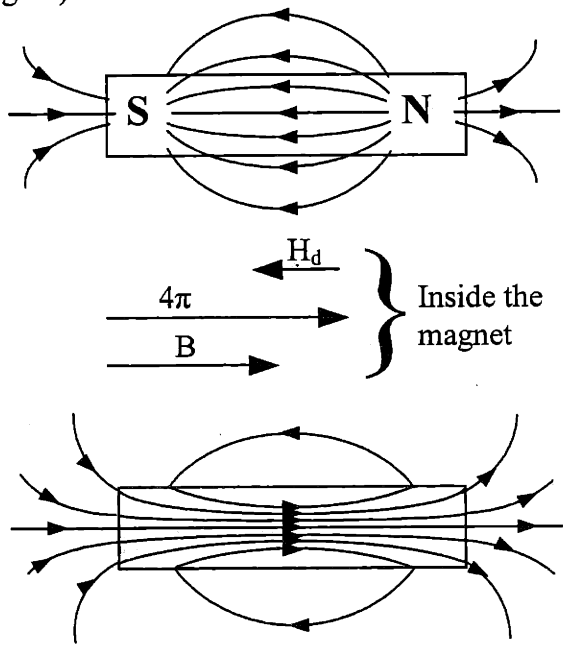

The H lines, radiating out from the N pole and ending at the S pole, constitute a field inside the magnet that acts from N to S and which therefore tends to demagnetize the magnet. The demagnetizing field H_d acts in the opposite direction to the magnetization M which creates it. When H_d is the only field acting, the relationship $B = H + 4\pi M$ becomes $B = -H_d + 4\pi M$. The induction B inside the magnet is therefore less than $4\pi M$ but in the same direction, since H_d can never exceed $4\pi M$ in magnitude. These vectors are shown in Figure on the right. Outside the magnet, B is identical to H.

The magnetization inside a bar magnet is not uniform: the lines diverge toward the ends, so that the flux density there is less than in the center. However, if the magnet is tapered toward each end, the induction inside can be made uniform throughout. It could be shown that the correct taper to achieve this result is that of an ellipsoid. The uniformity in M and B is due to the uniformity of H_d throughout the volume.

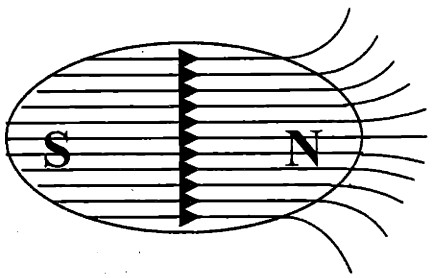

The demagnetizing field H_d of a body is proportional to the magnetization which creates it: $H_d = N_d * M$, where is the demagnetizing factor or coefficient. N_d depends mainly on the shape of the

body and can be calculated exactly for several specific shapes:

1. *Sphere* $N_d = \frac{4\pi}{3}$

2. *Prolate spheroid*, or rod. a = b c. Put c/a = r. Then,

$$N_c = \frac{4\pi}{(r^2-1)}\left[\frac{r}{\sqrt{r^2-1}}\ln\left(r+\sqrt{r^2-1}\right)-1\right]$$

$$N_a = N_b = \frac{4\pi - N_c}{2}$$

3. *Oblate spheroid*, or disk. a b = c, and c/a = r.

$$N_a = \frac{4\pi r^2}{r^2-1}\left[1-\sqrt{\frac{1}{r^2-1}}\sin^{-1}\frac{\sqrt{r^2-1}}{r}\right]$$

$$N_b = N_c = \frac{4\pi - N_a}{2}$$

The *magnetostatic energy* E_{ms} is the energy stored by a permanently magnetized body in zero applied field. It is given by the integral evaluated over all space:

$$E_{ms} = \frac{1}{8\pi}\int H_d^2 dv \quad \text{(ergs)}$$

However, it can be approximated by a more simple expression:

$$E_{ms} = \frac{1}{2}N_d M^2 \quad (\text{ergs/cm}^3)$$

For prolate spheroid, whose magnetization M has the components parallel and perpendicular to its long axis, this expression becomes:

$$E_{ms} = \frac{1}{2}\left[(M\cos\theta)^2 N_c + (M\sin\theta)^2 N_a\right] = \frac{1}{2}M^2 N_c + \frac{1}{2}(N_a - N_c)M^2\sin^2\theta$$

This expression for magnetostatic energy has the same angular dependence as the uniaxial magnetocrystalline anisotropy energy (Appendix A):

$$E_m = K_0 + K_1\sin^2\theta$$

Therefore, the shape anisotropy constant K_S is given by:

$$K_S = \frac{1}{2}(N_a - N_c)M^2$$

Acknowledgements

First of all, I would like to thank my advisor – Moungi Bawendi – for his always invaluable advice and great patience during the slow times of my project. Moungi, thanks for always being ready to meet with me and to discuss any of my problems, which were hardly limited to science alone.

Over the course of the last six years, I was fortunate to work in the group with wonderful people who were great fun to work with. Hans Eisler, Wing Woo, Vikram Sundar, Ken Shimizu, Sungjee Kim, Nathan Stott, Inhee Chung, Mirna Vitasovic, Joe Tracy, and Brent Fisher – thanks for being good friends and colleagues. I really enjoyed working with you, and I wish all of you the best.

The list of my friends and colleagues would not be complete without mentioning the names of former group members who greatly supported me in the lab as well as in life during the early stages of my graduate carrier – Hedi Mattoussi, Robert Neuhauser, Bashir Dabbousi, Ken Kuno, Fred Mikulec, Steve Empedocles, and Catherine Leatherdale – thanks for encouraging me and always providing your help and expertise.

This work could not be possible without significant input from the MIT faculty and staff. I would like to thank Prof. Ned Thomas and Prof. Caroline Ross for their willingness to discuss my data and for their valuable advice. The electron microscopy and diffraction, which are a significant part of this thesis, would not have been possible without the training and supervision of Mike Frongillo. I would also like to acknowledge the help of Tony Garett-Reed (microscopy lab), Neel Chaterjee (WDS analysis), Joe Adario and Peter Kloumann (x-ray lab), and Cheng-Feng Chou (SQUID lab).

Special thanks to the Corning Foundation for their financial support during my studies and for a brief introduction into the industrial research environment.

Last but not least, I would like to thank my ex-wife Alyssa Dinega for enriching my graduate carrier with such invaluable "real life" experiences as fatherhood, buying a home, divorce, selling a home, and fighting protracted legal battles over my parental rights. Without all those experiences my graduate life would certainly resemble living in paradise without having to die first.